

Photochemical Strategies
to Decage Organic
Compounds

Thesis by
Clinton Joseph Regan

In Partial Fulfillment of the Requirements for
the Degree of
Doctor of Philosophy

The Caltech logo, featuring the word "Caltech" in a bold, orange, sans-serif font.

CALIFORNIA INSTITUTE OF TECHNOLOGY
Pasadena, California

2016
(Defended May 27, 2016)

© 2016

Clinton Joseph Regan
All rights reserved

ACKNOWLEDGEMENTS

Rarely am I given the opportunity to thank all the wonderful people that have guided me down this path of fortune.

I vividly recall Dennis' infectious excitement when he first revealed a new photochemistry project to the group. I am deeply thankful for his trust and faith in my abilities to explore this uncharted territory, and I am delighted to know that others will continue to carry the photochemistry torch in my stead. I must also thank Dennis for an endless number of conversations that I would generally tag as 'physical organic chemistry,' 'photochemistry,' and 'cool.' How he has maintained his composure when these conversations have digressed from my primary research agenda is unfathomable, and I am thankful for it.

To my advisor of one year, Sarah Reisman, who graciously accepted me into her lab, put me through the best organic-synthesis boot camp that I could have imagined, and was understanding when it was time to go, your guidance has not been forgotten and is deeply appreciated.

I would like to thank my committee members Brian Stoltz and Theo Agapie. Brian has always reminded me to be proud of my work, which is a theme that has guided me through my Ph.D. Theo has constantly engaged me on a creative level during our committee meetings.

There are a couple of 'gems' at Caltech that have enriched my academic experience in ways that I fear I may never experience again. I'd like to thank:

Scott Virgil for his guidance in all things HPLC and in particular his persistent upkeep of the Crellin LCMS, which has saved me from confusion on exactly 2144 occasions.

David VanderVelde for patiently allowing me to tinker with Siena, and not being too upset when I resort to taking out the probe to fix a software glitch.

In addition, I am grateful to Eric Anslyn, who ushered me into the world of organic chemistry while I was still an art major at UT Austin. His enthusiasm for science and research has constantly guided my own ambitions.

The members of the Dougherty Lab have provided a fun and stimulating environment to work in, and I wish them all the best of luck. In addition, I would like to thank the current

and former members of Team Photoacids/Project Brainprotect –Kayla Busby, Matt Davis, and Catie Blunt. It has been a pleasure working in the chemistry lab with these individuals, and I have appreciated our many conversations on synthetic troubleshooting, photochemistry, and the like.

I have collaborated closely David Walton and Oliver Shafaat on the mechanism project, and am thankful for their thoughts, hard work, and discourse. Oliver has meticulously recorded all of our transient absorption data and I look forward to seeing what happens over the summer with the transient IR spectroscopy. David is brilliant and I'm constantly amazed at the ideas he generates and how smoothly he executes his dissertation work. I am extremely thankful to have been involved in development of the benzoquinone trimethyl lock photochemistry.

I have had many thoughtful conversations with Bryce Jarman and Matt Rienzo, who are always willing to discuss mechanistic models, complicated spectra, or brainstorm for creative ideas. I will miss their presence after leaving Caltech.

Chris Marotta and Ethan Van Arnam are true friends, and I hope we keep in touch.

I would not be here if it weren't for the love and guidance from my parents. They have always supported me in whatever path I have wanted to take, and I hope they understand that they are loved and appreciated. My brothers Roddy and Brad are my closest friends. Brad's controlled and calculated composure has always been a life model that I have looked up to, and I feel this will become increasingly important as I move from graduate school into the next phase of my life. Roddy always has a way of seeing through my antisocial eccentricities, quickly revealing the true nature of our friendship. I am lucky to have grown up with him.

My wife Patricia has been by my side through this entire process, and has kept me sane by making me take walks, water plants, and make dinner. Thank you for going through life with me. I love you.

To Charlie

ABSTRACT

This dissertation primarily describes new photochemical decaging systems that are activated by visible light. Such systems are expected to be useful as chemical biology tools or as drug delivery systems in a therapeutic context. A primary motivation for the development of these systems is for the treatment of traumatic brain injury, where a decaging strategy would require activation by low energy near-infrared light. Since most photochemical reactions are initiated using ultraviolet light, a primary challenge in developing these systems is overcoming the low energy efficiency of typical photochemical processes. Initial model systems are designed to address this challenge through use of the photoacidic effect. While many hydroxyaromatic compounds are known to become much more acidic in their excited state, the effect has never been utilized to accelerate an acid-catalyzed chemical reaction. Investigations are carried out in Chapter 2 to probe for the possibility of this unprecedented photochemistry. Ultimately, the results suggest that the acid-catalyzed decaging processes are too slow to be useful in a photochemical context. This finding led to the development of decaging strategies that utilize a *phototriggered* approach. In Chapter 2, a system is described where decaging occurs through rapid lactonization of a photogenerated hydroquinone. Formation of the hydroquinone results from an intramolecular photoreduction of the benzoquinone due to activation by violet light. Detailed mechanistic studies carried out on this system ultimately establish the importance of the triplet state in the overall reaction. While most benzoquinones form the triplet with unit efficiency, the system studied here forms the triplet in less than 10% yield. However, when the triplet is formed, it proceeds cleanly to products with high efficiency. Although the benzoquinone system has been useful for mechanistic studies, its application as a therapeutic decaging strategy has been challenging. Efforts to extend the wavelength toward the near-infrared have led to loss in photochemical reactivity. Ultimately, this challenge was overcome through the use of methylene blue. Methylene blue is a common organic dye that is activated by red light and undergoes photoreduction to a colorless form, similar to the benzoquinone systems. In Chapter 4, derivatives of methylene blue that are capable of undergoing photoreductive cyclization are designed and synthesized. Ultimately, these systems are found to be capable of rapidly decaging alcohols using red light.

PUBLISHED CONTENT AND CONTRIBUTIONS

TABLE OF CONTENTS

Acknowledgements	iii
Abstract	vi
Published Content and Contributions	vii
Table of Contents	viii
List of Figures, Schemes, and Tables	x
Chapter I: Introduction	1
1.1 Traumatic Brain Injury: A Critical Need for Decaging Strategies	1
1.2 Summary of Dissertation Work	3
1.3 References	4
Chapter II: The Utility of Excited-State Proton Transfer in the Development of Novel Photochemical Reactions	5
Section 1: Introduction	5
Section 2: t-Butyl Ester Model Systems	8
<i>General Chemical Design</i>	8
<i>The 2-Naphthol Model System</i>	10
<i>The Cy5 Model System</i>	13
<i>Discussion</i>	17
Section 3: General-Acid Catalyzed Systems	19
<i>Introduction</i>	19
<i>Oxocarbenium Ion Formation</i>	23
Section 4: Bimolecular Systems	27
<i>Introduction</i>	27
<i>Results and Discussion</i>	28
Section 5: Conclusions	31
Section 6: Experimental	31
<i>Materials and Methods</i>	31
<i>Preparative Procedures and Spectroscopic Data</i>	32
Section 7: References	43
Chapter III: Mechanistic Studies on the Trimethyl Lock Cyclization of Sulfur-Substituted Benzoquinones Triggered by Visible Light	46
Section 1: Introduction and Synthesis	46
Section 2: Steady-State Photolysis	49
Section 3: Mechanistic Investigations	51
<i>Quantum Yields and Radical Probes</i>	51
<i>Laser Flash Photolysis</i>	54
<i>Sensitization and Quenching Studies</i>	55
Section 4: Mechanistic Interpretation	61

Section 5: Conclusions	67
Section 6: Experimental	67
<i>Materials and Methods</i>	67
<i>Preparative Procedures and Spectroscopic Data</i>	68
<i>Preparative Scale Photolysis</i>	74
<i>Quantum Yield Measurements</i>	76
Section 7: References	80
Chapter IV: Decaging Strategies Based on the Photoredox Chemistry Of Methylene Blue	85
Section 1: Introduction	85
<i>A Brief History of Methylene Blue</i>	85
Section 2: Photooxidation of Tertiary Amines	89
<i>Photobleaching Studies</i>	89
<i>Results and Discussion</i>	91
<i>A Tethered Diamine System</i>	92
Section 3: Decaging via Lactam Formation	94
Section 4: Conclusions	97
Section 5: Experimental	97
<i>Materials and Methods</i>	97
<i>Preparative Procedures and Spectroscopic Data</i>	99
<i>Photolysis Procedures</i>	102
Section 6: References	103

LIST OF SCHEMES, FIGURES, AND TABLES

<i>Chapter 2</i>		<i>Page</i>
Scheme 1	General design of 2-naphthol model system.....	9
Figure 1	Synthesis of the 2-naphthol model system.....	10
Figure 2	Forster cycle for 2-naphthol	11
Figure 3	Spectra for 1 in acetonitrile.....	12
Figure 4	¹ H-NMR spectrum of 1 in acetonitrile	13
Scheme 2	Synthesis of the Cy5 model system.....	14
Scheme 3	Optimization of the Fischer indole formation of 8	16
Figure 5	Delocalization of negative charge in 1,14,14'	18
Scheme 4	Model for acid-catalyzed reactions	19
Scheme 5	A1 mechanism for t-butyl ester hydrolysis	20
Scheme 6	A1 mechanism for ESIPT t-butyl ester hydrolysis	20
Figure 6	Compounds studied for ESIPT general-acid catalysis.....	22
Figure 7	Synthesis of 18 – 21	23
Scheme 7	Photolysis of 20 and 21	24
Figure 8	Ground and excited state reactions of 18	25
Figure 9	Intramolecular general-acid catalysis of 20/21	27
Figure 10	Stern-Volmer quenching of 24	29
Scheme 8	Photoreaction of 24	30
 <i>Chapter 3</i>		 <i>Page</i>
Figure 1	Components of the photodecaging strategy	47
Figure 2	Synthesis of 4	48
Figure 3	UV/Vis spectrum of 4a	49
Figure 4	Products of photolysis of 4	50
Scheme 1	Retrosynthetic analysis of the photoreaction	51

Scheme 2	Potential intermediates in the H-shift reaction.....	52
Table 1	Spectroscopic and photolysis data for 4	53
Figure 5	Transient absorption spectrum for 4	54
Figure 6	Stern-Volmer quenching by diethylaniline.....	56
Figure 7	Reaction scheme for the conversion of 4 to 5	57
Figure 8	Sensitized photolysis of 4 by thioxanthone.....	59
Figure 9	Mechanistic interpretation.....	61
Figure 10	DFT M06/6-311++G** calculations.....	63

Chapter 4

Page

Figure 1	UV/Vis spectrum of methylene blue.....	87
Figure 2	Photochemical processes of methylene blue.....	87
Figure 3	Overview of decaging strategies.....	88
Figure 4	Photobleaching of methylene blue by amines.....	89
Figure 5	Photobleaching of methylene blue by TMEDA.....	90
Figure 6	Proposed model for photoreactivity with amines.....	91
Figure 7	Synthesis and photolysis of 2	92
Figure 8	Singlet oxygen trapping studies.....	93
Figure 9	Proposed model for reactivity of 2	94
Figure 10	Synthesis and photolysis of 4	95
Figure 11	Synthesis and photolysis of 5	96

Chapter 1

INTRODUCTION

Traumatic Brain Injury: A Critical Need for Photodecaging Strategies

The long-term effects of traumatic brain injury (TBI) are a growing concern for both the healthcare system and society as a whole. According to a recent report, nearly 2 million individuals in the United States sustain a TBI each year due to vehicular accidents, sports-related injuries, and other accidents that involve exposure of the head to excessive force¹. The very young and old are particularly susceptible to TBI, where falling is a primary cause of the injury. Additionally, the exposure of military personnel to concussive blasts often results in long-term neurological disorders that have been linked to TBI.

The effects of TBI on the brain are known to involve both primary and secondary injury^{1,2}. The primary injuries include tissue damage, hemorrhaging, and contusions that are a direct result of the impact. The secondary injuries involve long-term changes in biochemical pathways as a direct result of the primary injury, and include effects such as oxidative stress, excitotoxicity, inflammation, and cell death. The secondary injuries are also thought to be the primary cause for the development of neurological disorders, such as Alzheimer disease, chronic traumatic encephalopathy, and others which involve a whole spectrum of abnormal psychiatric indications³.

Much of the secondary injury occurs in the minutes to hours immediately after the accident⁴. The clinical fields refer to this time period as the ‘golden hour’, because it is the time when therapeutic intervention is the most successful at mitigating the long-term and permanent effects of the injury. Studies have demonstrated that patients who arrive at the hospital within the first sixty minutes after sustaining a TBI, or even within the first few hours, have an improved chance of optimal recovery over those that arrive days to weeks later⁴.

Despite the increasing amount of scientific and clinical research on the effects of TBI, there are only a handful of therapeutic agents that have been developed to treat the disease^{1,2,5}.

This is primarily due to the complexity and diversity of the biochemical pathways that are involved in the secondary injury. One indication that seems to be common in many secondary injuries is excitotoxicity in the damaged neurons⁶. Excitotoxicity is caused by upregulation of the neuronal excitatory pathways mediated principally by the neurotransmitter glutamate. Dysregulation of these pathways ultimately results in cell death, and studies have shown that therapies that alleviate this excitatory imbalance could potentially reduce neuronal damage⁷.

Although treatments for excitotoxicity have been, and continue to be developed, inconsistencies in the effectiveness for various compounds across different studies have highlighted the complexities for treatment of TBI through systemic administration of therapeutic agents¹. These inconsistencies stem, at least in part, from an inadequate understanding of the pharmacokinetics and the therapeutic window for these compounds¹. Many of these challenges are bypassed in animal studies by administering potential therapeutic agents through cerebral injection or other nonsystemic methods. However, potential drugs for use in humans will likely involve systemic administration.

The multifaceted challenge of developing therapeutic agents for TBI that mitigate the complex effects of secondary injury while at the same time overcoming the potential problems of systemic administration can be addressed with a photodecaging strategy. In this approach, a drug can be administered systemically in a chemically inactive or ‘caged’ form, and then selectively decaged at the site of the injury using light irradiation. In principle, this method would allow the issues related to pharmacokinetics, tissue localization, and the therapeutic window to be addressed separately from the issues related to systemic side-effects. Additionally, rather than developing new therapeutics altogether, a photodecaging strategy could potentially allow delivery of the endogenous signaling molecules that are involved in a dysregulated biochemical pathway.

A critical feature of a photodecaging strategy for the treatment of TBI involves activation by light in the brain. Current methods to deliver high doses of light into the brain are still in development, although a few specific designs are already currently being implemented for use in photodynamic therapy and other forms of nonspecific light-based therapies⁸⁻¹⁰. Due to the thickness of the skull and brain tissue, the primary challenge in

delivering light into the brain is the scattering and absorption of the incident light. Current research has demonstrated that this filtering is wavelength-dependent, with ultraviolet and much of the visible spectrum being absorbed by skull and tissue while near-infrared (650 – 980 nm), is significantly transmitted. This suggests that new photodecaging strategies should have target absorptions at these wavelengths.

Summary of Dissertation Work

The goal of this work is to design new photochemical processes that can be implemented as decaging systems activated by near-infrared light. Model systems were initially developed using compounds that absorb in the ultraviolet, due to the greater synthetic accessibility and photochemical efficiencies associated with chromophores that absorb at these wavelengths. In Chapter 2, the photochemical decaging of carboxylic acids through a photoacid mechanism is explored, and model systems based on the 2-naphthol and Cy5 chromophores were designed that utilize ultraviolet and near-infrared light, respectively. The results of these initial studies reveal that some chemical decaging reactions are too slow to compete with the fast kinetics associated with photochemical processes. These findings led to new chemical designs that utilize a *phototriggered* decaging process. In this approach, an efficient photochemical reaction is used to generate a reactive intermediate, which then undergoes a relatively sluggish thermal decaging process. A key feature of this mechanism is that formation of the reactive intermediate is irreversible, and that the decaging step does not have to compete with the rapid photochemical kinetics. Extensive mechanistic studies are conducted in Chapter 3 on a system that utilizes the well-established trimethyl lock decaging process phototriggered by reduction of a benzoquinone. Although the benzoquinone system is activated by violet light, conclusions drawn by the mechanistic analysis naturally led to longer wavelength systems. Chapter 4 presents related systems that utilize a near-infrared absorbing chromophore known as methylene blue. Methylene blue derivatives that utilize a decaging process similar to the trimethyl lock were designed and synthesized, and it was found that photochemical reduction of the chromophore using red light results in rapid cyclization and release of a caged alcohol. These systems are expected

to be directly applicable for the future development of drug delivery systems for the treatment of TBI with near-infrared light.

References

- 1.Loane, D. J. & Faden, A. I. Neuroprotection for traumatic brain injury: translational challenges and emerging therapeutic strategies. *Trends Pharmacol. Sci.* **31**, 596–604 (2010).
- 2.Xiong, Y., Mahmood, A. & Chopp, M. Emerging treatments for traumatic brain injury. *Expert Opin. Emerg. Drugs* **14**, 67–84 (2009).
- 3.DeKosky, S. T., Blennow, K., Ikonovic, M. D. & Gandy, S. Acute and chronic traumatic encephalopathies: pathogenesis and biomarkers. *Nat. Rev. Neurol.* **9**, 192–200 (2013).
- 4.Dinh, M. M. *et al.* Redefining the golden hour for severe head injury in an urban setting: the effect of prehospital arrival times on patient outcomes. *Injury* **44**, 606–610 (2013).
- 5.Hook, G., Jacobsen, J. S., Grabstein, K., Kindy, M. & Hook, V. Cathepsin B is a New Drug Target for Traumatic Brain Injury Therapeutics: Evidence for E64d as a Promising Lead Drug Candidate. *Front. Neurol.* **6**, 178 (2015).
- 6.Duhaime, A. C. Exciting your neurons to death: can we prevent cell loss after brain injury? *Pediatr. Neurosurg.* **21**, 117–122; discussion 123 (1994).
- 7.Gibson, C. J., Meyer, R. C. & Hamm, R. J. Traumatic brain injury and the effects of diazepam, diltiazem, and MK-801 on GABA-A receptor subunit expression in rat hippocampus. *J. Biomed. Sci.* **17**, 1–11 (2010).
- 8.Naeser, M. A., Saltmarche, A., Kregel, M. H., Hamblin, M. R. & Knight, J. A. Improved Cognitive Function After Transcranial, Light-Emitting Diode Treatments in Chronic, Traumatic Brain Injury: Two Case Reports. *Photomed. Laser Surg.* **29**, 351–358 (2011).
- 9.Morries, L. D., Cassano, P. & Henderson, T. A. Treatments for traumatic brain injury with emphasis on transcranial near-infrared laser phototherapy. *Neuropsychiatr. Dis. Treat.* **11**, 2159–2175 (2015).
- 10.Henderson, T. A. & Morries, L. D. Near-infrared photonic energy penetration: can infrared phototherapy effectively reach the human brain? *Neuropsychiatr. Dis. Treat.* **11**, 2191–2208 (2015).

*Chapter 2*THE UTILITY OF EXCITED-STATE PROTON TRANSFER IN THE
DEVELOPMENT OF NOVEL PHOTOCHEMICAL REACTIONS**Abstract**

Although photochemical reactions that utilize less than 40 kcal/mol (~ 700 nm) of excitation energy are rare, their development could be highly applicable as photochemical drug release strategies for biological applications where higher-energy processes must be avoided. Investigations in the use of excited-state proton transfer as a low-energy process capable of catalyzing photochemical transformations are shown here. Guided by the results of our initial strategies, a kinetic model is developed that naturally leads to specialized intramolecular systems that undergo general-acid catalysis in the excited state.

1. INTRODUCTION

New drug release strategies that are capable of delivering therapeutics with spatiotemporal control using light could overcome many of the challenges in drug design concerning bioavailability, localization to target tissues, and systemic side effects. In particular, photocontrolled release of drugs in the brain could mitigate current challenges in the treatment of traumatic brain injury (TBI)^{1,2}. TBI is a result of a traumatic event that leads to a localized section of the brain being damaged typically near the scalp³.

There are currently no known therapeutics that directly treat traumatic brain injury, primarily due to systemic side effects of potential drugs in other parts of the brain and body and due to the difficulty of localizing drugs in the brain^{1,2}. The latter is controlled by the blood-brain barrier, which limits diffusion of small molecules into the brain through a process that is not well understood. The design of therapeutics that are inactive until treatment with light would allow new drug designs and strategies to target the challenges of delivery independently of the challenges associated with systemic side-effects. Furthermore,

a general light-activation strategy could be designed to release a variety of drugs using the same deactivating group which would make this a broadly applicable tool for drug design.

Current methods to deliver high doses of light into the brain are still in development, although a few specific designs are already being implemented for use in photodynamic therapy and other forms of nonspecific light-based therapies^{4,5}. Due to the thickness of the skull and brain tissue, the primary challenge in delivering light into the brain is the scattering and absorption of the incident light⁶. Current research has demonstrated that this filtering is wavelength-dependent, with ultraviolet and much of the visible spectrum being absorbed by skull and tissue while near-infrared (600–980 nm) is significantly transmitted. This suggests that new light-activated drug release strategies should have target absorptions at these wavelengths.

A significant challenge in the development of light-activated drug release strategies that absorb in the near-infrared is the very little energy associated with these wavelengths of light. Many photochemical reactions that result in heterolytic bond cleavage processes are either initiated by, or directly a result of, higher-energy processes. Near-infrared light is generally incapable of delivering the required amount of energy that would allow the system to participate in these processes. Therefore, the effective design of new strategies will also involve the development of new photochemical mechanisms that are uniquely capable of activation by low-energy light.

The main challenge in designing new photochemical mechanisms that are activated by near-infrared light is overcoming low energy efficiency. For instance, an ideal highly-efficient photochemical system would need less than 10 kcal/mol of energy to change the rate of drug release from occurring on the time scale of months to that of seconds. This amount of energy corresponds to a wavelength of roughly 3000 nm, which is much lower in energy than the near-infrared, which has closer to 30 kcal/mol. Photoreactions initiated by ultraviolet light often generate radical intermediates through cleavage of strong bonds with energies up to 90 kcal/mol. However, the ultimate photoproducts are typically closed-shell molecules that result from eventual radical recombination. This radical recombination process can be hugely exothermic, resulting in energy wasting and low efficiency.

Although primary heterolytic bond-cleavage processes are less common in photochemical reactions than radical processes, there are well understood systems that are compatible with the energy requirements of near-infrared light. One such example is the photoacid effect⁷⁻¹³, where a mildly acidic function group, usually an aromatic alcohol, is made much more acidic during the excited state after light absorption. On a chemical level, the acidity corresponds to heterolytic cleavage of an O-H bond, leading to generation of H⁺ and the deprotonated alcohol. In the ground state for most aromatic alcohols, this process favors the starting material over the products by many orders of magnitude. However, in the excited state, the equilibrium can be shifted more toward the products. For instance, for 2-naphthol¹⁴, the excited-state favors a shift in the pK_a equilibrium by 10⁶. Even though 2-naphthol is excited by ultraviolet light, corresponding to energies of ~ 80 kcal/mol, this shift in the equilibrium is established using less than 10 kcal/mol. The remaining photonic energy is emitted from the naphtholate anion as fluorescence or heat.

Although the photoacid phenomenon is a highly-studied area of research, near-infrared absorbing organic molecules that participate in the effect have not been reported. In principle, an appropriate dye would be expected to have an aromatic alcohol that becomes more acidic upon absorption of near-infrared light, generating the deprotonated form of the dye in the excited-state and a proton. The generated proton can then be used as an acid catalyst of a chemical process that results in drug release. Since acid-base catalysis is a fundamental concept that has been studied for decades, many potential acid catalyzed processes can be envisioned to result in the release of a wide variety of functional groups¹⁵⁻

21

The research presented here addresses certain advances that have been made in the development of new photoacid-based drug delivery systems. A photochemical design that utilizes a photoacid mechanism to cleave t-butyl esters is initially detailed. Model systems using 2-naphthol and a longer-wavelength cyanine dye have been developed. The synthesis and photolysis of these compounds are discussed in detail. Key concepts that were discovered through the development of these systems that could be useful for the improved design of future photoacid-based strategies are outlined. In the final two sections of this

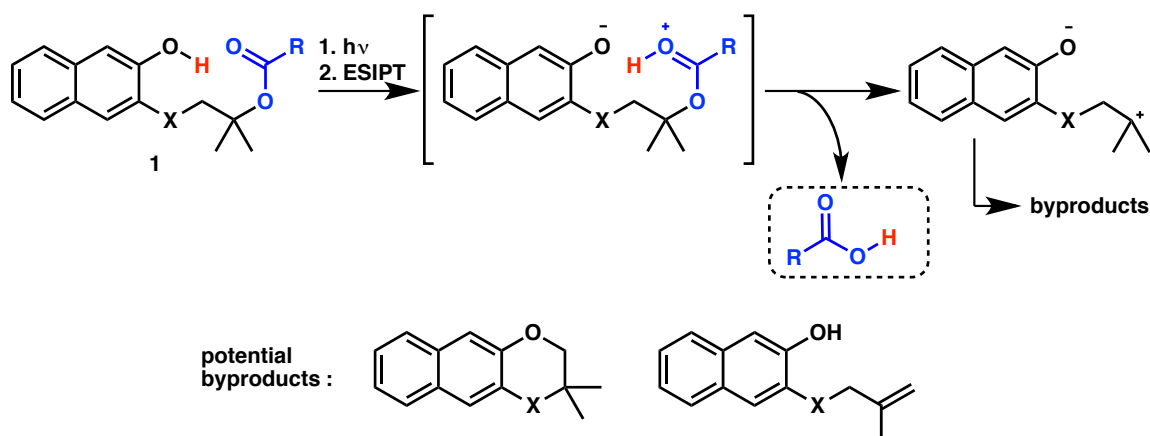
chapter, these concepts are applied toward the development of improved intramolecular and bimolecular systems.

2. T-BUTYL ESTER MODEL SYSTEMS

2.1 General Chemical Design

The initial design of a model system was envisioned to involve the direct transfer of a photoacidic proton to a tethered functional group that would then undergo cleavage of a bond that results in drug release. Although a variety of functional groups could be compatible with this concept, a t-butyl ester was chosen based on a few key factors. t-butyl esters decay under acidic conditions through a well-known mechanism that involves heterolytic C-O bond cleavage with generation of a carboxylic acid and the relatively stable t-butyl carbocation that ultimately gets trapped by a nucleophile or deprotonated to form a C-C double bond^{20,21}. That the process releases a carboxylic acid was desirable since a wide variety of therapeutic agents contain the carboxylic acid moiety and its protection as an ester is expected to generally result in drug deactivation. Additionally, t-butyl esters are thermally stable compounds, and are more resistant to nucleophilic or hydrolytic exchange than other esters. Similarly, they are generally unaffected by environmental changes in redox or acidity that would be present in a biological system.

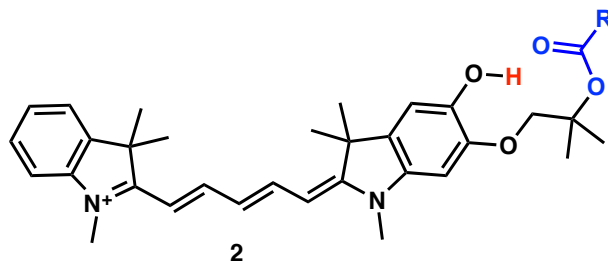
Another feature of the initial molecular design involves the exposure of a high *effective* molarity of acidic proton to the t-butyl ester by enforcing more conformational rigidity in the tether between the ester and the photoacidic alcohol in a way that would favor an unstrained geometry during the excited-state proton transfer²². It is well known that different ring sizes contain varying levels of strain in their sigma bond framework, with six and ten membered rings being energetically optimal structures. A design containing a six-membered ring would not be possible due to the fact that there are necessarily more than six atoms in a ring containing both an aromatic alcohol and a t-butyl ester. Therefore, a molecule that would generate a ten-membered ring was considered optimal. The result of these requirements is the prototype molecule **1** shown in Scheme 1, where R can be interchanged to accommodate different therapeutic agents, and X can be O, CH₂, or any other compatible



Scheme 1. General design of the initial model system containing a 2-naphthol photoacid.

group that may perhaps lead to improved photochemistry or ease of synthesis. Results from molecular-mechanics calculations for **1** suggest that the structure with $X = O$ is less strained than the structure with $X = CH_2$. For this reason, the initial synthetic design of **1** incorporates this element.

The chemical design of **1** is shown with a 2-naphthol photoacid, although in principle it could be any aromatic chromophore that has an available ortho position to the acidic alcohol. 2-naphthol was considered to be ideal for a model system, since its photoacidity is well-studied and can be directly observed using standard fluorometry¹⁴. Although many phenols are also known to be photoacidic, 2-naphthol has a maximum absorption at 330 nm compared to phenol which has a maximum at 275 nm. This is anticipated to improve the photolysis and minimize the occurrence of deleterious photochemical processes. In addition to a naphthol-based model system, longer-wavelength designs, such as **2**, containing a cyanine dye, will also be discussed.



As shown in Scheme 1, photolysis of **1** is expected to result in excited-state intramolecular proton transfer (ESIPT) from the naphthol to the *t*-butyl ester, which is then expected to undergo C-O heterolytic bond cleavage to generate a tertiary carbocation and

release of a carboxylic acid. A number of different byproducts of the naphthol chromophore can be envisioned, and some likely candidates are also shown in Scheme 1.

2.2 The 2-Naphthol Model System

Synthesis

The synthesis of **1** ($X = O$) is shown in Figure 1A for a derivative containing a hydrocinnamic ester. Release of hydrocinnamic acid upon photolysis was expected to be easily followed by NMR or HPLC, but to not perturb the course of the photochemical

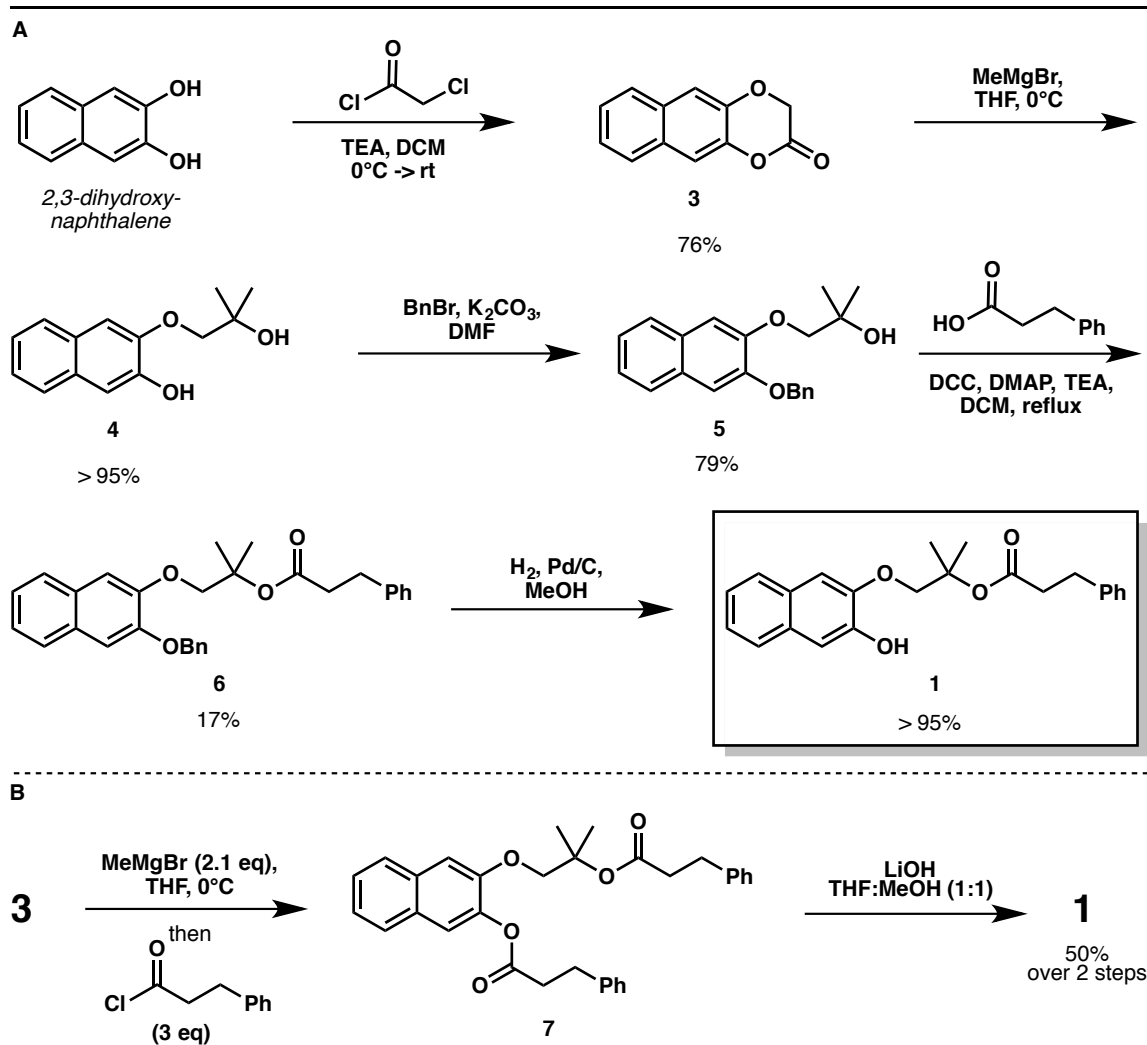


Figure 1. Synthesis of naphthol-based model system **1**. **A)** Initial approach using benzyl protection. **B)** Alternate two-step one-pot procedure.

reaction. Treatment of commercially available 2,3-dihydroxynaphthalene with chloroacetylchloride results in good yields of lactone **3**, which can be alkylated with methyl Grignard to yield quantitative formation of the diol **4**. Initially, benzyl protection of the phenol to generate **5**, followed by DCC coupling with hydrocinnamic acid to form **6**, and deprotection under hydrogenation conditions yielded the desired product **1** in a straightforward fashion. However, the DCC coupling was low yielding and inconsistent, so an alternative procedure was used in most cases as shown in Figure 1B. After treatment of **3** with methyl Grignard, quenching with hydrocinnamoyl chloride resulted in a decent yield of diester **7**, which could be selectively saponified to produce **1** in moderate, but consistent, overall yields.

Spectroscopy & Photolysis

A signature of the photoacid effect is emission from the deprotonated state which occurs with a Stokes shift that is correlated with the excited-state acidity according to the Förster cycle, which is demonstrated in Figure 2 for 2-naphthol¹⁴. In this thermodynamic cycle, the excited-state acid-base equilibrium (pK_a^*) can be obtained if the ground-state acid-base equilibrium (pK_a), excitation wavelengths ($h\nu^1$ and $h\nu^2$) and emission wavelengths ($h\nu^{-1}$ and $h\nu^{-2}$) can be measured or approximated.

Shown in Figure 3 are absorbance and fluorescence spectra for compound **1** recorded

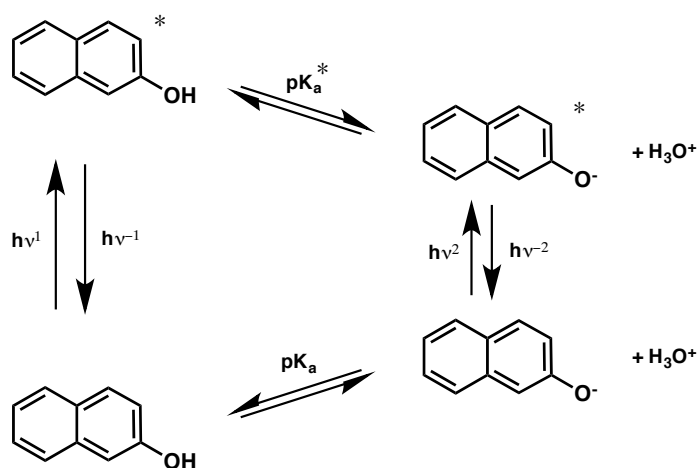


Figure 2. Förster cycle used for the determination of pK_a^* from the known pK_a , excitation wavelengths ($h\nu^1$ and $h\nu^2$) and emission wavelengths ($h\nu^{-1}$ and $h\nu^{-2}$) for 2-naphthol.

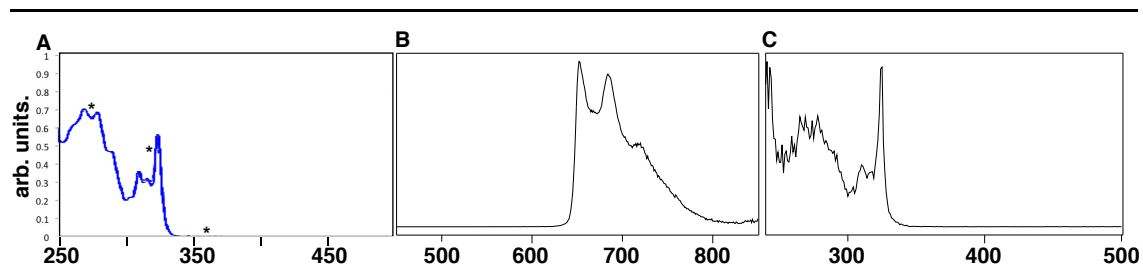


Figure 3. Spectra for **1** in acetonitrile. **A)** Absorbance spectrum. **B)** Emission spectrum due to excitation at 300 nm. **C)** Excitation spectrum for the emission at 650 nm.

in acetonitrile. The absorbance spectrum (Figure 3A) displays three primary bands at 260, 325, and 360 nm (starred), with the latter being weakly discernable in Figure 3. A strong emission between 650 and 800 nm is observed upon excitation into these bands, as shown in Figure 3B. Shown in Figure 3C is the excitation spectrum for this long-wavelength emission. There is a very close resemblance to the absorption spectrum, indicating that the emission occurs due to excitation of **1**.

Compound **1** was originally designed to possess a ten-membered ring in order to favor a cyclized conformation with a hydrogen bond between the acidic alcohol and the *t*-butyl ester. Shown in Figure 4 is the effect of varying temperature on the NMR spectrum for **1** in CD₃CN, and in particular the change in the chemical shift for the phenolic proton at ~ 7 ppm. Similar trends with increasing temperature have frequently been indicative of an equilibrium between open and closed hydrogen-bonded conformations²³.

Photolysis of **1** has been carried out under a variety of conditions, and in general yields a complex mixture of products. In aqueous systems or mixed-aqueous systems, excitation of a 1 mM solution of **1** at 355 nm with the focused beam from a 500 W high-pressure mercury lamp in degassed solution yields very slow consumption of **1** with half-lives on the order of ten hours. Although quantum yields were not measured directly, we assume they are very low based on similar photolysis times from more efficient systems. In nonaqueous solvents, photolysis results in the rapid decay of **1**, with the formation of hydrocinnamic acid evident by HPLC analysis along with a complex mixture of byproducts from the chromophore. In aqueous solvent systems, the decay is much slower, and does not result in the formation of hydrocinnamic acid.

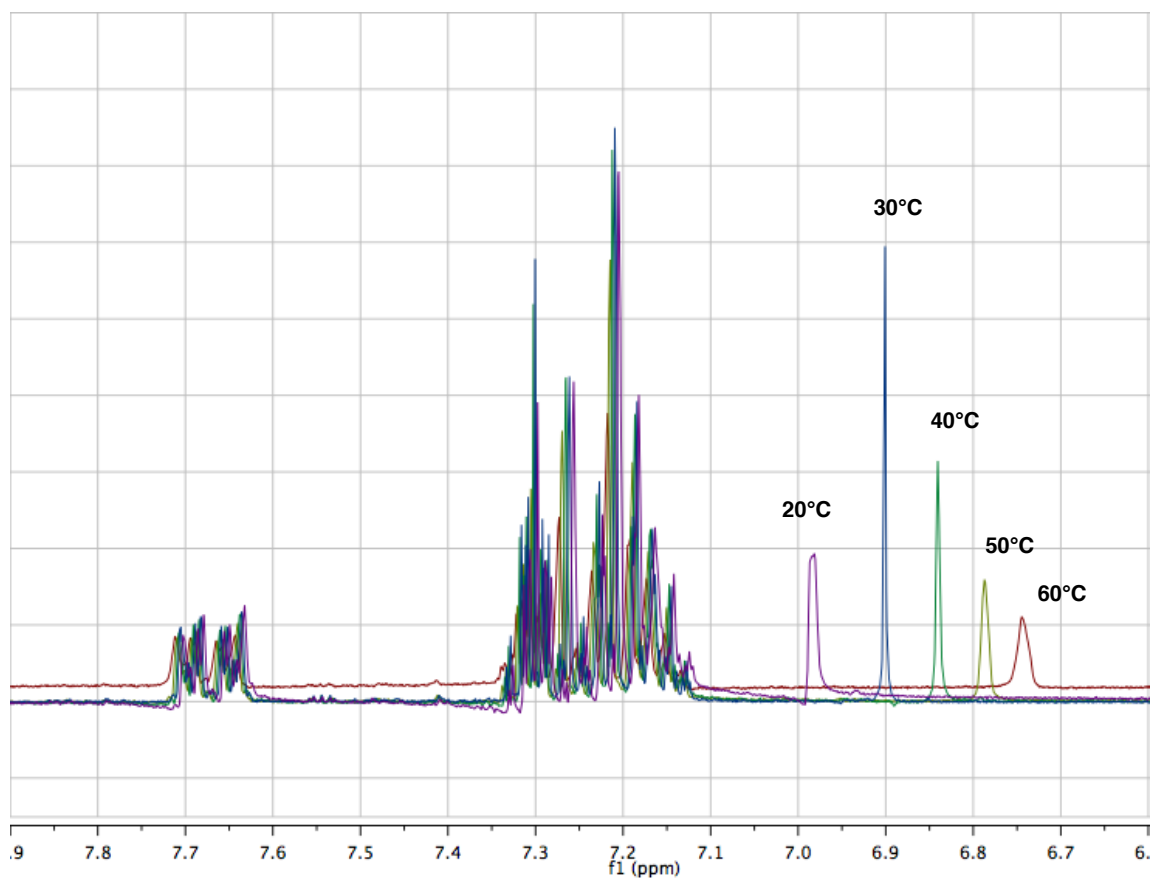
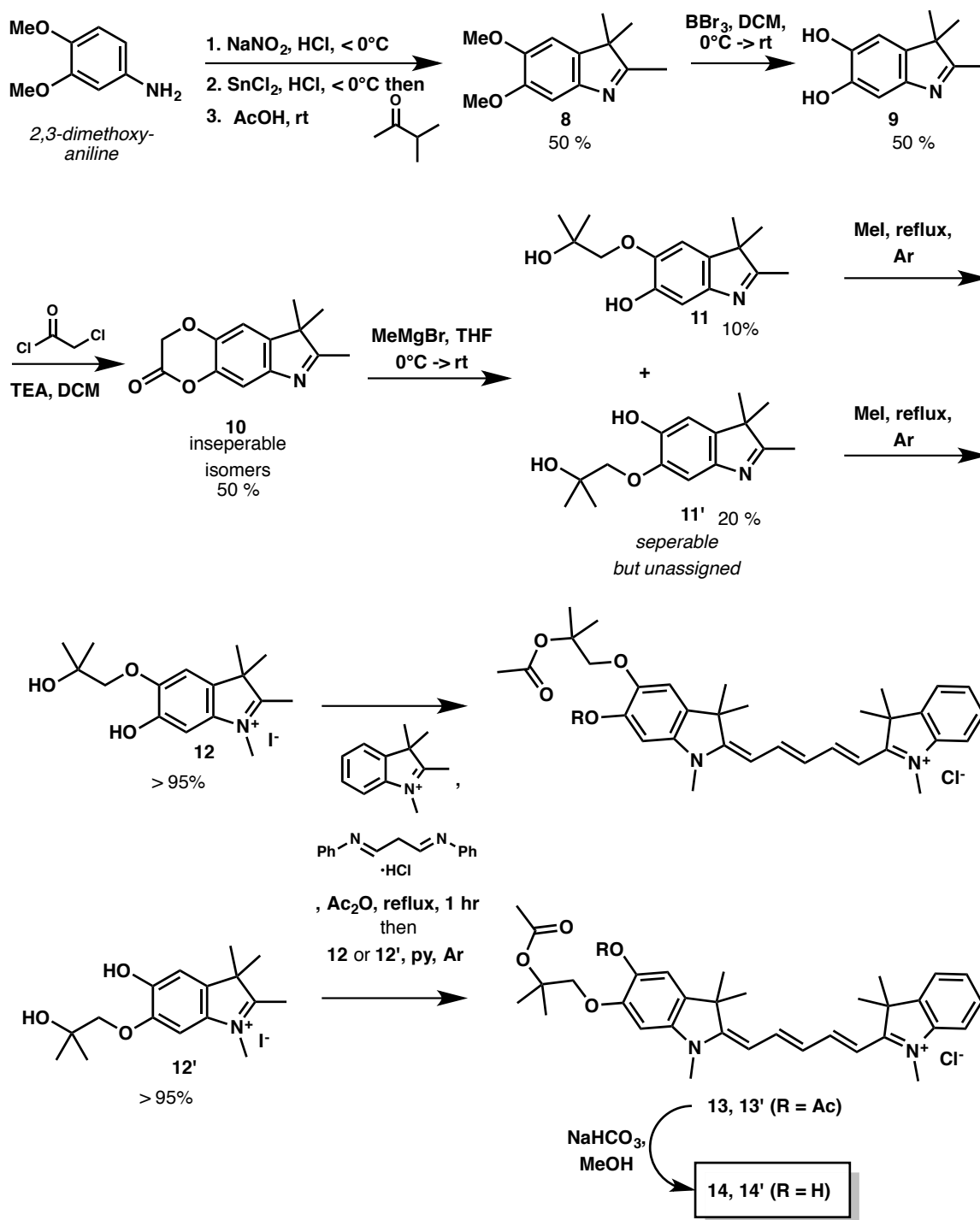


Figure 4. $^1\text{H-NMR}$ spectrum for **1** in CD_3CN at varying temperatures.

2.3 The Cy5 Model System

Synthesis

Compounds analogous to **1** based on the Cy5 chromophore were also synthesized as shown in Scheme 2. 2,3-dimethoxyaniline is initially converted to the aryl hydrazine and treated with 3-methyl-2-butanone to generate the dimethoxy-2,3,3-trimethylindolenine **8** in generally good yields. Deprotection of the methoxy groups with boron tribromide yields catechol **9**, which is highly unstable to mildly basic conditions. Careful treatment of the catechol with chloroacetyl chloride then generates an inseparable mixture of isomers **10**, which can be treated with methyl Grignard to generate a separable mixture of the diols **11** and **11'**. Although these compounds were isolated, assignment of the regioisomers was never

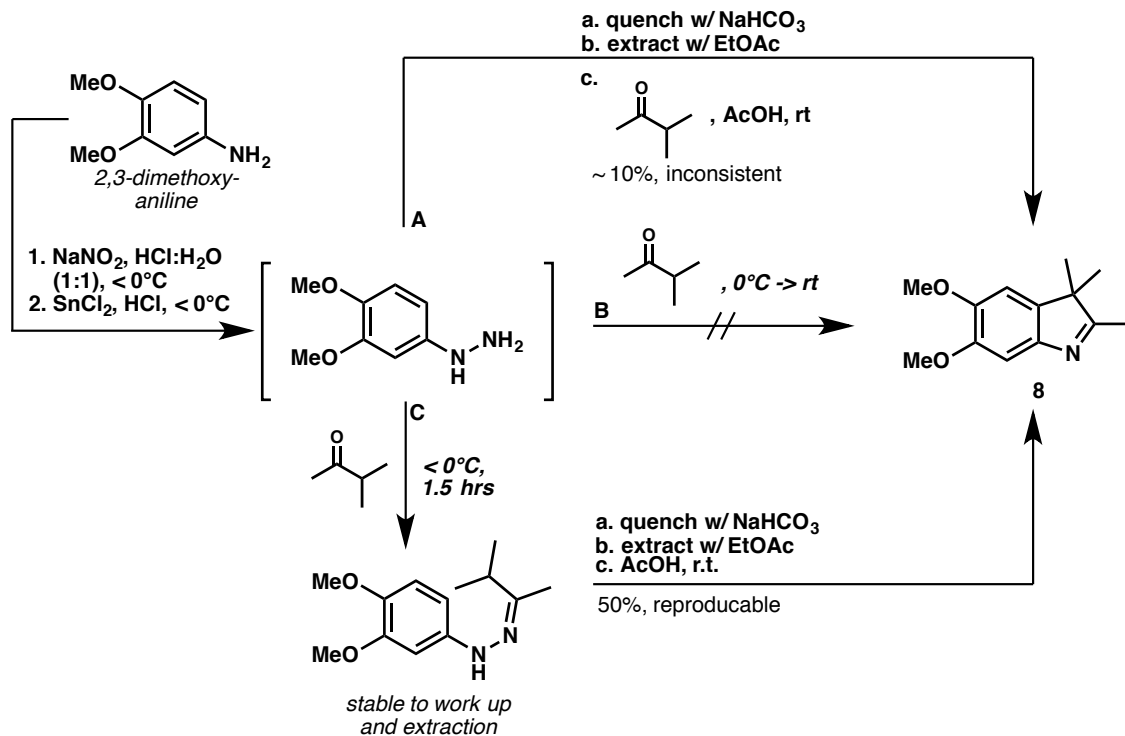


Scheme 2. Synthesis of Cy5-based model systems 14 and 14'.

made. **11** and **11'** can be refluxed in methyl iodide under deoxygenated conditions, which generates the salts **12** and **12'** in quantitative yields, and converted to the asymmetric cyanine dyes using 1,2,3,3-tetramethyl-3H-indolinium iodide and malondialdehyde bis(phenylimine). These last conditions are conducted in acetic anhydride, and result in the diacetylated products **13** and **13'**. Selective removal of the phenolic acetate is accomplished with bicarbonate in aqueous methanol to yield **14** and **14'**, presumably as chloride salts after washing with brine.

Although an ester more distinguishable than acetate would have been preferred for photolysis studies of **14** and **14'**, many attempts to install a group other than acetate using this and other protocols were unsuccessful. Attempted esterification of **11** and **11'** resulted in amide formation on the indole nitrogen, and compounds **12** and **12'** were similarly unstable to standard coupling conditions, although specific side products were not identified. The formation of **13** and **13'** with other simple esters was possible by carrying out the reaction with some anhydrides other than acetic anhydride, but solvent level amounts were a requirement, making the installation of other groups impractical and in many cases much lower yielding than installation of acetate groups.

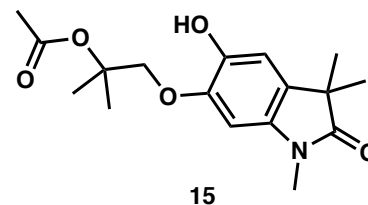
Formation of the indolenine **8** was also challenging due to the instability of the electron rich aryl hydrazine (Scheme 3). Standard attempts to quench the hydrazine formation with mild base and extraction led to low and inconsistent yields (Scheme 3, path **A**). Similarly, attempting to perform the Fischer indole formation from *in situ* formed aryl hydrazine without an intermediate workup was completely unsuccessful (Scheme 3, path **B**). However, conversion of the *in situ* aryl hydrazine to the hydrazone, which is typically the first step of the Fischer indole formation, and then performing a basic quench and extraction (Scheme 3, path **C**) was found to consistently generate decent yields of **8** due to the greater stability of the hydrazone to the workup conditions.



Scheme 3. Optimization of the Fischer indole formation of **8**. In path **A**, the aryl hydrazine was found to be unstable to basic workup conditions. Attempting to bypass the workup failed (path **B**), but trapping out as the aryl hydrazone in path **C** led to reproducibly decent yields.

Photolysis

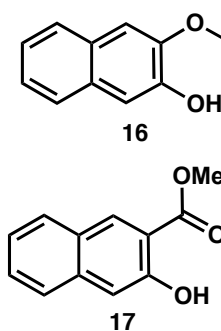
Photolysis of **14** and **14'** was generally carried out using the focused beam from a 500 W high-pressure mercury lamp with wavelengths greater than 550 nm or with a Luzchem irradiation chamber using standard visible fluorescent bulbs. Irradiation in degassed methanol, acetonitrile, water, or benzene resulted in slow photobleaching of the dye with half-lives of greater than twenty hours. The formation of deacetylated products was not detected using HPLC-MS or NMR analysis, suggesting the photoacid reaction to be very inefficient for these systems. When conducted in degassed benzene solvent, the photobleaching process was cleaner, and product **15** was obtained as a major product, indicating that slow oxidation of the cyanine chain occurs at least in



some cases without release of the acetate. Similar decomposition pathways for cyanine dyes have been reported^{24,25}.

2.4 Discussion

Although photolysis of the 2-naphthol system **1** results in the desired cleavage of the t-butyl ester and the formation of hydrocinnamic acid, the photoreaction is efficient only in the aprotic solvent acetonitrile. Reactions conducted in water led to decay of **1**, but hydrocinnamic acid was not observed in the product mixture. As shown in Scheme 1, the excited-state process is envisioned to occur through two primary steps. Initial proton-transfer from the excited naphthol to the t-butyl ester results in formation of a zwitterion that then undergoes C-O bond cleavage of the t-butyl ester in a second step. The second step of this process is assumed to be irreversible, while the latter could foreseeably return to starting material. That the process occurs in two steps is evidenced by the fluorescence emission of **1** in acetonitrile (Figure 3B). The Stokes shift has been estimated to be > 250 nm, based on the long-wavelength edge of the absorbance (400 nm) and the short wavelength edge of the emission (650 nm). This large a Stokes shift is irregular for general aromatic systems, and we note that the reported fluorescence emission of **16**, an analogous compound which lacks the t-butyl ester, occurs at 343 nm in ethanol, with no reported emission at longer wavelengths²⁶. Shown in Figure 3A, this wavelength is similar to the longest-wavelength absorption band for **1**, and thus likely represents emission from the S₁ state in the absence of excited-state proton transfer. In comparison, the emission of **1** at 650 nm is very similar to that reported from compound **17**, which occurs at a maximum wavelength of 650 nm²⁷. The large Stokes shift was attributed to ESIPT from the naphthol to the pendant ester, which results in emission from a tautomeric form of **17**. Similarly, emission from **1** is thought to occur from a state that has undergone proton transfer from the naphthol to the t-butyl ester, as shown in Scheme 1. That no emission was observed at shorter wavelengths suggests that population of the zwitterionic state is efficient. However, the overall conversion of **1** to the desired photoproducts is



inefficient, suggesting that C-O bond-cleavage in the zwitterionic intermediate is too slow to compete with back proton transfer to the naphtholate.

Emission from **14** or **14'** could not be recorded due to instrumental limitations preventing detection at the long wavelengths encountered with these compounds. It is therefore unclear whether the low reaction efficiency of these derivatives is due to the excited-state proton-transfer or the t-butyl ester cleavage process. For the 2-naphthol system, efficient excited-state proton-transfer has been thought to be correlated with the larger π -system of naphthalene, which allows better delocalization of the negative charge in the excited naphtholate^{9,27}. Shown in Figure 5 in blue are positions on **1**, **14**, and **14'** that can accommodate the negative charge using closed-shell resonance structures. Although meta effects are certainly more important for excited state systems than ground-state systems, previous evidence has demonstrated that for 2-naphthol, much of the negative charge lies at the ortho/para positions⁹. The π -systems between the aromatic alcohol in **14** and **14'** are connected to the cyanine π -system, but there are no closed-shell resonance structures that can be drawn that allow the phenolate to delocalize negative charge into the cyanine chain. This suggests that there may be less driving force for excited-state proton-transfer from **14** and **14'** compared to **1**. However, excited states are often more complicated than these simple models and more investigations would need to be carried out to support these conclusions.

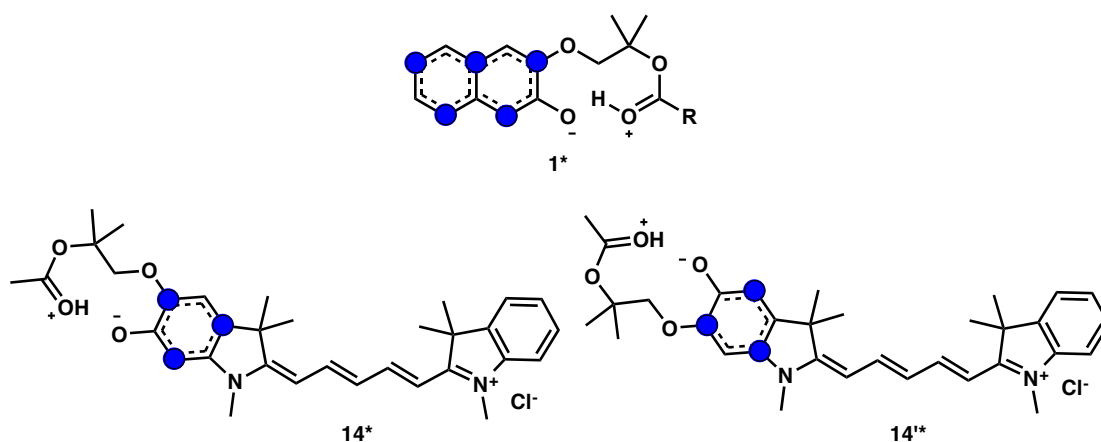


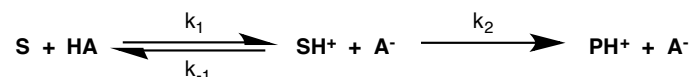
Figure 5. Delocalization of negative charge in the anions of **1***, **14***, and **14'*** onto the labelled positions.

3. GENERAL-ACID CATALYZED SYSTEMS

3.1 Introduction

The initial studies of photoacid systems containing tethered t-butyl esters highlight the importance of the kinetics for the steps following ESIPT. For instance, although compound **1** is found to readily undergo excited-state protonation of the t-butyl ester side chain (Scheme 1), low efficiency for cleavage of the protonated ester occurs if the kinetics for this reaction are too slow to compete with back proton-transfer. These conclusions have led to the development of second-generation designs that involve faster reaction than C-O bond cleavage of protonated t-butyl esters. More specifically, systems that are known to undergo general-acid catalyzed processes were targeted.

Acid-catalyzed reactions can be defined according to the two-step model in Scheme 4, where **S** refers to substrate, **P** refers to product, and **HA** is the catalytic acid²⁸. Note that



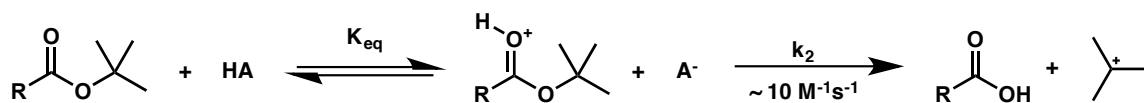
Scheme 4. Two step model for acid catalyzed reactions that transform substrate **S** into product **P** with the acid **HA**.

the final step of the catalytic process, regeneration of the acid catalyst, has been omitted for clarity since this step does not affect the analysis. Broadly speaking, acid-catalysis can be defined as either general or specific. Specific-acid catalyzed mechanisms describe situations where the second-order rate constants k_1 and k_{-1} are much greater than k_2 , such that the initial equilibrium (k_1/k_{-1}) is established much more quickly than product is formed via k_2 . Under these conditions, the ratio (k_1/k_{-1}) can be substituted by the equilibrium constant ($K_a^{HA}/K_a^{SH^+}$), and the preequilibrium approximation can be applied to describe the kinetics of the overall reaction. The rate equation for the concentration of **P** is described by Eq. 1:

$$[\text{P}] = [\text{S}]_0 \cdot (1 - e^{-K_{eq} \cdot k_2 \cdot [\text{HA}] \cdot t}) \quad \text{where } K_{eq} = \frac{K_a^{HA}}{K_a^{SH^+}} \quad (1)$$

As shown in Scheme 5, the A1 mechanism that describes the hydrolysis of t-butyl esters is known to be specific-acid catalyzed in water, meaning that the proton-transfer

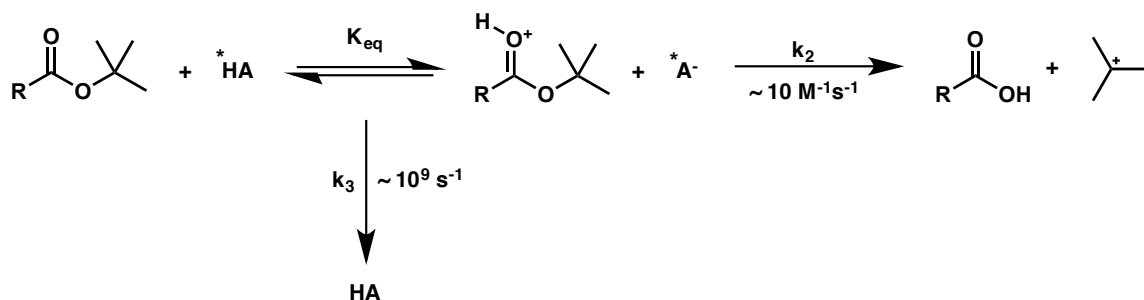
equilibrium is established much more quickly than C-O bond cleavage occurs ($k_2 \sim 10 \text{ M}^{-1} \text{ s}^{-1}$)^{20,21}. A first-order rate constant ($K_{eq} \cdot k_2 \cdot [\text{HA}]$) can therefore be calculated for a given pH, and it is clear that for each order-of-magnitude shift in K_{eq} , there will be an order-of-magnitude shift in the overall rate constant.



Scheme 5. A1 mechanism for the hydrolysis of t-butyl esters described by the model in Scheme 4.

For an excited-state acid ($^*\text{HA}$), the specific-acid catalyzed process competes directly with deactivation of the excited state (k_3), as shown in Scheme 6. For 2-naphthol, the singlet-excited state is known to decay with a rate constant of 10^9 s^{-1} ¹⁴. The formation of product **P** described by this model is given by Eq. 2, assuming again that the excited-state proton-transfer equilibrium is established faster than excited-state decay and product formation. In this expression, if $k_2 \cdot K_{eq} \cdot [^*\text{HA}] \gg k_3$, then Eq. 2 reduces to Eq. 1, neglecting the excitation rate constant k_{hv} .

$$[\mathbf{P}] = [\mathbf{S}]_0 \cdot k_{hv} \cdot \left(1 - \frac{k_2 \cdot K_{eq} \cdot [^*\text{HA}]}{k_2 \cdot K_{eq} \cdot [^*\text{HA}] + k_3}\right) \cdot e^{-(k_2 \cdot K_{eq} \cdot [^*\text{HA}] + k_3) \cdot t} \quad (2)$$



Scheme 6. A1 mechanism for the hydrolysis of t-butyl esters in the excited-state through ES IPT.

General-acid catalyzed processes are described by the opposite situation, where k_2 is similar to or faster than $k_1 \cdot [\text{HA}]$. Under these circumstances, the observed rate constant for the overall reaction involves $k_1 \cdot [\text{HA}]$ and, if similar in magnitude, k_2 as well. Two classic

experiments exist to expose a general-acid catalyzed mechanism. If the reaction rate constant is dependent upon the concentration of the general-acid, [**HA**], at constant pH, then a general-acid mechanism is at least partially active. An example of this would be to measure the rate of reaction at different buffer concentrations. Since direct proton-transfer between **HA** and **S** is part of the observed rate constant for the general-acid catalyzed process, a second common feature for this mechanism is a dependence of the rate constant on the pK_a for the general acid (at constant pH), given by the Brønsted α value²⁸. The Brønsted equation (Eq. 3) is a linear free-energy relationship that assumes the activation energy for proton transfer correlates directly with the reaction driving force. The Brønsted α value ranges between 0 and 1, and is often interpreted as the degree to which the proton is transferred at the transition state. The existence of a general-acid catalyzed pathway for a reaction implies that the two steps, proton-transfer and product (**PH**⁺) formation, are concerted. However, it does not distinguish between concerted asynchronous reactions, where the transition state contains a degree of proton-transfer but not of product formation, and concerted synchronous reactions, where the transition state contains degrees of proton-transfer and product formation.

$$\log(k) = \alpha \cdot \log(K_a) \quad (3)$$

Although both general-acid catalysis and excited-state proton-transfer have been studied for decades, there are no known examples of an excited-state acid being used in a general-acid catalyzed process. However, the results of our previous investigations with *t*-butyl ester substituted photoacids reveal that a general-acid mechanism could potentially address the problem of poor quantum efficiency by demonstrating with compound **1** that the proton-transfer process is efficient but that cleavage of the C-O bond in the protonated *t*-butyl ester is not (Scheme 1). Within the current framework, the photoreaction of **1** represents a specific-acid catalyzed process with kinetics that are dictated by k_2 in Scheme 6. In general, specific-acid catalyzed processes are going to possess low values for k_2 , resulting in low efficiencies on a photochemical pathway.

Another key point that is exposed by the models in Schemes 5 and 6 is that for an excited state acid-catalyzed process, the ground state reaction may also be occurring simultaneously. This is typically not the case for photochemical reactions since

photochemical processes often have rate constants that exceed their ground-state counterparts by many orders-of-magnitude (e.g. a Norrish II reaction is never going to happen thermally, yet HAT on the triplet surface occurs with rate constants $> 10^7 \text{ s}^{-1}$)²⁹. For photoacids, however, excited state acidities may only be a few orders of magnitude greater than their ground-state counterparts, and this fact in combination with the other factors in Eq. 2 that slow down the photochemical reaction, i.e., the rate of excited-state population (k_{hv}) and the quantum efficiency ($\frac{k_2 \cdot K_{eq} \cdot [*HA]}{k_2 \cdot K_{eq} \cdot [*HA] + k_3}$), can make design of photoacid-catalyzed systems difficult. The former parameter (k_{hv}) affects only the excited state kinetics, and represents a combination of the photon flux and the extinction coefficient of **HA**. Therefore, experimental systems that maximize these variables are preferred. The quantum efficiency ($\frac{k_2 \cdot K_{eq} \cdot [*HA]}{k_2 \cdot K_{eq} \cdot [*HA] + k_3}$) contains k_2 , which appears in both the ground-state and excited-state kinetics and therefore can't necessarily be maximized to favor the excited-state process. However, the rate constant k_3 is present only in the photochemical process, and represents the intrinsic lifetime of the excited state. Decreasing this value therefore selectively increases the rate constant for the photochemical pathway.

Compounds **18** – **21** in Figure 6 were synthesized in order to study the possibility of excited state general-acid catalysis. All four systems are based on 1-naphthol, which is a stronger excited-state acid than 2-naphthol. Although these compounds are not specifically designed to release a drug, they are envisioned to be adaptable for such purposes. Development of longer wavelength systems are still in progress, and will be described in other reports.

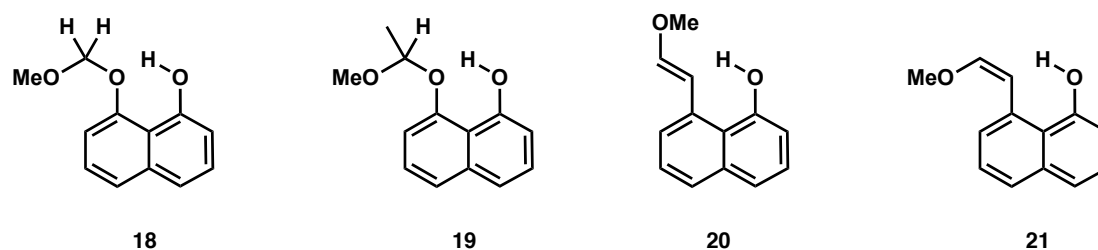


Figure 6. Compounds that were studied to probe the possibility of ESIPT general-acid catalysis

3.2 Oxocarbenium Ion Formation

Synthesis

The synthesis of compound **18** occurs in a single step by treating 1,8-dihydroxynaphthalene with MOM-Cl (Figure 7A). Similarly, the acetal **19** can be prepared using ethyl vinyl ether in the presence of catalytic PPTS (Figure 7B). Synthesis of vinyl ethers **20** and **21** was ultimately accomplished using a Wittig reaction (Figure 7C). Beginning with 1,8-naphthalic anhydride, five previously reported steps furnish aldehyde **22**, which can be converted to an inseparable mixture of isomers of the vinyl ether **23**. Deprotection of the phenol occurs under basic conditions, resulting in a separable mixture of vinyl ethers **20** and **21**.

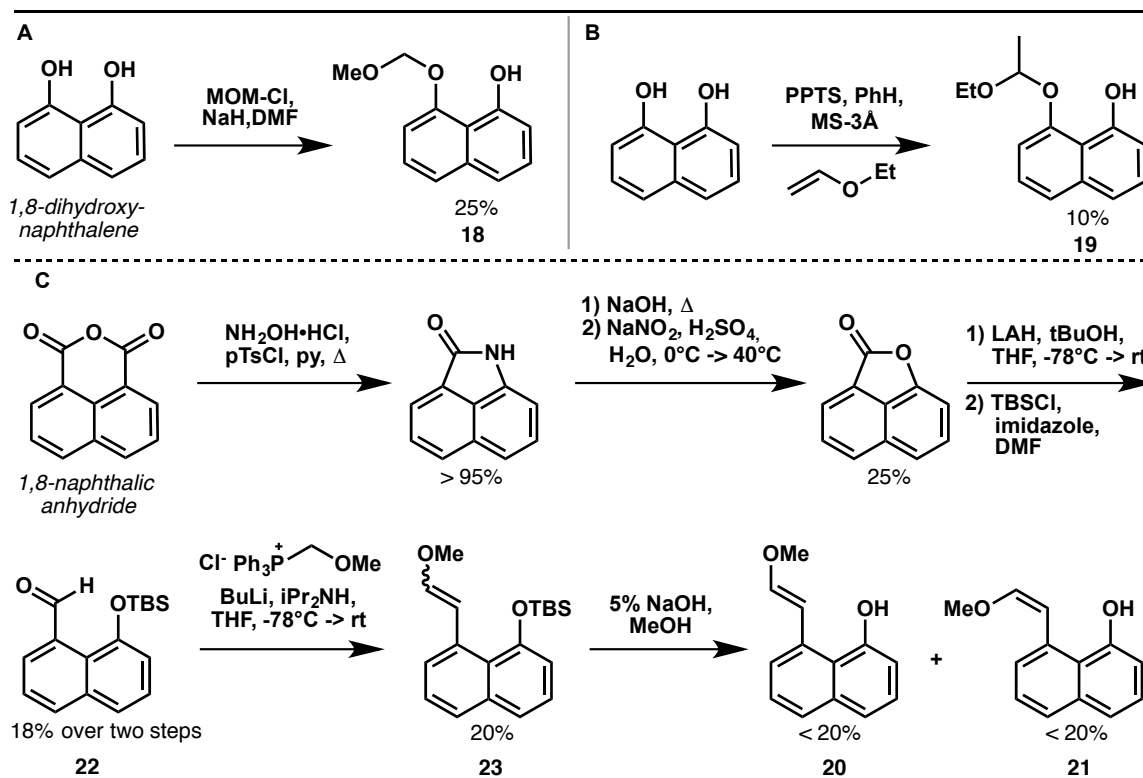
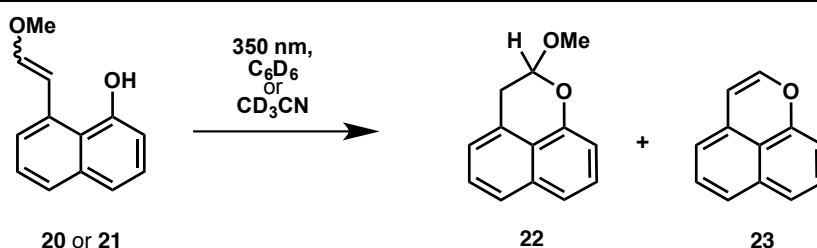


Figure 7. Synthesis of compounds **18** - **21**.

Photolysis

Photolysis studies were generally conducted using 350 nm excitation from the collimated beam of a 500 W high-pressure mercury lamp. When **18** was photolyzed in D₂O and mixed D₂O solvent systems under degassed conditions, the formation of methanol, formaldehyde, and 1,2-dimethoxyethane is evident. Multiple byproducts of the chromophore were also present and were difficult to characterize. Although methanol and formaldehyde are the desired products of acid-catalysis, the photolysis of **18** in non-buffered media was also found to be complicated by background thermal hydrolysis of the acetal initiated by photolysis. This process is presumed to be caused by the generation of catalytic amounts of permanent acid as a result of photolysis of **18**. In buffered media, this background reaction disappears, but the photolysis is also slower and does not yield the correct products. Compound **19** was designed to favor the formation of a more stable oxocarbenium ion intermediate. However, it was found to be thermally unstable in D₂O, cleanly generating ethanol, acetaldehyde, and 1,8-dihydroxynaphthalene in the absence of light.

Photolysis of **20** or **21** in methanol-d₄ results initially in rapid isomerization of the vinyl ether, generating an equilibrium mixture of the two isomers in under two minutes. Upon further photolysis, the mixture decomposes to a complex mixture of products that were unable to be characterized. When the photolysis is carried out in benzene-d₆ or acetonitrile-d₃, the reaction is much cleaner and **22** and **23** are isolated as major photoproducts (Scheme 7). A thermal background reaction was not observed in this system, as it was for **18**, suggesting that generation of these products is a direct result of photolysis.



Scheme 7. Photolysis of vinyl ethers **20** and **21** in degassed aprotic solvent.

Discussion

The hydrolysis of acetals and vinyl ethers has been heavily studied and is generally understood to display general-acid catalyzed behavior under certain conditions²⁸. The compounds studied here possess either an acetal (**18**, **19**) or a vinyl ether (**20**, **21**), and are expected to also participate in this type of mechanism, with the naphthol hydroxyl group acting as the general acid. For the acetals, this assertion is supported by previous reports on the hydrolysis of **18**³⁰. A pH-rate profile revealed a linear region at low pH (< 4), which was attributed to specific-acid catalysis by H_3O^+ , and a pH independent region between pH 4 and 10, attributed to general-acid catalysis by the naphthol. The reported mechanism for the general-acid catalyzed process is shown in Figure 8A.

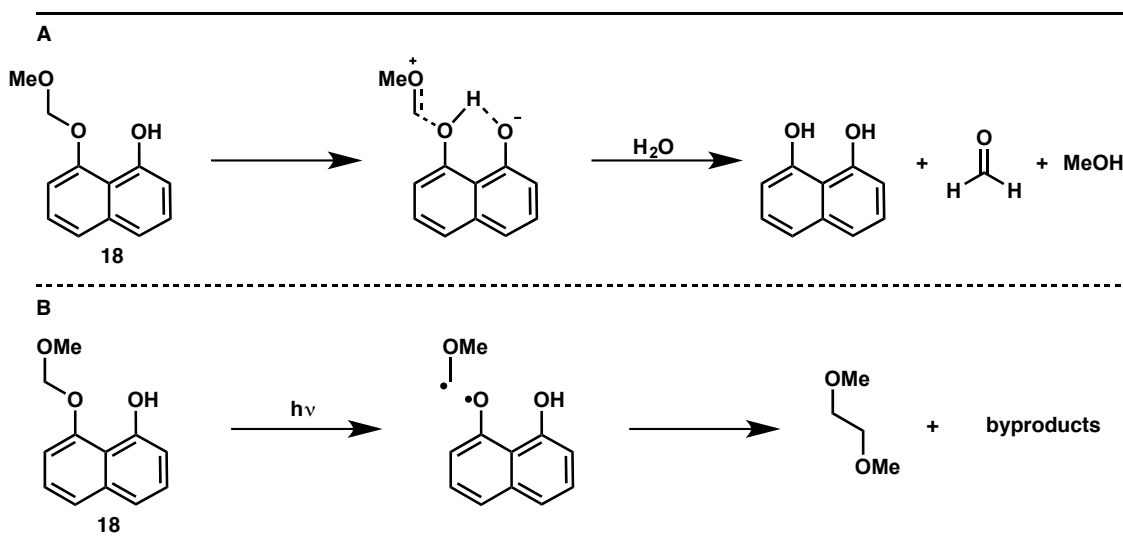


Figure 8. A) Reported general-acid catalyzed mechanism for the hydrolysis of **18**. B) Radical process that leads to the observed photolysis product, 1,2-dimethoxyethane.

Proton-transfer from the naphthol to the acetal oxygen results in formation of an oxocarbenium ion, which is trapped by water to generate 1,8-dihydroxynaphthalene, formaldehyde, and methanol. That general-acid catalysis is due to the naphthol is supported by the fact that the methoxy derivative of **18**, lacking the necessary $-\text{OH}$, did not display a pH independent region of the pH-rate profile. Under neutral conditions, where general-acid catalysis dominates the hydrolysis of **18**, the rate constant is expected to be sensitive to the pK_a of the naphthol, according to the Brønsted equation (Eq. 3). Since excitation of

naphthols typically results in an increase in acidity by ~ 8 pK_a units, the rate constant for proton-transfer is expected to increase by $\sim 10^8$ for $\alpha = 1$, or less for $\alpha < 1$. Since the reported ground-state rate constant is $\sim 10^{-4} \text{ s}^{-1}$, the excited-state rate constant is expected to be $\sim 10^4 \text{ s}^{-1}$. Comparison of this value with known rates of excited-state deactivation for 1-naphthol, either neutral ($\sim 10^9 \text{ s}^{-1}$) or deprotonated ($\sim 10^8 \text{ s}^{-1}$)¹⁴, reveals that quantum efficiencies for the excited-state process are unlikely to be greater than 10^{-4} .

Photolysis of **18** primarily generates a complex mixture of products believed to be caused by radical, not photoacid, processes, as shown in Figure 8B. This conclusion is supported by the efficient generation of 1,2-dimethoxyethane, which was formed as a major product when **18** was photolyzed under a wide variety of conditions. Although products resulting from the formation of a naphthosemiquinone were not fully characterized, mass analysis of the crude mixture suggested that homocoupling of this species also occurs to an appreciable extent. Formation of these radical-derived products is consistent with an inefficient excited-state proton transfer photoreaction, as predicted in the analysis above.

The photolysis of **20** and **21** generate the expected product of excited-state proton transfer, **22** (Scheme 7). Although the thermal process has not been studied for this particular system, an analogous system with benzoic acid as an intramolecular general-acid has been shown to proceed to the analogous product (Figure 9A)³¹. The rate constant for the process was reported to be $2 \times 10^{-3} \text{ s}^{-1}$ for the E-isomer and $2 \times 10^{-2} \text{ s}^{-1}$ for the Z-isomer, which are 10 and 100 times faster than the rate constant for the analogous reaction of **18**. If it is assumed that excitation of **20** and **21** results in a drop in the naphthol pK_a by 8 units, then excited-state proton-transfer is expected to occur with a rate constant of $2 \times 10^5 \text{ s}^{-1}$ and $2 \times 10^6 \text{ s}^{-1}$, respectively. The same analysis as that used for the photolysis of **18** predicts quantum efficiencies of 0.1 – 1%. That a major product is obtained from the photolysis of **20** and **21** that is consistent with an excited-state proton transfer mechanism perhaps reflects the greater efficiency of this reaction relative to that of **18** (Figure 9B). However, given that **18** seems to react via homolytic cleavage of the acetal C-O bond, the absence of such a reactive pathway for **20** and **21** would also allow the product **22** to be formed with greater chemical yield, regardless of the actual quantum yield. Additionally, alternant mechanisms can be

envisioned for the generation of **22**, and support for an excited-state proton-transfer pathway would require more mechanistic investigation.

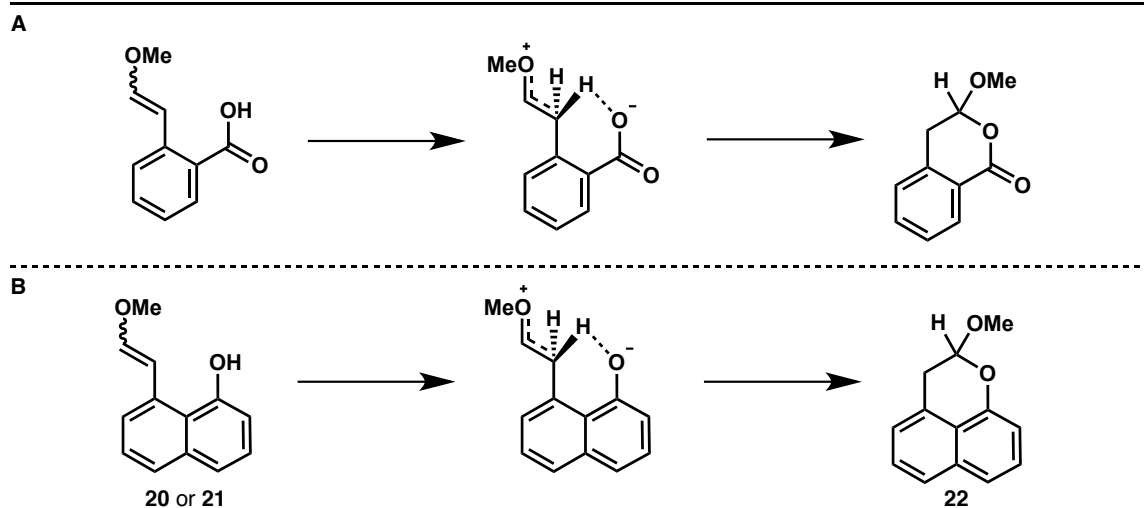


Figure 9. A) Reported intramolecular general-acid catalysis for a benzoic acid analog of **20/21**. B) Analogous photoacid mechanism for **20** and **21** that leads to the observed product **22**.

4. BIMOLECULAR SYSTEMS

4.1 Introduction

In Part 2 of this investigation, photoacid system **1** was designed to participate in an intramolecular excited state proton-transfer to a tethered t-butyl ester. That proton transfer occurs was evidenced by a large Stokes shift in the emission at 650 nm when the compound was irradiated in the longest-wavelength absorption band at 355 nm. A model was then put forth in Part 3 that describes the chemical processes that allow excited-state acids to be used to catalyze a photochemical transformation (Scheme 6). Photolysis of the resulting intramolecular systems **20** and **21** were found to generate the expected products of an excited-state proton transfer process. The current investigation seeks to apply these concepts toward the development of bimolecular photoreactions of excited-state acids.

An effective bimolecular photoreaction requires the substrate to be present in high enough concentration to undergo diffusional proton transfer during the lifetime of the excited-state acid. The intramolecular systems undergo efficient proton transfer because of

the high *effective* concentration of substrate that is afforded through tethering. The efficiency of bimolecular quenching can be monitored using fluorescence. Substrates that undergo protonation by the excited state acid are expected to result in fluorescence quenching with a concentration dependence that is reflected by the Stern-Volmer Equation (Eq. 4):

$$\frac{F_0}{F} = 1 + K_{SV}[Q] \quad (4)$$

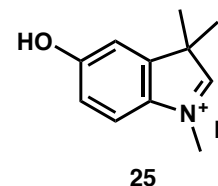
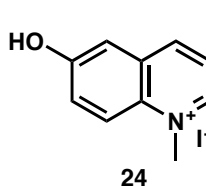
The Stern-Volmer quenching constant, K_{SV} , permits calculation of the quantum-yield for quenching (Φ_Q) at a given concentration of quencher ($[Q]$) according to Eq. 5. For a photochemical reaction that is initiated by excited-state proton transfer, Φ_Q represents the maximum efficiency for this step. If quenching processes occur that are not due to proton transfer, the quantum efficiency will be lower than Φ_Q . For a general-acid catalyzed process that conforms to the model in Scheme 6, the efficiency of proton transfer represents the efficiency of the photoreaction. Substrates that undergo general-acid catalyzed processes and display efficient Stern-Volmer quenching are therefore ideal candidates for the discovery of new photoreactions of excited-state acids:

$$\Phi_Q = \frac{[Q]}{[Q] + 1/K_{SV}} \quad (5)$$

4.2 Results & Discussion

The naphthols were initially screened for fluorescence quenching by a wide range of substrates that participate in general-acid catalysis, such as acetals, orthoesters, and vinyl ethers. However, no substrates were identified that led to noticeable quenching of the naphthol fluorescence, suggesting that efficient excited-state proton transfer reactions cannot be accessed in a bimolecular fashion for these short-lived and weak photoacids.

The hydroxyquinolinium **24** has been previously reported to have an excited-state pK_a of -7. Shown in Figure 10A is the fluorescence quenching of **24** by water in



acetonitrile upon excitation at 355 nm. That the absorbance spectrum undergoes only minimal change at these concentrations of quencher suggest that the quenching process is diffusional (data not shown). A Stern-Volmer constant, K_{SV} , of 22 M^{-1} is obtained through linear regression analysis of the maximum fluorescence intensity (Figure 10A). In contrast,

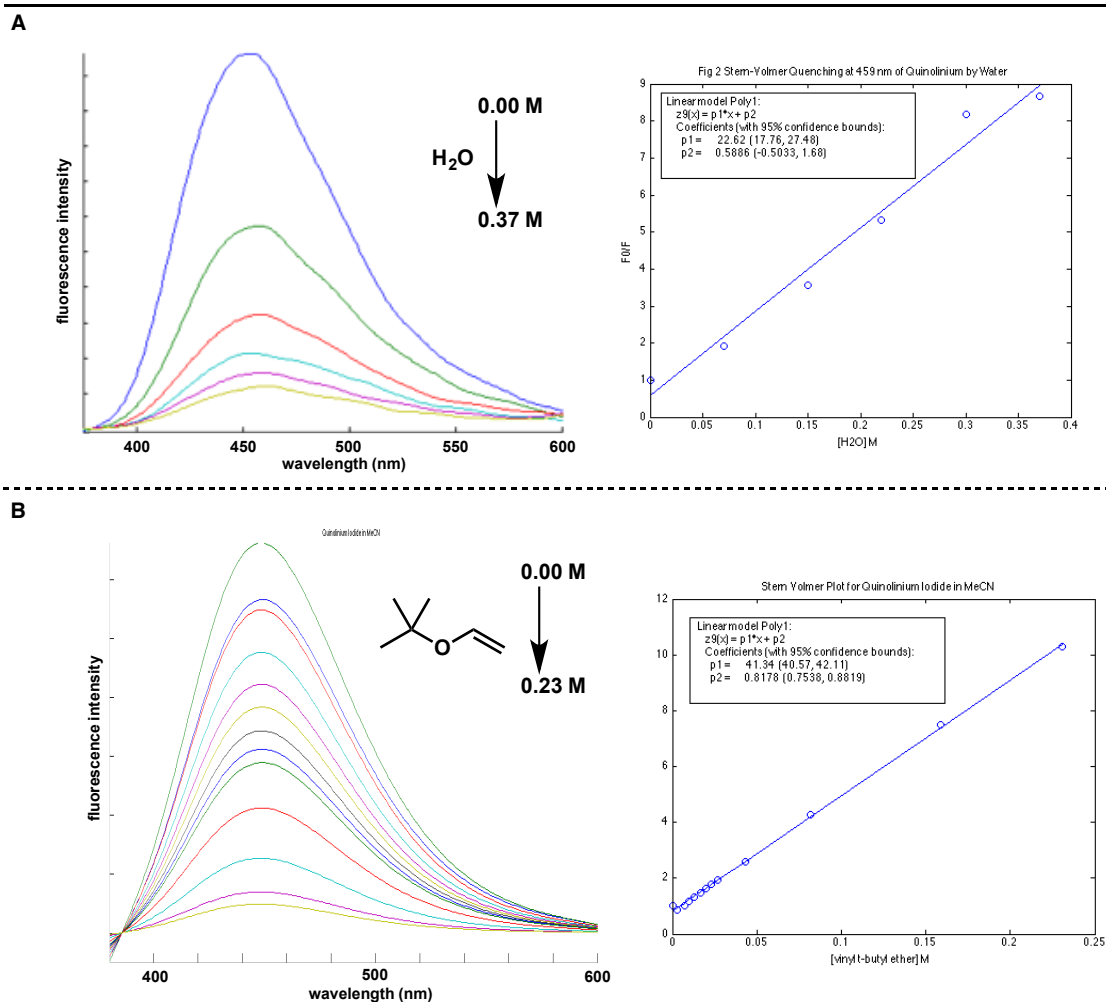
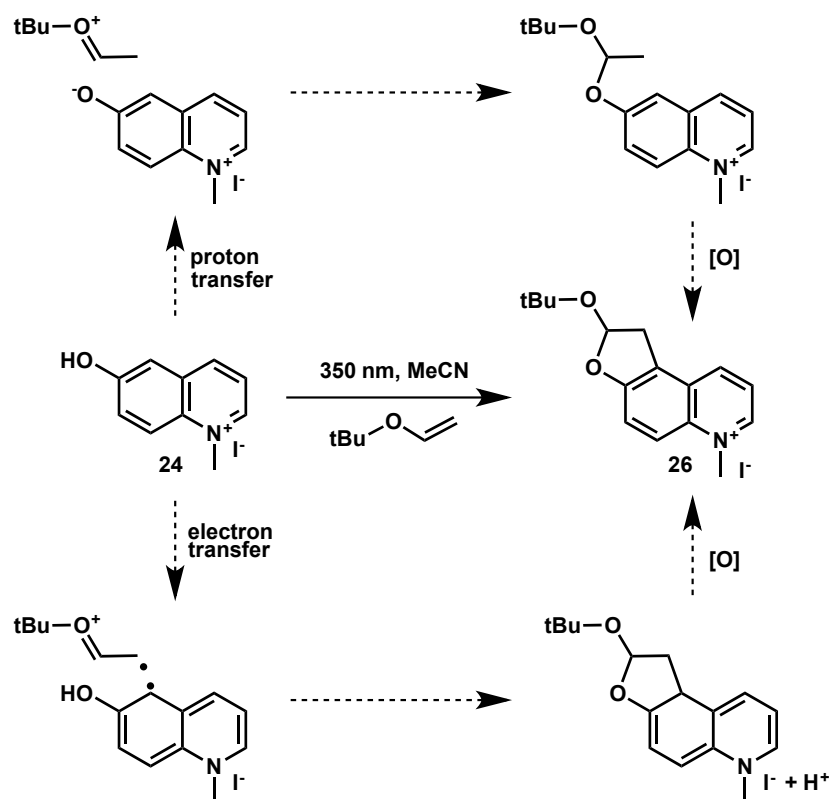


Figure 10. Stern-Volmer quenching of fluorescence from **24** in acetonitrile by **A)** water and **B)** t-butyl vinyl ether. Shown are emission spectra with increasing concentrations of quencher and Stern-Volmer plots with linear fits.

the hydroxyindolinium **25** displays a modest fluorescence enhancement with a K_{SV} value of -0.6 M^{-1} upon addition of water in acetonitrile. However, larger differences in the absorbance spectrum suggest that this enhancement could be due to a static process, such as complex formation between **25** and water. These results support previous findings that **24** is an excited-state acid capable of protonating water, while **25** is incapable of doing so, either because it is not an excited-state acid or because the excited state is too short-lived to undergo efficient bimolecular proton transfer at these concentrations of quencher.

Efficient fluorescence quenching of **24** was also observed in the presence of t-butyl vinyl ether, a substance known to undergo general-acid catalyzed hydrolysis. The emission spectra and Stern-Volmer plot are shown in Figure 10B, and a K_{SV} value of 41 M^{-1} was obtained. Since this vinyl ether displayed the most potent quenching for **24** of the various compounds that were tested, it was further explored as a potential photochemical reaction partner. Specifically, when **24** is photolyzed at approximately 350 nm in degassed acetonitrile containing t-butyl vinyl ether, the cyclic acetal **26** is obtained as a major product (Scheme 8). If this product were the result of an excited-state proton-transfer process, a secondary oxidation step would have to be invoked. It seems more likely that this product results from a photoinduced electron transfer process, where a vinyl ether radical cation can form the requisite C-O and C-C bonds directly, and oxidation to the quinolinium can take place through disproportionation. Similar processes have been reported for other systems³².



Scheme 8. Photoreaction of **24** in degassed acetonitrile in the presence of t-butyl vinyl ether. Either an initial proton-transfer or electron-transfer could generate the observed product, **26**.

5. CONCLUSIONS

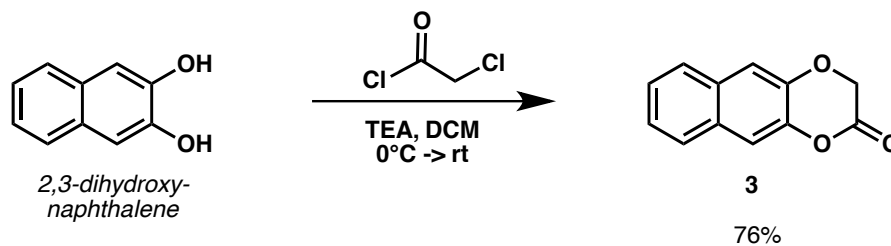
Development of photochemical reactions that harness excited-state acidity is a challenging task primarily due to the competing kinetics between excited-state deactivation and acid-catalyzed reaction. In the course of these investigations, a kinetic model was developed that led to the hypothesis that specialized intramolecular general-acid catalyzed systems would be capable of undergoing efficient photoreaction through an ESIPT mechanism. One of these systems is the vinyl ether **25**, which contains a 1-naphthol photoacid. Photolysis of this compound results in generation of the expected product of an ESIPT pathway.

6. EXPERIMENTAL

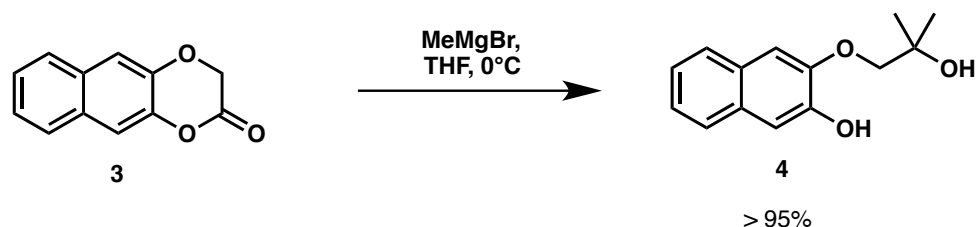
6.1 *Materials and Methods*

Unless otherwise stated, reactions were performed under an argon atmosphere using freshly dried solvents. N,N-dimethylformamide, methanol, dichloromethane, and tetrahydrofuran were dried by passing through activated alumina. Triethylamine and diisopropylamine, and pyridine were distilled from CaH₂ under an argon atmosphere. All other commercially obtained reagents were used as received unless specifically indicated. All reactions were monitored by thin-layer chromatography using EMD/Merck silica gel 60 F254 pre-coated plates (0.25 mm). Protection of certain materials from light was accomplished by wrapping the reaction, workup, and chromatography glassware with foil or working in conditions of low-ambient light. Unless otherwise stated, irradiations at 350 nm were carried out using collimated light from a 500 W high-pressure mercury vapor lamp (Oriol 66011 lamp housing and 6285 bulb) passed through water-cooled Schott WG335/UG11 filters. Visible light irradiations were carried out using a Luzchem irradiation chamber equipped with eight cool white fluorescent tubes (LCZ-VIS) and with magnetic stirring.

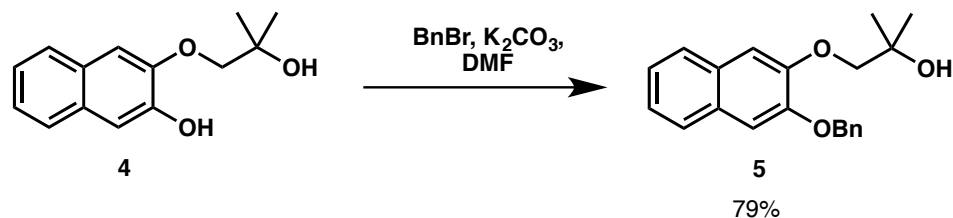
6.2 Preparative Procedures and Spectroscopic Data



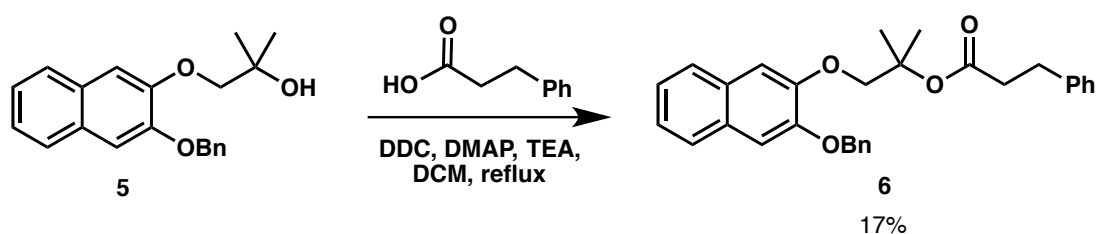
2H,3H-naphtho[2,3-b][1,4]dioxin-2-one (3). To an oven-dried 500 mL round bottom flask equipped with a magnetic stir bar and a reflux condenser is added 2,3-dihydroxynaphthalene (5 g, 1 eq) and dry DCM (150 mL). Freshly distilled triethylamine (2.2 eq) is added dropwise, and the mixture is cooled with an ice-water bath. Chloroacetyl chloride (1.1 eq) is added dropwise, and the reaction is stirred 30 minutes, allowed to warm to room temperature, then refluxed 4 hours. After cooling to room temperature, the reaction is quenched with water (200 mL) and extracted with DCM (150 mL x 3), dried over MgSO_4 , flushed through a plug of silica gel, and concentrated *in vacuo* to yield **3** which was used without further purification. $^1\text{H NMR}$ (300 MHz, Chloroform-*d*) δ 7.86 – 7.68 (m, 2H), 7.54 (s, 1H), 7.50 – 7.38 (m, 3H), 4.77 (s, 2H).



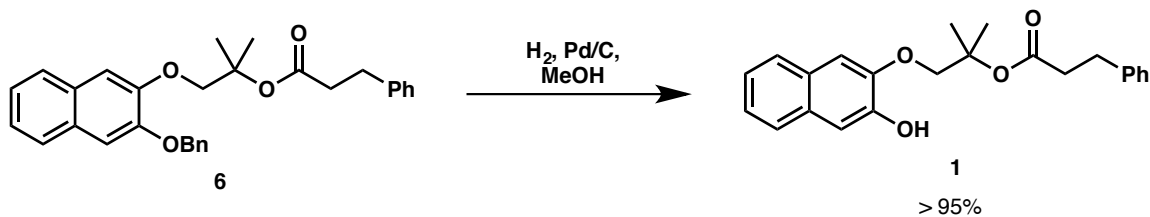
3-(2-hydroxy-2-methylpropoxy)naphthalen-2-ol (4). To an oven-dried 150 mL round bottom flask equipped with a magnetic stir bar and under an argon atmosphere is added lactone **3** (1 eq, 1.5 g) and dry THF (75 mL). The solution is cooled with an ice-water bath, then methyl magnesium bromide (2.2 eq, 3 M in Et_2O) is added dropwise. The reaction is allowed to warm to room temperature and stirred for 2 hours, then quenched with sat. aq. NH_4Cl (100 mL) and extracted with Et_2O (100 mL x 3), dried over MgSO_4 , and concentrated *in vacuo* to yield **4** as a white solid which was used without further purification. $^1\text{H NMR}$ (300 MHz, Chloroform-*d*) δ 7.65 (ddd, $J = 7.5, 6.3, 2.3$ Hz, 2H), 7.36 – 7.27 (m, 3H), 7.13 (s, 1H), 6.87 (s, 1H), 4.00 (s, 2H), 2.55 (s, 1H), 1.44 (s, 6H).



1-{{3-(benzyloxy)naphthalen-2-yl}oxy}-2-methylpropan-2-ol (5). To a round bottom flask equipped with a magnetic stir bar is added diol **5** (1 eq, 350 mg), dry DMF (15 mL), benzyl bromide (2.2 eq), and K_2CO_3 (5 eq). The reaction is stirred at room temperature overnight, then diluted in water (250 mL) and extracted with diethyl ether (100 mL x 3). The combined organics are dried over MgSO_4 , and concentrated *in vacuo*. The crude material is purified by flash column chromatography (SiO_2 , 25% EtOAc in hexanes) to yield **5** as a clear oil. ^1H NMR (400 MHz, Chloroform-*d*) δ 7.65 (m, 2H), 7.49 (d, $J = 7.6$ Hz, 2H), 7.43 – 7.28 (m, 5H), 7.19 (m, 2H), 5.21 (s, 2H), 3.95 (s, 2H), 1.37 (s, 6H).

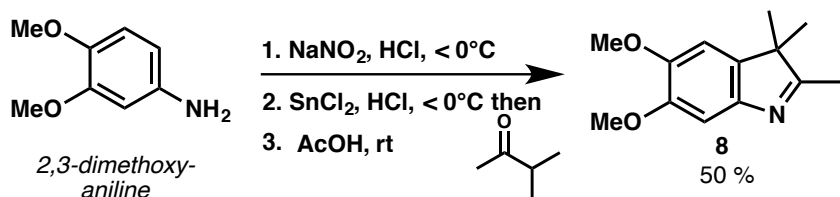


1-{{3-(benzyloxy)naphthalen-2-yl}oxy}-2-methylpropan-2-yl-3-phenylpropanoate (6). To a 25 mL round bottom flask equipped with a magnetic stir bar and reflux condenser is added **5** (1 eq, 229 mg), dry DCM (10 mL), hydrocinnamic acid (5 eq), freshly distilled triethylamine (5 eq), DMAP (0.25 eq), and DCC (5 eq). The reaction is heated to reflux overnight, then diluted with water (25 mL), and extracted with DCM (25 mL x 3). The combined organics are washed with 1 M HCl, 1M NaOH, then dried over MgSO_4 , and concentrated *in vacuo*. The crude is purified by flash column chromatography (SiO_2 , 5 - 10% EtOAc in hexanes) to yield **6** as a clear oil. ^1H NMR (400 MHz, Chloroform-*d*) δ 7.59 (m, 2H), 7.43 (d, $J = 7.5$ Hz, 2H), 7.33 – 7.01 (m, 12H), 5.13 (s, 2H), 4.18 (s, 2H), 2.79 (t, $J = 7.8$ Hz, 2H), 2.46 (t, $J = 7.9$ Hz, 2H), 1.47 (s, 6H).



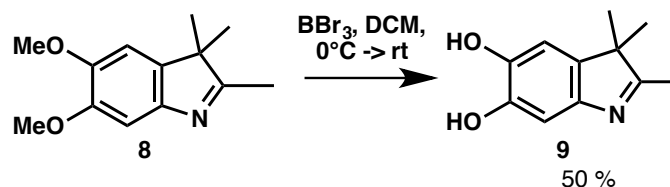
1-[(3-hydroxynaphthalen-2-yl)oxy]-2-methylpropan-2-yl 3-phenylpropanoate (1).

Benzyl ether **1** (1 eq, 57 mg) is dissolved in methanol (10 mL). Pd/C (20 mg) is added and the flask is purged-backfilled thrice with argon, then with H₂. After vigorous stirring for 7 hours under an atmosphere of H₂, the crude is passed through a plug of celite, washed with ethanol, and concentrated *in vacuo*. The crude was purified by flash column chromatography (SiO₂, 25% EtOAc in hexanes) to yield **1** as a clear oil. ¹H NMR (400 MHz, Chloroform-*d*) δ 7.64 – 7.58 (m, 2H), 7.31 – 7.05 (m, 9H), 4.20 (s, 2H), 2.89 – 2.82 (t, *J* = 7.5 Hz, 2H), 2.55 (t, *J* = 7.5 Hz, 2H), 1.54 (s, 6H).

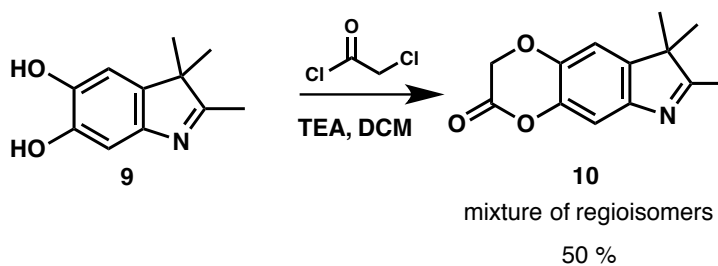


5,6-dimethoxy-2,3,3-trimethyl-3H-indole (8). In a round bottom flask with magnetic stir bar and thermometer, and immersed in a temperature-controlled bath, 3,4-dimethoxyaniline (1 eq, 1 g) is dissolved at -5°C in a mixture of water (30 mL) and concentrated HCl (30 mL). A chilled solution of NaNO₂ (1.1 eq) in water (10 mL) is added dropwise such that the reaction does not exceed 0°C. The reaction is stirred 30 minutes, then a chilled solution of SnCl₂ (3 eq) in HCl (5 mL) is added dropwise such that the reaction does not exceed 0°C. Immediately after addition is complete, 3-methyl-2-butanone (3 eq) is added and reaction is warmed to room temperature, quenched into sat. aq. NaHCO₃, extracted EtOAc (100 mL x 3), dried over MgSO₄, and concentrated *in vacuo*. The residue is taken up in acetic acid (60 mL) and additional 3-methyl-2-butanone is added (3 eq). The mixture is stirred at room temperature overnight, then concentrated *in vacuo*. The residue is purified by flash column chromatography (SiO₂, 75% EtOAc in hexanes) to yield **8** as a clear oil. ¹H NMR (300 MHz, Chloroform-*d*) δ 7.15 (s, 1H), 6.81 (s, 1H), 3.90

(s, 6H), 2.24 (s, 3H), 1.27 (s, 6H). ESI-MS(+) calculated for $[\text{C}_{13}\text{H}_{18}\text{NO}_2]^+$ ($[\text{M}+\text{H}]^+$) 220.1, found 220.1.

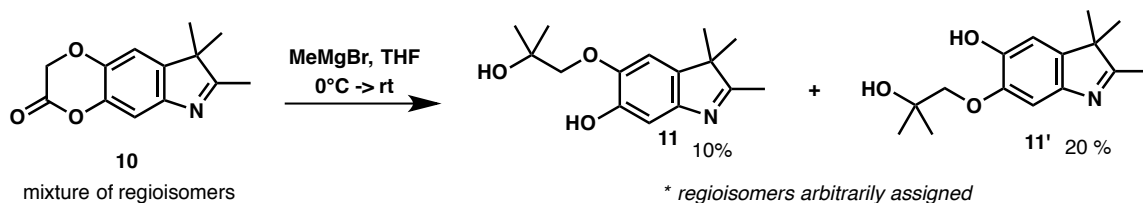


2,3,3-trimethyl-3H-indole-5,6-diol (9). To an oven-dried 100 mL round bottom flask equipped with a magnetic stir bar and under an argon atmosphere is added **8** (1 eq, 920 mg), and dry DCM (40 mL). The solution is cooled to 0°C, and BBr_3 (3 eq) is added dropwise. The reaction is stirred for 2 hours at room temperature, and then quenched with 1M sodium acetate (50 mL), extracted with DCM (50 mL x 3), dried over MgSO_4 , and concentrated *in vacuo*. The residue is purified by flash column chromatography (SiO_2 , 5% methanol in DCM) to yield **9** as a brown solid. ^1H NMR (300 MHz, Acetone- d_6) δ 7.00 (s, 1H), 6.86 (s, 1H), 3.33 (s, 1H), 2.18 (s, 3H), 1.96 (s, 1H), 1.23 (s, 6H). ESI-MS(+) calculated for $[\text{C}_{11}\text{H}_{14}\text{NO}_2]^+$ ($[\text{M}+\text{H}]^+$) 192.1, found 192.1.



7,8,8-trimethyl-2H,3H,8H-[1,4]dioxino[2,3-f]indol-3-one + **7,8,8-trimethyl-2H,3H,8H-[1,4]dioxino[2,3-f]indol-2-one (10)**. To an oven-dried schlenk flask equipped with a magnetic stirbar is added diol **9** (1 eq, 188 mg) and dry DCM (10 mL). The solution is freeze-pump-thawed three times, backfilling with argon. Then, at 0°C, freshly distilled triethylamine (2.2 eq) is added dropwise, followed by chloroacetylchloride (1.1 eq) dropwise. The mixture is stirred at 0°C for 1 hour, then heated in a 60°C oil-bath overnight. After cooling, the reaction is diluted in sat. aq. NH_4Cl (10 mL) and extracted with EtOAc (10 mL x 3). The combined organics are dried over MgSO_4 , and concentrated *in vacuo* to

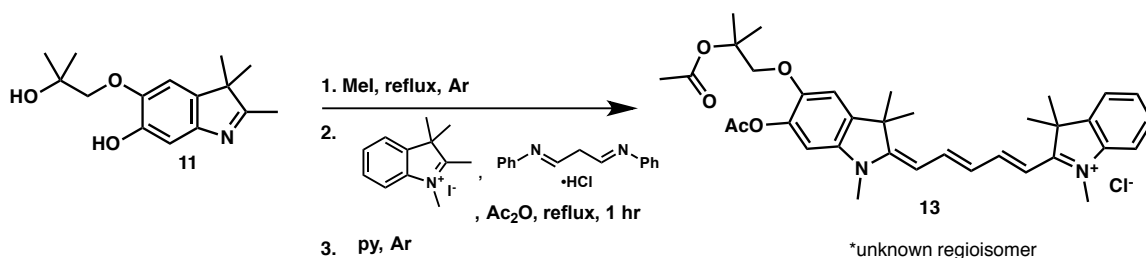
provide **10** as a 3:2 mixture of regioisomers. $^1\text{H NMR}$ (400 MHz, Chloroform-*d*) δ 7.25 – 7.19 (s, 1H), 6.98 – 6.93 (s, 1H), 4.65 (s, 2H), 2.24 (s, 3H), 1.27 (s, 6H). ESI-MS(+) calculated for $[\text{C}_{13}\text{H}_{14}\text{NO}_3]^+$ ($[\text{M}+\text{H}]^+$) 232.1, found 232.0.



5-(2-hydroxy-2-methylpropoxy)-2,3,3-trimethyl-3H-indol-6-ol + 6-(2-hydroxy-2-methylpropoxy)-2,3,3-trimethyl-3H-indol-5-ol (11** + **11'**).**

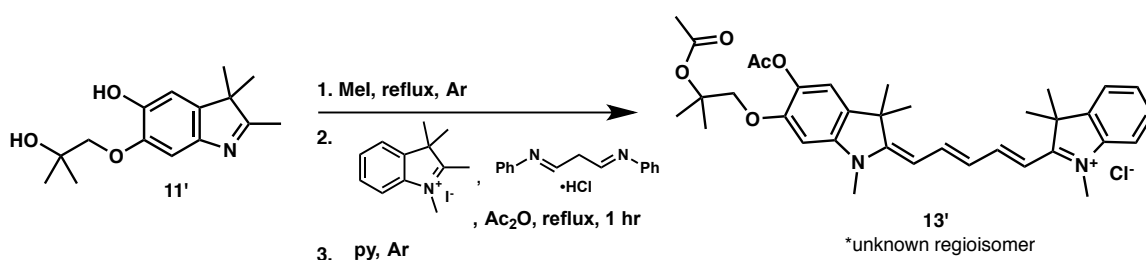
To an oven-dried round bottom flask under an argon atmosphere is added the mixture of isomers **10** (1 eq, 84 mg) and dry tetrahydrofuran (3 mL). The solution is cooled with a dry-ice acetone bath, and methyl magnesium bromide (2.1 eq, 3 M in diethyl ether) is added dropwise. The solution is warmed to room temperature and stirred for 30 minutes, then quenched with sat. aq. NH_4Cl (5 mL), extracted with EtOAc (5 mL x 3), dried over MgSO_4 , and concentrated *in vacuo*. The crude material is purified by flash column chromatography (SiO_2 , 5% methanol in DCM + 1% AcOH) to yield **11** and **11'** as slightly red oils. Data for **11**: $^1\text{H NMR}$ (300 MHz, Chloroform-*d*) δ 7.18 (s, 1H), 6.77 (s, 1H), 3.86 (s, 2H), 2.24 (s, 3H), 1.38 (s, 6H), 1.24 (s, 6H). ESI-MS(+) calculated for $[\text{C}_{15}\text{H}_{22}\text{NO}_3]^+$ ($[\text{M}+\text{H}]^+$) 264.1, found 264.1.

Data for **11'**: $^1\text{H NMR}$ (300 MHz, Chloroform-*d*) δ 7.13 (s, 1H), 6.87 (s, 1H), 3.87 (s, 2H), 2.24 (s, 3H), 1.37 (s, 6H), 1.25 (s, 6H). ESI-MS(+) calculated for $[\text{C}_{15}\text{H}_{22}\text{NO}_3]^+$ ($[\text{M}+\text{H}]^+$) 264.1, found 264.1.



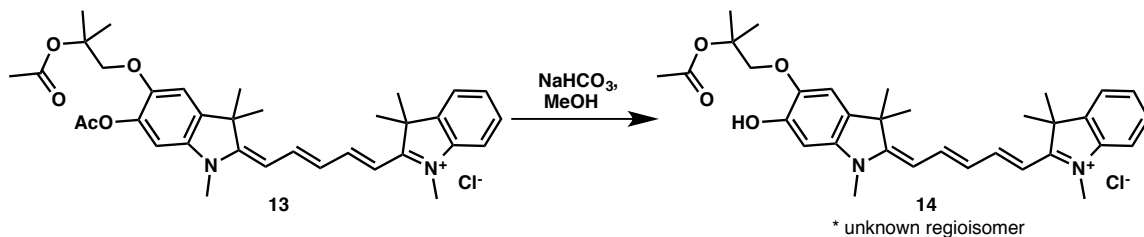
2-[(1E,3E)-5-[(2E)-6-(acetyloxy)-5-[2-(acetyloxy)-2-methylpropoxy]-1,3,3-trimethyl-2,3-dihydro-1H-indol-2-ylidene]penta-1,3-dien-1-yl]-1,3,3-trimethyl-3H-indol-1-ium

chloride (13). This procedure is carried out with protection from light, as described above. To an oven-dried Schlenk flask, equipped with a magnetic stir bar and under an argon atmosphere, was added **11** (18 mg) followed by methyl iodide (2 mL). The flask is sealed and heated to 40°C using an oil-bath for 2 hours, then cooled to room temperature, and concentrated *in vacuo* to yield the indolinium iodide as a white precipitate. In a separate schlenk flask, 1,2,3,3-tetramethylindolinium iodide (1.1 eq) and malondialdehyde bis(phenylimine)•HCl (1.1 eq) are heated at 100°C in acetic anhydride (750 µL) under a closed argon atmosphere for 2 hours, then cooled to room temperature, and cannulated into the Schlenk containing the indolinium iodide derived from **11**. Freshly distilled pyridine (750 µL) is added dropwise and the mixture is stirred under a closed argon atmosphere overnight. The solution is then quenched with 1M sodium acetate (5 mL), and extracted with EtOAc (5 mL x 3). The combined organics are washed with brine, dried over MgSO₄, and concentrated *in vacuo*. The crude material is purified by reverse-phase HPLC (C18, 50% acetonitrile in water + 0.1% acetic acid) to yield **13** as a blue residue. ¹H NMR (400 MHz, Chloroform-*d*) δ 8.33 (bm, 2H), 7.48 – 7.30 (m, 2H), 7.23 – 7.14 (m, 1H), 7.07 (d, *J* = 7.9 Hz, 1H), 6.97 (s, 1H), 6.83 (s, 1H), 6.80 – 6.70 (m, 1H), 6.39 – 6.25 (m, 2H), 4.18 (s, 2H), 3.68 (s, 3H), 3.66 (s, 3H), 2.33 (s, 3H), 2.00 (s, 3H), 1.74 (s, 12H), 1.55 (s, 6H). ESI-MS(+) calculated for [C₃₅H₄₃N₂O₅]⁺ ([M]⁺) 571.3, found 571.3.

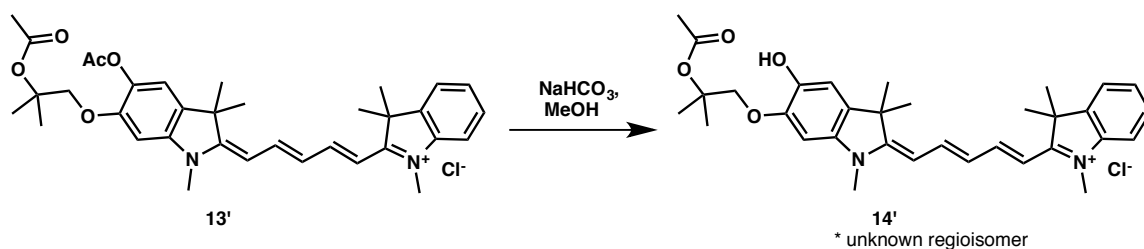


2-[(1E,3E)-5-[(2E)-5-(acetyloxy)-6-[2-(acetyloxy)-2-methylpropoxy]-1,3,3-trimethyl-2,3-dihydro-1H-indol-2-ylidene]penta-1,3-dien-1-yl]-1,3,3-trimethyl-3H-indol-1-ium chloride (13'). Using the same procedure as that for **13**, **13'** is isolated as a blue residue. ¹H NMR (400 MHz, Chloroform-*d*) δ 8.26 (bm, 2H), 7.37 – 7.34 (m, 2H), 7.22 (m, 1H), 7.10 (m, 1H), 7.01 (s, 1H), 6.74 (s, 1H), 6.80 – 6.74 (m, 1H), 6.37 – 6.29 (m, 2H), 4.23 (s, 2H),

3.71 (s, 3H), 3.69 (s, 3H), 2.31 (s, 3H), 2.01 (s, 3H), 1.73 (s, 12H), 1.55 (s, 6H). ESI-MS(+) calculated for $[\text{C}_{35}\text{H}_{43}\text{N}_2\text{O}_5]^+$ ($[\text{M}]^+$) 571.3, found 571.3.

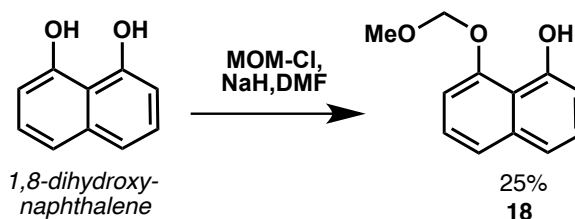


2-[(1E,3E)-5-[(2E)-5-[2-(acetyloxy)-2-methylpropoxy]-6-hydroxy-1,3,3-trimethyl-2,3-dihydro-1H-indol-2-ylidene]penta-1,3-dien-1-yl]-1,3,3-trimethyl-3H-indol-1-ium chloride (14). In a 2 mL vial with magnetic stir bar and in darkness, **13** is treated with 1M sodium bicarbonate (500 μL) and methanol (500 μL). The solution is stirred 10 minutes, then quenched with 1M sodium acetate buffered at pH = 7 (5 mL). The aqueous is extracted with DCM (5 mL x 3), washed with brine, dried over MgSO_4 , and concentrated *in vacuo*. The crude material is purified by reverse-phase HPLC (C18, 5-95% acetonitrile in water + 0.1% acetic acid) to obtain **14** as a blue residue. ^1H NMR (500 MHz, Chloroform-*d*) δ 7.88 (br m, 2H), 7.18 (s, 1H), 7.15 (t, $J = 7.4$ Hz, 1H), 6.97 (d, $J = 7.8$ Hz, 1H), 6.92 (s, 1H), 6.55 (t, $J = 12.6$ Hz, 1H), 6.31 (d, $J = 14.1$ Hz, 1H), 5.96 (d, $J = 13.0$ Hz, 1H), 4.29 (s, 2H), 3.77 (s, 3H), 2.02 (s, 3H), 2.01 (s, 3H), 1.70 (s, 6H), 1.65 (s, 6H), 1.61 (s, 6H). ESI-MS(+) calculated for $[\text{C}_{33}\text{H}_{41}\text{N}_2\text{O}_4]^+$ ($[\text{M}]^+$) 529.3, found 529.3.

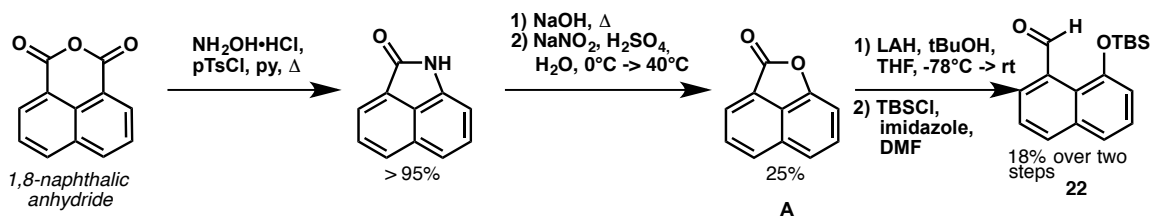


2-[(1E,3E)-5-[(2E)-6-[2-(acetyloxy)-2-methylpropoxy]-5-hydroxy-1,3,3-trimethyl-2,3-dihydro-1H-indol-2-ylidene]penta-1,3-dien-1-yl]-1,3,3-trimethyl-3H-indol-1-ium chloride (14'). Using the same procedure as that for **14**, **14'** is isolated as a blue residue. ^1H NMR (500 MHz, Chloroform-*d*) δ 7.88 – 7.70 (m, 2H), 7.39 – 7.28 (m, 2H), 7.15 (t, $J =$

7.5 Hz, 1H), 6.97 (d, $J = 7.9$ Hz, 1H), 6.87 (s, 1H), 6.46 (t, $J = 12.5$ Hz, 1H), 6.18 (d, $J = 14.2$ Hz, 1H), 5.89 (d, $J = 13.1$ Hz, 1H), 4.23 (s, 2H), 3.71 (s, 3H), 2.09 (s, 3H), 2.00 (s, 3H), 1.69 (s, 6H), 1.64 (s, 6H), 1.59 (s, 6H). ESI-MS(+) calculated for $[\text{C}_{33}\text{H}_{41}\text{N}_2\text{O}_4]^+$ ($[\text{M}]^+$) 529.3, found 529.3.



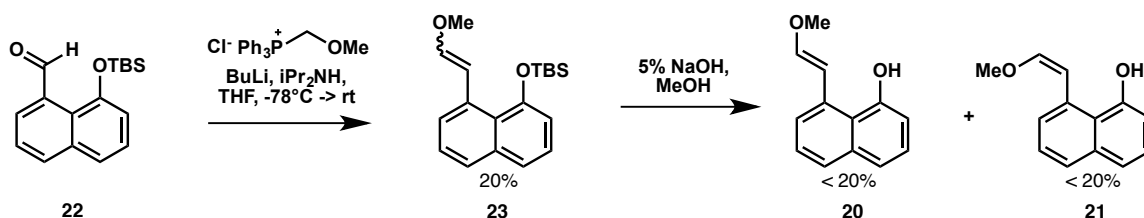
8-(methoxymethoxy)naphthalen-1-ol (18). 1,8-dihydroxynaphthalene (100 mg, 1 eq) in dry DMF (500 μL) is added to a suspension of sodium hydride (1.25 eq, 60% dispersion) in DMF (1 mL). After 30 minutes, MOM-Cl is added dropwise and the reaction is stirred at room temperature for 1 hour. The solution is then quenched with 1M NaOAc (pH = 7), and extracted with diethyl ether. The combined organics are dried over MgSO_4 , and concentrated *in vacuo*. The crude is purified by flash column chromatography (SiO_2 , 10% EtOAc in hexanes) to yield **18** as a clear oil. ^1H NMR (300 MHz, Chloroform- d) δ 9.31 (s, 1H), 7.47 (d, $J = 8.3$ Hz, 1H), 7.41 – 7.25 (m, 3H), 7.05 (d, $J = 7.7$ Hz, 1H), 6.90 (dd, $J = 7.1, 1.7$ Hz, 1H), 5.44 (s, 2H), 3.59 (s, 3H). ESI-MS(–) calculated for $[\text{C}_{12}\text{H}_{11}\text{O}_3]^-$ ($[\text{M}-\text{H}]^-$) 203.0, found 203.1.



8-[(tert-butyldimethylsilyl)oxy]naphthalene-1-carbaldehyde (22). **A** is initially synthesized from 1,8-naphthalic anhydride according to *J. Org. Chem.*, **2002**, 67 (21), 7457. Then, in an oven-dried round bottom flask under an argon atmosphere is added lithium aluminum hydride (1 eq, 6 mL, 1M in THF) and dry THF (10 mL). Freshly distilled *t*BuOH (3 eq) is added dropwise and the reaction is stirred 30 minutes at room temperature,

then added via syringe to a -78°C solution of **A** (1 eq) in dry THF (10 mL). The solution is stirred at room temperature overnight, then quenched with 1M HCl (25 mL) and extracted with diethyl ether (25 mL x 3), the combined organics dried over MgSO_4 , and concentrated *in vacuo*. The crude material is purified by flash column chromatography (SiO_2 , 10% EtOAc in hexane) to yield 8-hydroxynaphthalene-1-carbaldehyde as a clear oil which was used without further purification.

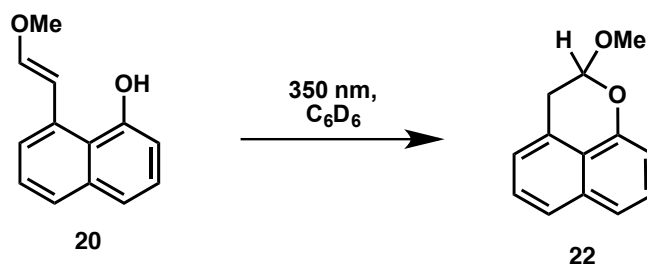
To a solution of the aldehyde (1 eq, 650 mg) in dry DMF (5 mL) is added TBSCl (2 eq) and imidazole (2 eq). The reaction is stirred for 2 hours, then diluted in water (25 mL) and extracted with diethyl ether (25 mL x 3). The combined organics are dried over MgSO_4 , and concentrated *in vacuo*. The crude is purified by flash column chromatography (SiO_2 , 10% EtOAc in hexanes) to yield **22** as a clear oil. ^1H NMR (300 MHz, Chloroform-*d*) δ 11.13 (s, 1H), 8.02 – 7.83 (m, 2H), 7.58 – 7.46 (m, 2H), 7.43 – 7.34 (m, 1H), 7.03 (d, $J = 7.6$, 0.9 Hz, 1H), 1.00 (s, 9H), 0.32 (s, 6H).



8-[(E)-2-methoxyethenyl]naphthalen-1-ol (20) and **8-[(Z)-2-methoxyethenyl]naphthalen-1-ol (21)**. To an oven-dried round bottom flask under an argon atmosphere is added n-butyllithium (2 eq, 2.1 M in THF) and dry THF (20 mL). Freshly distilled diisopropylamine (2 eq) is added dropwise, and the reaction is stirred 10 minutes, then cooled with a dry ice-acetone bath. (methoxymethyl)triphenylphosphonium chloride (2 eq) is added, and the reaction is warmed to room temperature and stirred 30 minutes, then cooled again to -78°C . **22** (1 eq) is added dropwise as a solution in dry THF, and the reaction is stirred at room temperature for 1 hour, then diluted in water (50 mL), and extracted with EtOAc (50 mL x 3). The combined organics are passed through a plug of silica gel, and concentrated *in vacuo*. The crude is purified by flash column chromatography (SiO_2 , 10% EtOAc in hexanes) to yield **23** as a mixture of isomers. ^1H NMR (600 MHz, Chloroform-*d*) δ 7.91 (d, $J = 7.4$ Hz, 0.4H), 7.63 (dd, $J = 16.2$, 7.9 Hz, 1H),

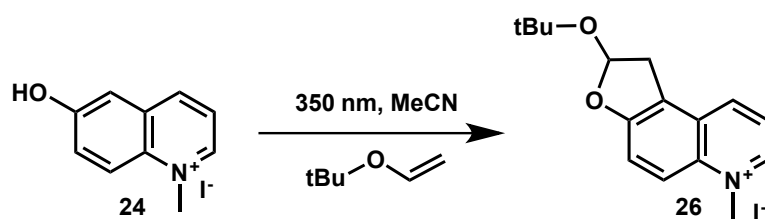
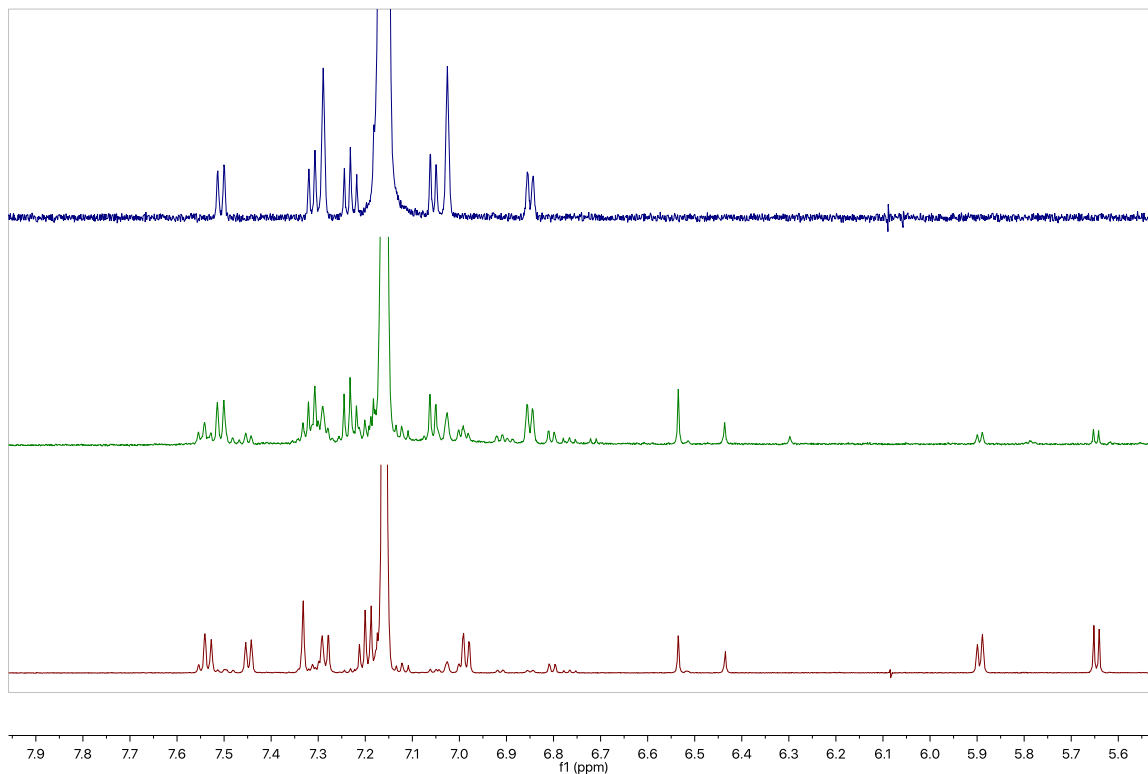
7.45 – 7.18 (m, 3.6H), 7.04 (d, $J = 12.4$ Hz, 0.6H), 6.90 – 6.80 (m, 1H), 6.64 – 6.52 (m, 1H), 6.14 (d, $J = 7.3$ Hz, 0.4H), 3.74 (s, 1.4H), 3.73 (s, 1.6H), 1.02 (s, 3.6H), 1.01 (s, 5.4H), 0.33 (s, 3.6H), 0.30 (s, 2.4H).

The mixture of isomers **23** is taken up in MeOH (1 mL), and treated with 5% sodium hydroxide in methanol (1 mL). The reaction is stirred 4 hours under an argon atmosphere, then quenched with sat. aq. NH_4Cl (5 mL) and extracted with EtOAc (5 mL x 3). The combined organics are dried over MgSO_4 , and concentrated *in vacuo*. The crude material is purified by flash column chromatography (SiO_2 , 50% DCM in hexane) to yield **20** and **21** as clear oils. Data for (**20**): ^1H NMR (600 MHz, Chloroform-*d*) δ 7.70 (d, $J = 8.3$ Hz, 1H), 7.47 (s, 1H), 7.44 – 7.28 (m, 3H), 6.90 (d, $J = 7.5$ Hz, 1H), 6.49 (d, $J = 6.6$ Hz, 1H), 6.11 (d, $J = 7.1$ Hz, 1H), 3.73 (s, 3H). ESI-MS(+) calculated for $[\text{C}_{13}\text{H}_{13}\text{O}_2]^+$ ($[\text{M}+\text{H}]^+$) 201.0, found 200.9. Data for (**21**): ^1H NMR (600 MHz, Chloroform-*d*) δ 7.71 (d, $J = 8.2$ Hz, 1H), 7.40 (d, $J = 8.2$ Hz, 1H), 7.34 (dd, $J = 7.9$ Hz, 2H), 7.17 (d, $J = 7.0$ Hz, 1H), 6.94 – 6.83 (m, 2H), 6.65 (d, $J = 12.9$ Hz, 1H), 3.78 (s, 3H). ESI-MS(+) calculated for $[\text{C}_{13}\text{H}_{13}\text{O}_2]^+$ ($[\text{M}+\text{H}]^+$) 201.0, found 200.9.



In a quartz J. Young tube, **20** is dissolved in C_6D_6 , freeze-pump-thawed thrice, and backfilled with an argon atmosphere. Photolysis was carried out using collimated light from a 500 W high-pressure mercury vapor lamp (Oriol 66011 lamp housing and 6285 bulb) and passed through water-cooled Schott WG335/UG11 filters. The reaction progress was monitored by ^1H -NMR. Shown below is the aromatic region for the sample prior to photolysis (red), after 6 minutes of irradiation (green), and the purified product **22** (blue) in C_6D_6 . The photolysis products were purified by preparative thin-layer chromatography (50% DCM in hexanes) to yield **22** as the major product. ^1H NMR (600 MHz, Chloroform-*d*) δ 7.67 (d, $J = 8.4$ Hz, 1H), 7.44 (d, $J = 8.1$ Hz, 1H), 7.41 – 7.35 (m, 2H), 7.17 (d, $J = 6.9$ Hz,

1H), 6.97 (d, $J = 7.3$ Hz, 1H), 5.39 (t, $J = 3.3$ Hz, 1H), 3.52 (s, 3H), 3.49 – 3.37 (m, 1H), 3.23 (dd, $J = 16.1, 3.5$ Hz, 1H).



Photolysis of **24** was carried out using the same protocol as that for **20**. In a quartz J. Young NMR tube is dissolved **24** (10 mg) and t-butyl vinyl ether (20 μL) in spectral-grade acetonitrile (150 μL). The sample is freeze-pump-thawed thrice, then backfilled with an argon atmosphere. The sample is irradiated for 3 hours, then concentrated *in vacuo*. The photolysate is purified by reverse-phase HPLC (C18, 5 – 95% acetonitrile in water) providing **26** as a white residue. ^1H NMR (500 MHz, Chloroform-*d*) δ 10.13 (d, $J = 5.7$ Hz, 1H), 8.63 (d, $J = 8.5$ Hz, 1H), 8.12 (d, $J = 9.3$ Hz, 1H), 8.03 (dd, $J = 8.6, 5.7$ Hz, 1H), 7.74 (d, $J = 9.3$

Hz, 1H), 6.39 (dd, $J = 7.1, 3.1$ Hz, 1H), 4.85 (s, 3H), 3.77 (dd, $J = 16.8, 7.0$ Hz, 1H), 3.43 (dd, $J = 16.9, 3.1$ Hz, 1H), 1.38 (s, 9H). ESI-MS(+) calculated for $[\text{C}_{16}\text{H}_{20}\text{NO}_2]^+$ ($[\text{M}]^+$) 258.1, found 258.1.

7. REFERENCES

1. Hook, G., Jacobsen, J. S., Grabstein, K., Kindy, M. & Hook, V. Cathepsin B is a New Drug Target for Traumatic Brain Injury Therapeutics: Evidence for E64d as a Promising Lead Drug Candidate. *Front. Neurol.* **6**, 178 (2015).
2. Loane, D. J. & Faden, A. I. Neuroprotection for traumatic brain injury: translational challenges and emerging therapeutic strategies. *Trends Pharmacol. Sci.* **31**, 596–604 (2010).
3. DeKosky, S. T., Blennow, K., Ikonovic, M. D. & Gandy, S. Acute and chronic traumatic encephalopathies: pathogenesis and biomarkers. *Nat. Rev. Neurol.* **9**, 192–200 (2013).
4. Morries, L. D., Cassano, P. & Henderson, T. A. Treatments for traumatic brain injury with emphasis on transcranial near-infrared laser phototherapy. *Neuropsychiatr. Dis. Treat.* **11**, 2159–2175 (2015).
5. Naeser, M. A., Saltmarche, A., Kregel, M. H., Hamblin, M. R. & Knight, J. A. Improved Cognitive Function After Transcranial, Light-Emitting Diode Treatments in Chronic, Traumatic Brain Injury: Two Case Reports. *Photomed. Laser Surg.* **29**, 351–358 (2011).
6. Henderson, T. A. & Morries, L. D. Near-infrared photonic energy penetration: can infrared phototherapy effectively reach the human brain? *Neuropsychiatr. Dis. Treat.* **11**, 2191–2208 (2015).
7. Solntsev, K. M., Huppert, D. & Agmon, N. Photochemistry of ‘Super’-Photoacids. Solvent Effects. *J. Phys. Chem. A* **103**, 6984–6997 (1999).
8. Solntsev, K. M., Huppert, D., Agmon, N. & Tolbert, L. M. Photochemistry of ‘super’ photoacids. 2. Excited-state proton transfer in methanol/water mixtures. *J. Phys. Chem. A* **104**, 4658–4669 (2000).
9. Agmon, N., Rettig, W. & Groth, C. Electronic Determinants of Photoacidity in Cyanonaphthols. *J. Am. Chem. Soc.* **124**, 1089–1096 (2002).

10. Agmon, N. Elementary Steps in Excited-State Proton Transfer \dag. *J. Phys. Chem. A* **109**, 13–35 (2005).
11. Tolbert, L. M. & Haubrich, J. E. Enhanced photoacidities of cyanonaphthols. *J. Am. Chem. Soc.* **112**, 8163–8165 (1990).
12. TOLBERT, L. & HAUBRICH, J. Photoexcited Proton-Transfer From Enhanced Photoacids. *J. Am. Chem. Soc.* **116**, 10593–10600 (1994).
13. Tolbert, L. M. & Solntsev, K. M. Excited-State Proton Transfer: From Constrained Systems to ‘Super’ Photoacids to Superfast Proton Transfer \dag. *Acc. Chem. Res.* **35**, 19–27 (2002).
14. Rosenberg, J. L. & Brinn, I. Excited state dissociation rate constants in naphthols. *J. Phys. Chem.* **76**, 3558–3562 (1972).
15. Fife, T. H. General acid catalysis of acetal, ketal, and ortho ester hydrolysis. *Acc. Chem. Res.* **5**, 264–272 (1972).
16. Dean, K. E. S. & Kirby, A. J. Concerted general acid and nucleophilic catalysis of acetal hydrolysis. A simple model for the lysozyme mechanism. *J. Chem. Soc. Perkin Trans. 2* 428–432 (2002). doi:10.1039/B110948K
17. Kirby, A. J. & Williams, N. H. Efficient intramolecular general acid catalysis of enol ether hydrolysis. Hydrogen-bonding stabilisation of the transition state for proton transfer to carbon. *J. Chem. Soc. Perkin Trans. 2* 643–648 (1994). doi:10.1039/P29940000643
18. Fife, T. H. & Przystas, T. J. Intramolecular general acid catalysis in the hydrolysis of acetals with aliphatic alcohol leaving groups. *J. Am. Chem. Soc.* **101**, 1202–1210 (1979).
19. Fife, T. H. & Anderson, E. Intramolecular carboxyl group participation in acetal hydrolysis. *J. Am. Chem. Soc.* **93**, 6610–6614 (1971).
20. Yates, K. Kinetics of ester hydrolysis in concentrated acid. *Acc. Chem. Res.* **4**, 136–144 (1971).
21. Yates, K. & McClelland, R. A. Mechanisms of ester hydrolysis in aqueous sulfuric acids. *J. Am. Chem. Soc.* **89**, 2686–2692 (1967).
22. Kirby, A. J. in *Advances in Physical Organic Chemistry* (ed. Bethell, V. G. and D.) **17**, 183–278 (Academic Press, 1981).

23. Yoshimi, Y., Maeda, H., Hatanaka, M. & Mizuno, K. Intramolecular 9-membered hydrogen bonding of 2-arylmethylphenols having carbonyl groups at 2'-position. *Tetrahedron* **60**, 9425–9431 (2004).
24. Gorka, A. P., Nani, R. R., Zhu, J., Mackem, S. & Schnermann, M. J. A Near-IR Uncaging Strategy Based on Cyanine Photochemistry. *J. Am. Chem. Soc.* **136**, 14153–14159 (2014).
25. Nani, R. R., Kelley, J. A., Ivanic, J. & Schnermann, M. J. Reactive species involved in the regioselective photooxidation of heptamethine cyanines. *Chem. Sci.* (2015). doi:10.1039/C5SC02396C
26. Budyka, M. F., Sadykova, K. F. & Gavrishova, T. N. Energy transfer, fluorescence and photoisomerization of styrylquinoline–naphthol dyads with dioxypolymethylene bridges. *J. Photochem. Photobiol. Chem.* **241**, 38–44 (2012).
27. Catalán, J., del Valle, J. C., Palomar, J., Díaz, C. & de Paz, J. L. G. The six-membered intramolecular hydrogen bond position as a switch for inducing an excited state intramolecular proton transfer (ESIPT) in esters of O-hydroxynaphthoic acids. *J. Phys. Chem. A* **103**, 10921–10934 (1999).
28. Cordes, E. H. & Bull, H. G. Mechanism and catalysis for hydrolysis of acetals, ketals, and ortho esters. *Chem. Rev.* **74**, 581–603 (1974).
29. Wagner, P. J. & Hammond, G. S. Mechanism of Type II Photoelimination I. *J. Am. Chem. Soc.* **87**, 4009–4011 (1965).
30. Hibbert, F. & Spiers, K. J. Intramolecular catalysis of the hydrolysis of an acetal by an internally hydrogen-bonded hydroxy group. *J. Chem. Soc. Perkin Trans. 2* 377–380 (1989). doi:10.1039/P29890000377
31. Kirby, A. J. & Williams, N. H. Efficient intramolecular general acid catalysis of vinyl ether hydrolysis by the neighbouring carboxylic acid group. *J. Chem. Soc. Chem. Commun.* 1643–1644 (1991). doi:10.1039/C39910001643
32. Yoon, U. C. *et al.* Exploratory and mechanistic aspects of the electron-transfer photochemistry of olefin-N-heteroaromatic cation systems. *J. Am. Chem. Soc.* **105**, 1204–1218 (1983).

MECHANISTIC STUDIES ON THE TRIMETHYL LOCK CYCLIZATION OF SULFUR-SUBSTITUTED BENZOQUINONES TRIGGERED BY VISIBLE LIGHT

Abstract

A new photochemical method that is useful for the decaging of a wide variety of bioactive compounds has been developed based on an intramolecular photoredox reaction of sulfur-substituted benzoquinones. Visible-light reduction of the quinone leads to exposure of a nucleophilic hydroquinone, which undergoes rapid lactonization through the well-known trimethyl lock decaging process. Classical mechanistic tools such as radical clocks, triplet studies, and isotope effects as well as laser flash-photolysis are used to determine the key mechanistic details. Results reveal that the photoreaction commences through a charge-transfer state that undergoes a critical hydrogen shift from the sulfide substituent to the benzoquinone. Additionally, not only does the sulfur substituent enable the photochemistry to be conducted at wavelengths as long as 455 nm, it also increases the selectivity for the desired pathway, resulting in quantitative yields for release of the caged compound.

1. INTRODUCTION & SYNTHESIS

Our lab recently described a new class of compounds that undergo photochemical decaging of a wide range of substrates at wavelengths as long as 600 nm¹. Such compounds could find use as chemical biology tools, and in therapeutic settings, where longer wavelengths lead to deeper tissue penetration. In an effort to maximize decaging efficiency and to provide insights into possible strategies for extending the photoreactivity to even longer wavelengths, we have conducted extensive mechanistic studies of the photoreaction. Here we describe those mechanistic studies and the design strategies they suggest.

The initial approach sought to take a known *chemical* decaging process and design systems that could be phototriggered. Figure 1A shows two variants of the well-established trimethyl lock system²⁻⁴. Either reducing a quinone or revealing a phenol produces a

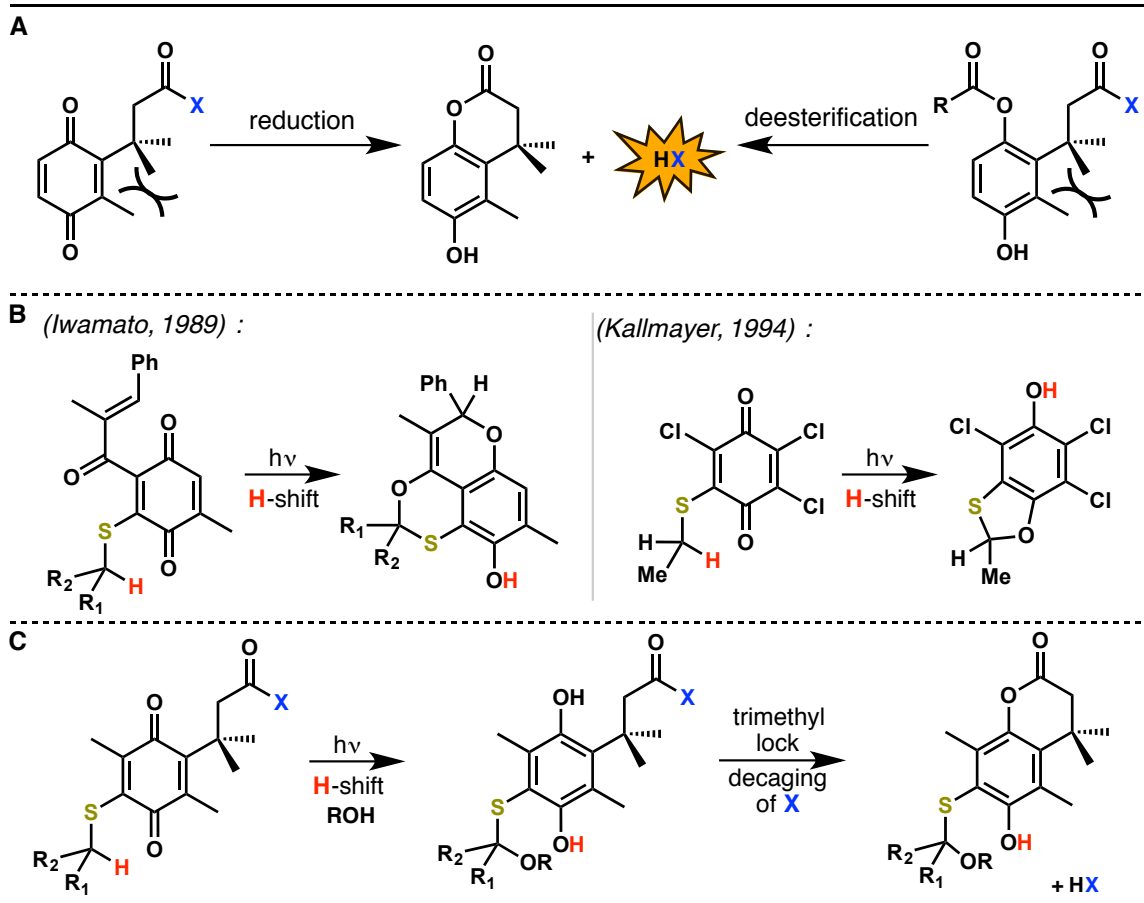


Figure 1. **A)** Variants of the trimethyl lock decaging process. **B)** Intramolecular photoreductions of sulfur-substituted quinones. **C)** General design of the photoreductive trimethyl lock strategy implemented in this work.

nucleophile that can exploit the remarkable rate enhancements associated with the trimethyl lock system, releasing **HX** as a generic alcohol, amine, thiol, or phosphate. Of course, deprotection of the phenol can be accomplished photochemically using established caging groups^{5,6}, but this approach does not lead naturally to longer wavelength systems.

The bimolecular photoreduction of quinones by sulfides has been reported, but, in general, the process has not been extensively studied^{7,8}. The process is believed to be initiated by an electron transfer (ET) followed by a crucial C-H oxidation, similar to photoreduction by amines⁹⁻¹². Intramolecular variants are known (Figure 1B)^{13,14}, but for these reactions a direct hydrogen abstraction (Norrish Type II-like) process cannot be ruled out. For the present purposes, we sought to employ an ET mechanism, as this seemed better suited for

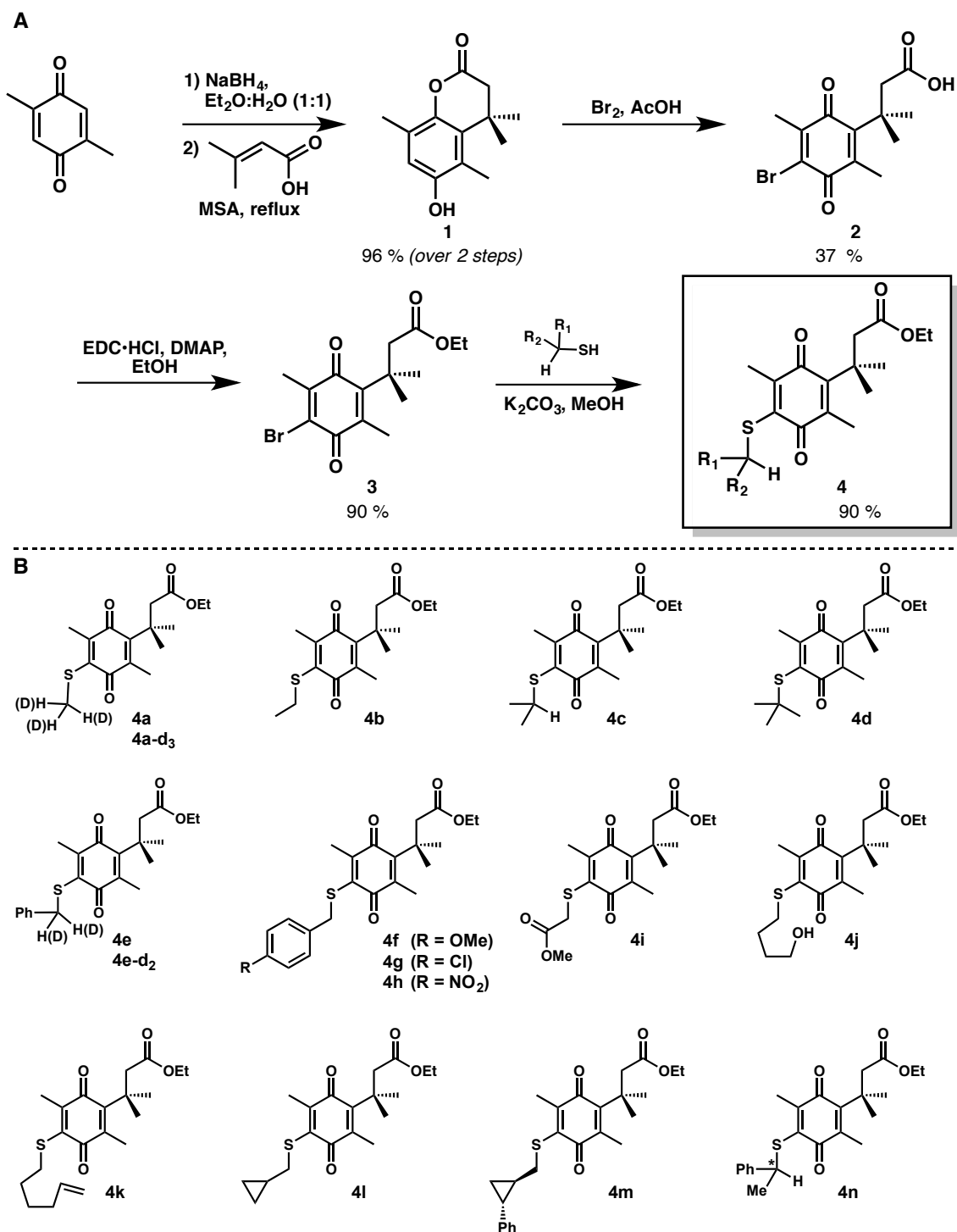


Figure 2. A) Synthesis of quinone sulfide trimethyl lock compounds with caged ethanol.
B) Derivatives of 4 discussed in this work.

longer wavelengths. Although most quinone photoreductions involve amines^{15–22}, we chose a sulfide as the potential electron donor in our initial design (Figure 1C). We anticipated a more facile synthesis of the desired systems, more favorable redox properties, and perhaps greater stability in air and in a biological context. Our initial design is shown in Figure 2 as compound **4**. The synthesis (Figure 2A) is efficient and permits a wide variety of sulfide substituents to be introduced in the last step (Figure 2B). Note that the final two steps in the synthesis can also be reversed in sequence. A representative UV/vis spectrum is shown in Figure 3 for the S-methyl derivative (**4a**). Notably, a broad visible absorption band is observed at approximately 413 nm; the relevant data for this band (λ_{max} and ϵ) have been collected for key substrates and are reported in Table 1. We have been unable to observe luminescence from **4a**, either in fluid media at room temperature or at 77K in a frozen matrix, as is typical of quinones^{23–30}.

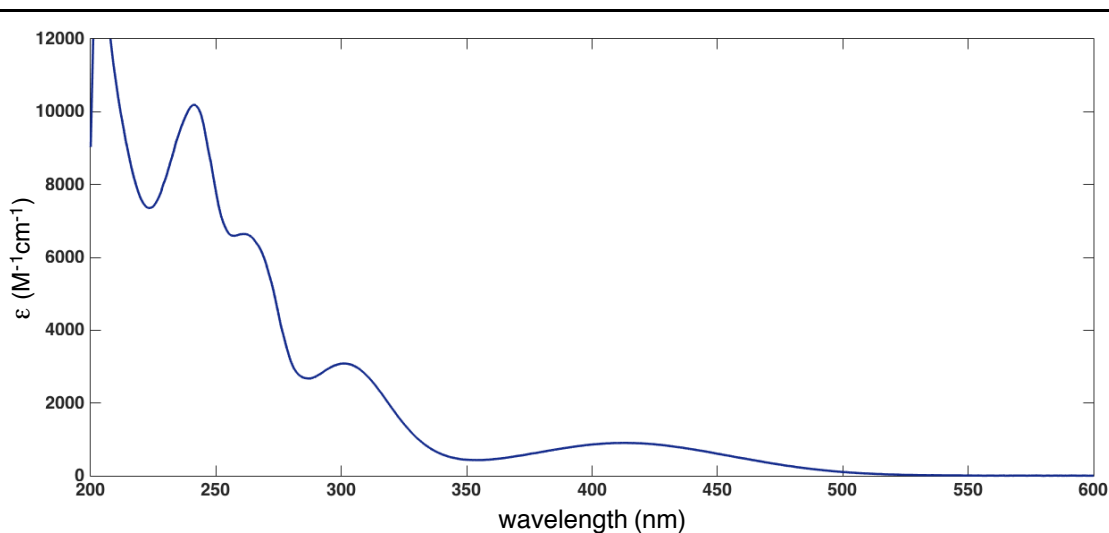


Figure 3. UV/Vis spectrum of **4a** in methanol.

2. STEADY-STATE PHOTOLYSIS

Photolysis of **4a** with, for example, a 420 or 455 nm LED, in air-equilibrated methanol, leads to the release of ethanol and the clean formation of thioacetal **5a** (Figure 4A). Photolysis in water (pure or buffered to pH 7.5) also releases the caged alcohol and produces the disulfide **7**, presumably via a thiohemiacetal intermediate. Both reactions are very clean; quantum yields will be discussed below. In other solvents such as acetonitrile,

benzene, or hexane, the reaction is slower and produces a complex mixture of products. Along with the expected methanol adduct **5**, in some cases the cyclic thioacetal **6** is also produced, presumably by intramolecular capture of the species that is trapped by methanol or water. Compound **4j** contains a tethered alcohol, and upon photolysis in methanol it cleanly produces both **5j** and the expected cyclic product **8** in a 1:4 ratio (Figure 4B). Photolysis of **4j** in acetonitrile or benzene also produces **8**, but there are also other uncharacterized products in the crude reaction mixture. Compounds **4h** and **4i**, both possessing electron-withdrawing groups, are peculiar in that they produce unidentified decomposition products upon photolysis, and display visible absorption bands that are weak and blue-shifted (Table 1). It is clear that some of the decomposition products have not undergone trimethyl lock cyclization, suggesting that unmasking of the phenol has not occurred. Compound **4d** lacks the necessary γ -hydrogen on sulfur and is found to be nonreactive to photolysis at 420 nm. By comparison, compound **9** lacks a sulfur substituent altogether, and is found to undergo γ -hydrogen abstraction from the trimethyl lock side chain. Similar processes have been previously reported^{7,31–37}.

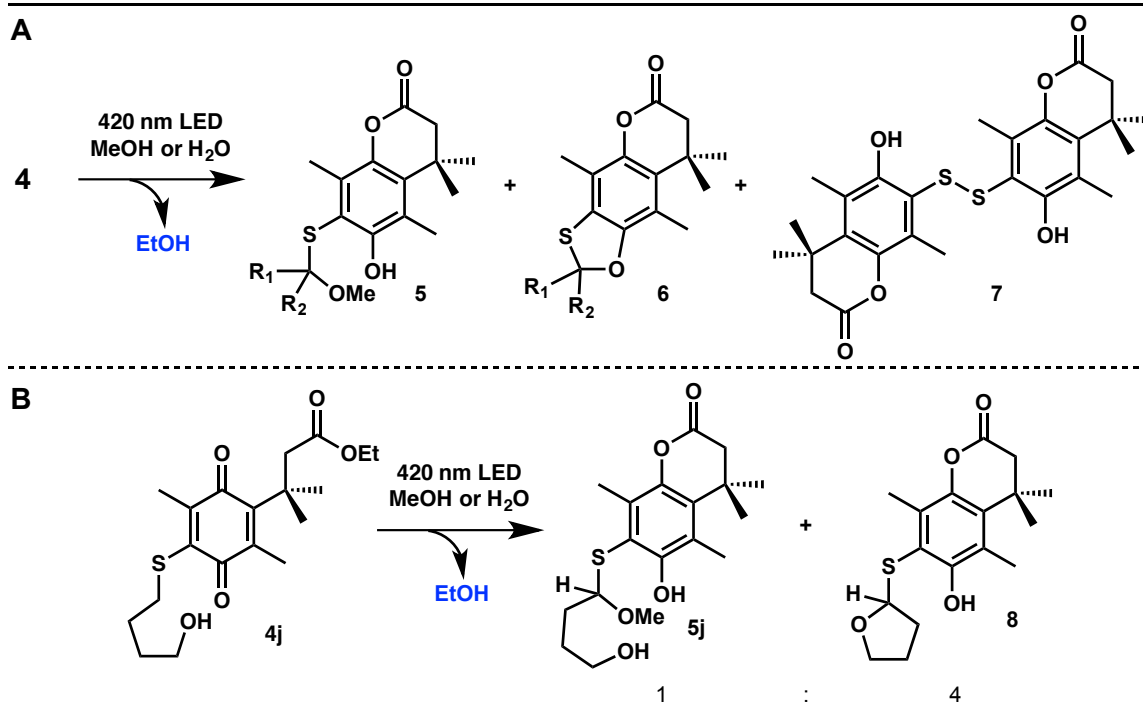
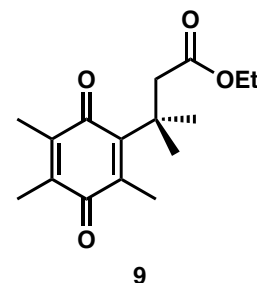


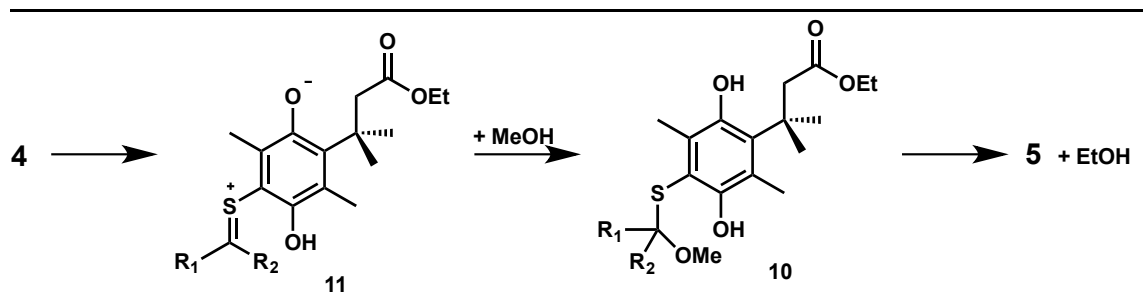
Figure 4. Products of photolysis of **4** at 420 nm in methanol or water.

3. MECHANISTIC INVESTIGATIONS

3.1 Quantum Yields and Radical Probes

Most of our mechanistic studies have been conducted in methanol, where the reaction is clean and solubility is not an issue. It is simplest to consider the mechanism by working backwards from the final product.

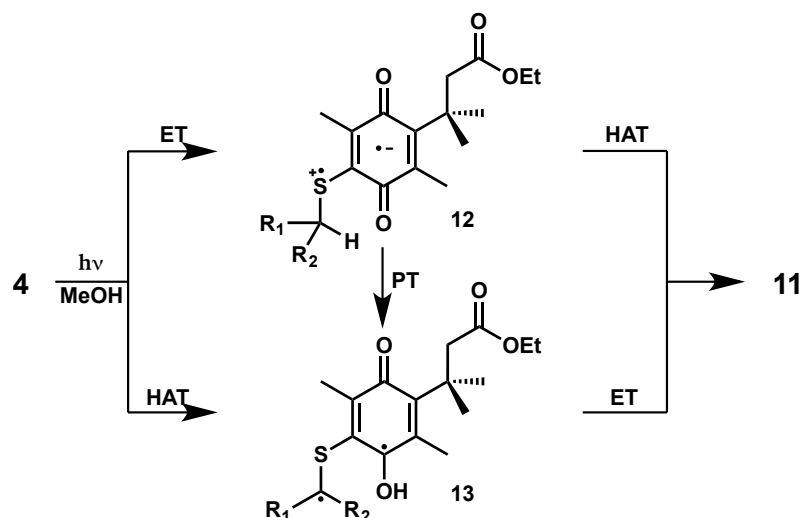
It is clear that the actual ring closure of the trimethyl lock and the release of the caged compound is the final and slowest step of the process. One could have imagined that an initial photochemical ET from the sulfide to the quinone would build enough negative charge on the quinone oxygens such that a trimethyl lock closure could occur before further reduction of the quinone¹⁸, but that is not the case. In methanol, the hydroquinone (**10**), shown in Scheme 1, can be directly observed prior to trimethyl lock ring closure. In aqueous systems the ring closure is rapid for an alcohol leaving group, but not for an amine leaving group, again allowing the hydroquinone to be observed prior to trimethyl lock closure. These results could be anticipated based on known trimethyl lock rates².



Scheme 1. Solvent trapping of zwitterion **11** to generate hydroquinone **10**.

The mechanistic issue then becomes the conversion of quinone **4** to the methanol adduct hydroquinone, **10**. The requirement for a solvent capture step implicates zwitterion **11** as the likely precursor to **10**. Conceptually, the conversion of **4** to **11** then requires reduction of the quinone by two electrons and the shift of a proton from the carbon attached to the sulfur (β -carbon) to the quinone oxygen. The issue is the sequence of events and what combination of ET, proton transfer (PT), and/or hydrogen atom transfer (HAT) is involved

in the process (Scheme 2). To keep the semantics straight, we will use the term hydrogen-shift as noncommittal regarding all steps in the process $4 \rightarrow 11$.



Scheme 2. Potential intermediates in the hydrogen shift reaction of **4** to **11**.

We have applied a number of classical mechanistic tools to this reaction. First, the influence of substituents on the sulfide on the quantum yield for product formation was probed. Using a ferrioxalate actinometer we have determined the quantum yield (Φ) for the conversion of **4** in degassed methanol solutions, and the results are summarized in Table 1. The effect of added oxygen on the quantum yield is generally small and will be discussed further below. There is a trend of *i*Pr (**4c**) > Et (**4b**) > Me (**4a**) in relative quantum yield, although the effect is not large. A benzyl substituent (**4e**) shows the largest effect, with greater than a 5-fold increase in quantum yield. These trends would be consistent with either radical or cationic character building up on the β -carbon. However, substituted benzyl compounds (**4f** and **4g**) do not follow a simple trend, and we note again that the *p*-nitrobenzyl substrate **4h** produces a complex mixture of products.

We next considered the role of the hydrogen shift on the overall process. There is an isotope effect ($\Phi_{\text{H}}/\Phi_{\text{D}}$) on the quantum yield for quinone disappearance. A value of 4.0 is obtained for the *S*-methyl compound (**4a** vs. **4a-d₃**), and 2.5 for the *S*-benzyl compound (**4e** vs. **4e-d₂**) (Table 1). These effects highlight the critical role of the hydrogen-shift in the

Table 1. Spectroscopic and photolysis data for disappearance of **4** in degassed

methanol. ⁿ 4	λ_{\max}^a (nm)	ϵ^a (M ⁻¹ cm ⁻¹)	Φ^b (%)	τ^c (ns)	Φ^S^d (%)	Φ^T^d (%)	$\Phi_{\text{rxn}}^T^e$ (%)	Φ_{isc}^f (%)	$k_{\text{rxn}}^T^g$ (10 ⁵ s ⁻¹)
4a	413	903	1.2	930	1.0	0.2	21	0.9	2.3
4a-d₃	413	923	0.3	1070	0.27	0.03	0.3	10	0.03
4b	414	1005	1.7	750	1.5	0.2	15	1.3	2.0
4c	411	927	2.2	543	1.6	0.6	21	2.8	3.9
4e	413	951	6.3	143	3.0	3.3	73	4.5	51
4e-d₂	412	944	2.5	577	1.0	1.5	42	3.5	7.3
4f	410	953	3.1	600	–	–	44	–	7.3
4g	409	832	5.2	180	–	–	89	–	49
4h	396	709	0.6	–	–	–	–	–	–
4i	394	604	0.6	–	–	–	–	–	–

^a Data reported for the longest wavelength absorption band in air-equilibrated methanol. ^b Quantum yield for disappearance of **4** at 420 nm in degassed methanol. ^c Lifetime of the transient observed at 480 nm upon pulsed laser irradiation at 355 nm in degassed methanol. ^d Quantum yield of quinone disappearance due to singlet (S) and triplet (T) pathways, determined from quenching studies. ^e Minimum value of the quantum efficiency for disappearance of quinone from the sensitized triplet state. ^f Quantum efficiency of intersystem crossing. ^g Rate constant for reaction from the triplet state. ^h All quantum yields measured relative to ferrioxalate and are reported with a standard deviation of < 10%. (–) = measurement was not attempted or could not be calculated.

overall process. Either an ET-PT or HAT mechanism could potentially generate biradical **13** (Scheme 2), with the HAT mechanism being a conventional Norrish II reaction. To probe for the intermediacy of **13**, we introduced radical clocks to the system, preparing the 5-hexenyl (**4k**), cyclopropylmethyl (**4l**), and 2-phenylcyclopropylmethyl (**4m**) derivatives. These are standard probes that have been used successfully in conventional Norrish II reactions^{38–42}. For both **4k** and **4l**, no radical rearrangement is seen; the products **5** and **6** are cleanly produced. The phenylcyclopropyl clock shows a very fast intrinsic ring opening rate of 10¹¹ s⁻¹^{38,43}. Photolysis of **4m** produces a 20% yield of the expected methanol trapping product (**5m**) with the phenylcyclopropyl ring still intact. The remaining material is a complex mixture of products that was unable to be fully characterized. While it is likely true that the sulfur in our system perturbs the radical rearrangements studied here, it still seems safe to conclude that if a biradical such as **13** is directly formed in this system, it has a very short lifetime.

An especially telling probe of the role of the hydrogen shift was provided by a stereochemical test. Enantiomerically pure phenethyl derivative **4n** was prepared with >95% ee. Upon photolysis to 75% conversion, recovered starting material showed no racemization. These results establish that, regardless of whether it is HAT or PT and regardless of when it

occurs in the process, *the hydrogen shift is irreversible*. The system is committed to product once the hydrogen shift has occurred, making this a key mechanistic event.

3.2 Laser Flash Photolysis

To provide further insight into possible mechanisms for this reaction, we have studied this system using nanosecond laser flash photolysis with transient absorption. Briefly, samples were excited at 355 nm with an 8 ns pulse at 10 Hz. On excitation of **4a** in methanol, a transient with an absorption maximum at 480 nm is observed (Figure 5). It decayed in a single exponential with a lifetime (τ) of 930 ns under degassed conditions. Similar transients are seen from a number of structures (Table 1). In all cases we have shown that the products formed in the laser experiments are the same as in the steady-state photolysis. In air-equilibrated solutions, the same transient is observed, but in all cases the lifetime is in the 100 to 200 ns range, indicating diffusional quenching by oxygen. The transient is also

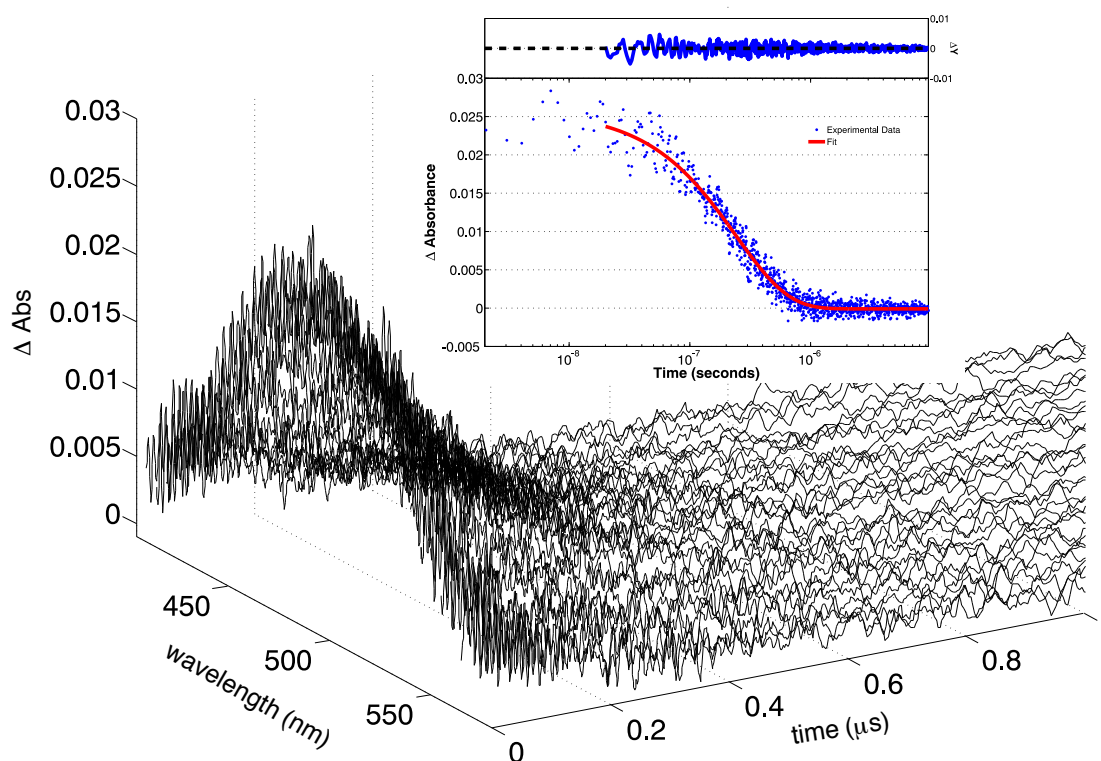


Figure 5. Transient absorption spectrum of **4a** observed upon laser flash photolysis at 355 nm in degassed methanol. Inset: single exponential fit (red) of transient decay at 480 nm.

quenched by amine-based quenchers. Considering the parent, **4a**, in the presence of 10 mM TEA, an initial decay with a lifetime of 310 ns is seen, compared to 930 ns in the absence of TEA.

As shown in Table 1, there is a considerable variation in lifetime (τ) for the 480 nm transient. For the simple hydrocarbon systems (methyl, ethyl, isopropyl, benzyl), the transient lifetime tracks the product quantum yield measured in bulk, with the benzyl transient being significantly shorter lived than the methyl. As in the bulk photolysis, a significant isotope effect is seen for the transient lifetime for the benzyl compound (**4e** vs. **4e-d₂**). However, a minimal isotope effect is seen for the methyl compound (**4a** vs **4a-d₃**). The t-butyl compound, **4d**, does not display a transient that is observable by our detection system, suggesting that the species responsible for the transient is either too short-lived, formed with little efficiency, or both.

3.3 Sensitization and Quenching Studies

Excitation of quinones typically produces a triplet state with near unit efficiency^{23,24}. The present system, however, is significantly perturbed, electronically by the sulfur substituent and geometrically by the bulky trimethyl lock system. The long lifetime of the transient from the flash photolysis studies, and the fact that it is quenched efficiently by oxygen, suggest that the transient is a triplet. However, in steady-state photolysis studies, oxygen has only a small effect on the quantum yield. We have undertaken several studies to probe the role and nature of the triplet state in the photoreaction.

We initially considered the impact of triplet quenchers on the overall process, and obtained clean quenching with diethylaniline. Shown in Figure 6 are Stern-Volmer (SV) plots for photoreaction of the methyl (**4a**) and benzyl (**4e**) compounds, where Φ_q is defined as the quantum yield in the presence of quencher. At low concentrations of diethylaniline (up to approximately 1 mM), near-linear SV behavior is observed (Figure 6, inset). However, at higher concentrations (up to approximately 100 mM), the SV plot deviates from linearity and essentially plateaus. This indicates that the photoreaction proceeds through two different pathways, one being much more efficiently quenched than the other. We have assigned the less and more quenchable portion of the photoreaction to that which occurs through the

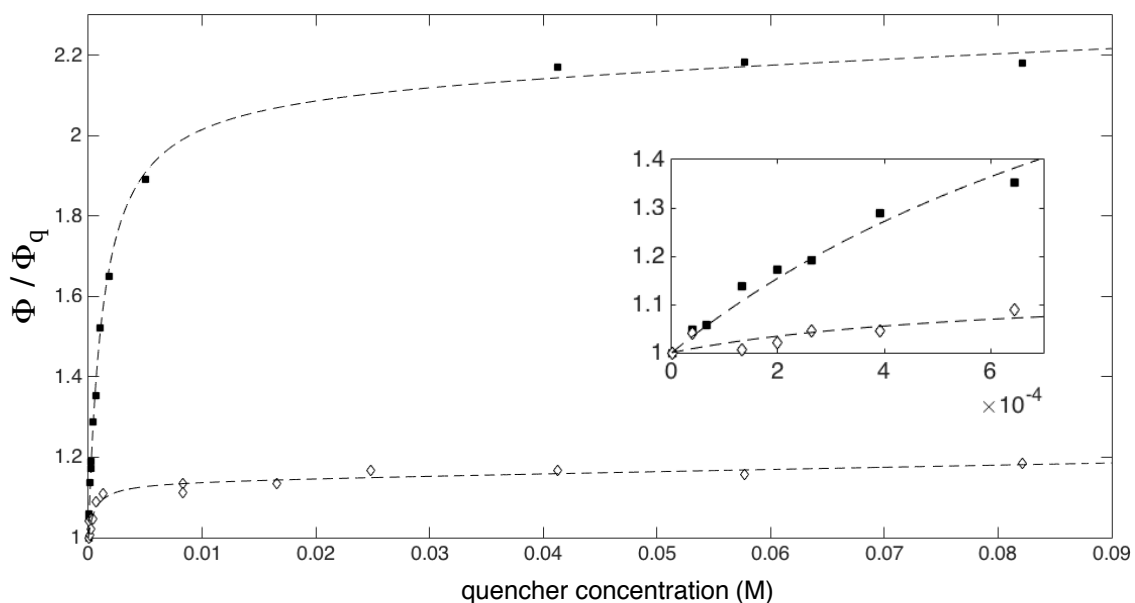


Figure 6. Stern-Volmer plot for the quenching of the quantum yield for disappearance of **4a** (white diamonds) and **4e** (black squares) by diethylaniline. Dotted curves are multivariable regression fits to Eq. 2. Inset is the low concentration region of the plot.

singlet (Φ^S) and triplet (Φ^T) pathways, respectively, where the sum of these pathways provides the overall quantum yield (Eq. 1).

$$\Phi = \Phi^S + \Phi^T \quad (1)$$

$$\frac{\Phi}{\Phi_q} = \frac{(1+K_{SV}^S[Q])(1+K_{SV}^T[Q])}{1+a} \quad \text{where } a = \frac{K_{SV}^T[Q]}{1+(\Phi^T/\Phi^S)} \quad (2)$$

Eq. 2 has been previously derived to describe the effect of quencher concentration, $[Q]$, on the quantum yield when there are two quenchable pathways⁴⁴. A regression analysis fitting of the data in Figure 6 to Eq. 2, which takes as parameters the two SV quenching constants for the singlet and triplet pathways (K_{SV}^S and K_{SV}^T , respectively) and the ratio of their quantum yields (Φ^T/Φ^S), results in the curves shown in Figure 6. This analysis has been performed for key substrates (Supporting Information), and the resulting values of Φ^S and Φ^T are reported in Table 1, after insertion of the calculated ratios (Φ^T/Φ^S) into Eq. 1. As expected, the triplet pathways of **4a** and **4e** are strongly quenched with similar K_{SV}^T values of 1800 and 1700 M^{-1} , respectively. The singlet states are also similarly quenched, although with low K_{SV}^S values of 0.45 and 0.52 M^{-1} . The two compounds, however, differ largely in

their ratios of singlet to triplet reactivity, Φ^T/Φ^S . The calculated ratios reveal that for **4a**, the reaction proceeds 88% on the singlet pathway and 12% on the triplet pathway. For **4e** the proportions are 47% through the singlet and 53% through the triplet. If we assume that the transient observed in laser flash photolysis is the triplet being quenched by diethylaniline, we can use the transient lifetimes (τ) and K_{SV}^T values to obtain k_q , the second-order rate constant for quenching. We find k_q to be $10 \times 10^9 \text{ M}^{-1}\text{s}^{-1}$ and $2 \times 10^9 \text{ M}^{-1}\text{s}^{-1}$ for **4a** and **4e**, respectively, which are near the diffusion-controlled values in methanol, where $k_{\text{diff}} = 1.2 \times 10^{10} \text{ M}^{-1} \text{ s}^{-1}$.

The results from the quenching experiments reveal that the overall quantum yield (Φ , Table 1) measured in the steady-state photolysis can be defined as the sum of quantum yields for disappearance of quinone through singlet (Φ^S) and triplet (Φ^T) pathways (Eq. 1). A minimal model describing the relevant steps that contribute to these pathways is shown in Figure 7, where nonproductive processes have been omitted for clarity. According to this model, the quantum yield from the singlet (Φ^S) due to direct photolysis of the quinone is defined by the pathway $S_0^Q \rightarrow S_1^Q \rightarrow 11 \rightarrow 10 \rightarrow 5$. The conversion of $11 \rightarrow 10 \rightarrow 5$ occurs

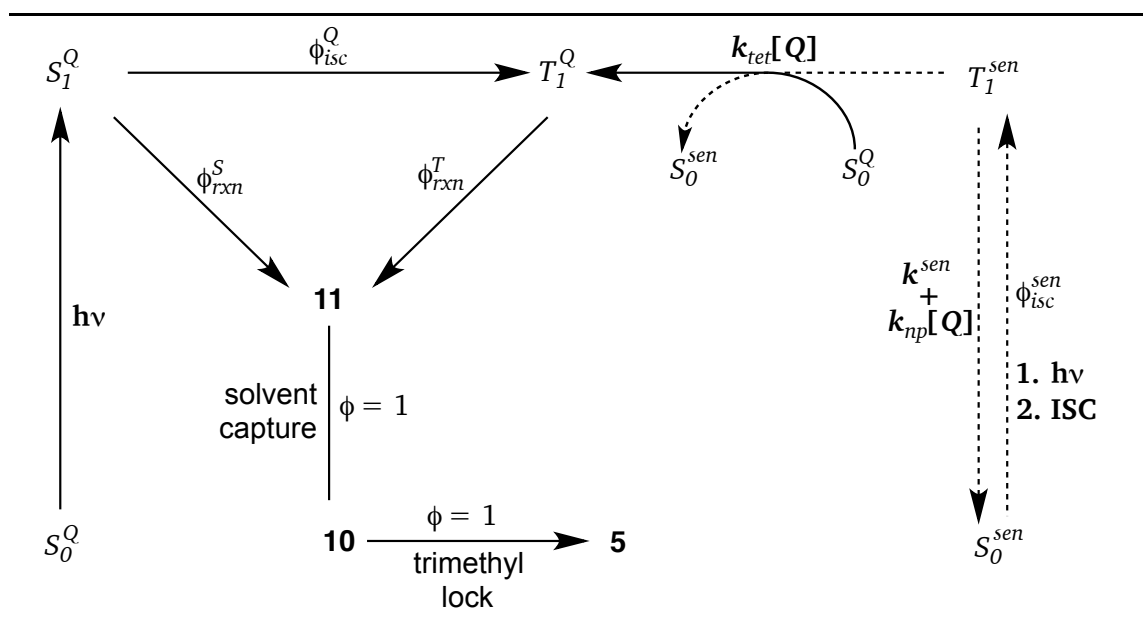


Figure 7. Processes that contribute to the direct and sensitized quantum yields of quinone decay. States: S_0^Q = ground-state quinone; S_1^Q = excited-singlet quinone; T_1^Q = triplet quinone; S_0^{sen} = ground-state sensitizer; T_1^{sen} = triplet sensitizer; Quantum Efficiencies: ϕ_{isc}^Q = intersystem crossing of the quinone; ϕ_{rxn}^S = formation of product from the singlet; ϕ_{rxn}^T = formation of product from the triplet; ϕ_{isc}^{sen} = intersystem crossing of the sensitizer; Rate Constants: k^{sen} = intrinsic deactivation of triplet sensitizer; $k_{tet}[Q]$ = deactivation of sensitizer via productive collisions with quinone; $k_{np}[Q]$ = deactivation of sensitizer via nonproductive collisions with quinone. Solid arrows represent paths taken by quinone; dashed arrows represent paths taken by sensitizer

with unit efficiency, as evidenced by the clean formation of product and the irreversibility of the hydrogen-shift. Φ^S is therefore simply defined by the efficiency of $S_1^Q \rightarrow \mathbf{11}$ (ϕ_{rxn}^S).

Likewise, disappearance of quinone via the triplet state (Φ^T) due to direct photolysis is defined by the pathway $S_0^Q \rightarrow S_1^Q \rightarrow T_1^Q \rightarrow \mathbf{11} \rightarrow \mathbf{10} \rightarrow \mathbf{5}$. The quantum yield for this process, given by Eq. 3, is constructed as the product of the contributing efficiencies, namely ϕ_{isc}^Q , the efficiency of triplet formation via intersystem crossing (*isc*), and ϕ_{rxn}^T , conversion of the triplet to zwitterion **11**.

$$\Phi^T = \phi_{isc}^Q \cdot \phi_{rxn}^T \quad (3)$$

We sought to explore the nature of this triplet pathway in more detail through the use of triplet sensitizers. Many efforts to employ certain sensitizers were either ineffective (acetophenone, benzophenone, methylene blue) or produced undesired side products (biacetyl, naphthalene, anthracene, rose bengal). However, thioxanthone produced clean and consistent results.

Shown in Figure 7 are processes that contribute to the sensitized quantum yield for quinone disappearance. For clarity, steps taken the by the sensitizer are shown with dashed arrows. The pathway begins with excitation and *isc* of the sensitizer, $S_0^{sen} \rightarrow T_1^{sen}$, followed by bimolecular triplet energy transfer (*tet*) to the quinone, $T_1^{sen} + S_0^Q \rightarrow S_0^{sen} + T_1^Q$. Conversion of the triplet quinone to product then proceeds normally ($T_1^Q \rightarrow \mathbf{11} \rightarrow \mathbf{10} \rightarrow \mathbf{5}$). The quantum yield for this pathway (Φ_{sen}) is given by the product shown in Eq. 4, where ϕ_{isc}^{sen} is the efficiency of *isc* for the sensitizer, and ϕ_{tet} is the efficiency of triplet energy transfer. The latter depends upon the concentration of quinone, [Q], and is described by Eq. 5, where k_{sen} is the first-order rate constant that describes the intrinsic decay of the triplet sensitizer, and $k_{tet}[Q]$ and $k_{np}[Q]$ are first-order rate constants for deactivation of the sensitizer through productive and nonproductive collisions with the quinone, respectively.

$$\Phi_{sen} = \phi_{isc}^{sen} \cdot \phi_{tet} \cdot \phi_{rxn}^T \quad (4)$$

$$\phi_{tet} = \frac{k_{tet}[Q]}{k_{sen} + k_{tet}[Q] + k_{np}[Q]} \quad (5)$$

Insertion of Eq. 5 into Eq. 4, and taking the inverse reveals a double-reciprocal linear relationship between the sensitized quantum yield and quinone concentration (Eq. 6), where

the ratio (k_{tet} / k_{sen}) is recognized as a Stern-Volmer constant, K_{SV} , for the productive quenching of the triplet sensitizer by quinone. The reciprocal of the y-intercept in Eq. 6 is designated as Φ_{sen}^{lim} (Eq. 7), and it describes the sensitized quantum yield for quinone disappearance in the limit where deactivation of the triplet sensitizer occurs exclusively through collisions with the quinone.

$$\frac{1}{\Phi_{sen}} = \frac{1}{\phi_{isc}^{sen} \cdot \phi_{rxn}^T} \left(\frac{1}{K_{SV}} \cdot \frac{1}{[Q]} + \frac{k_{tet} + k_{np}}{k_{tet}} \right) \quad (6)$$

$$\Phi_{sen}^{lim} = \phi_{isc}^{sen} \cdot \phi_{rxn}^T \cdot \frac{k_{tet}}{k_{tet} + k_{np}} \quad (7)$$

Using the reported efficiency of intersystem crossing for thioxanthone (ϕ_{isc}^{sen}) of 0.56^{45,46}, a minimum value for ϕ_{rxn}^T can be calculated from Eq. 7 in the limit that all collisions are productive, i.e. $\frac{k_{tet}}{k_{tet} + k_{np}} = 1$. Representative double-reciprocal plots are shown in Figure 8 for **4a**, **4e**, and the deuterated analogs **4a-d₃** and **4e-d₂**. Determination of Φ_{sen}^{lim} from the trendline is accomplished by averaging three independent samples, and calculated values of ϕ_{rxn}^T for key substrates have been collected in Table 1. Although the standard deviation in Φ_{sen}^{lim} is consistently less than 10% (Figure 8, error bars), we note that

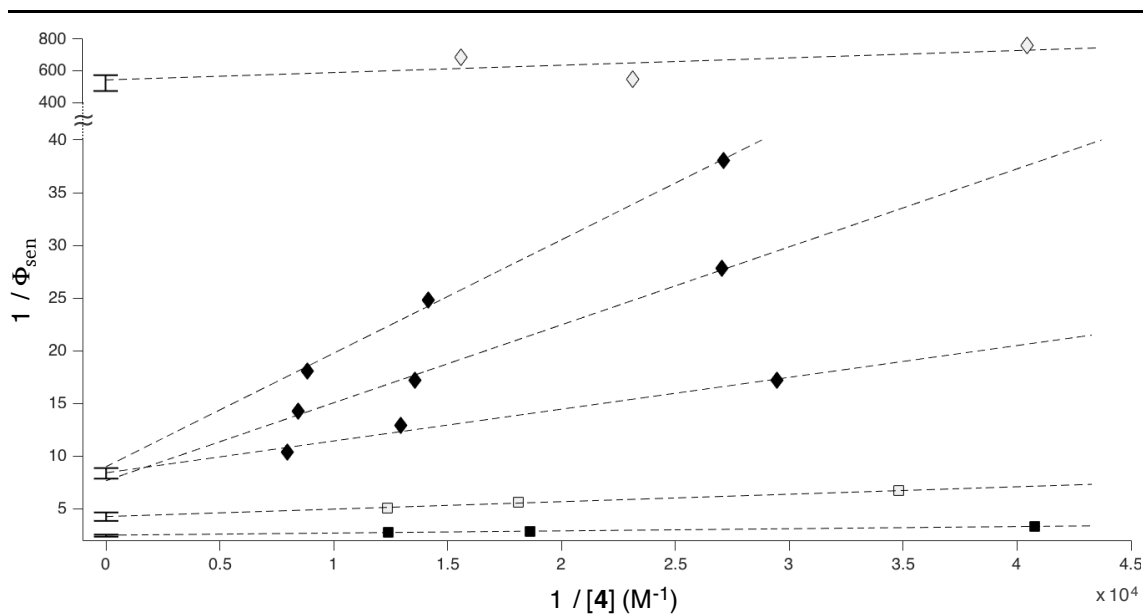


Figure 8. Double reciprocal plots for the sensitized photolysis of **4** by thioxanthone in degassed methanol. **4e** (■), **4e-d₂** (□), **4a** (◆), **4a-d₃** (◇). Dotted lines are linear fits; error bars are the standard deviation in the y-int for three independent samples. Three samples of **4a** using different concentrations of thioxanthone are shown to demonstrate that the slope, but not the y-intercept, is affected.

the slope in the double-reciprocal plots is unexpectedly sensitive to the concentration of thioxanthone. This fact is demonstrated explicitly for **4a**, where three samples containing 1, 2, and 3 mM thioxanthone resulted in incremental shifts in the slope. The y-intercept, however, is clearly unaffected, and the phenomenon was not further probed.

In general, ϕ_{rxn}^T is much larger than Φ , suggesting that the sensitized state is not efficiently generated by direct photolysis. Substitution of ϕ_{rxn}^T into Eq. 3 permits calculation of the efficiency of *isc* (ϕ_{isc}^O , Table 1) in the direct photolysis of **4**. Although quinones typically form triplets with near unit efficiency²³, the efficiencies observed in this system do not exceed 10%, perhaps due to the electronic and steric effects of the sulfide and trimethyl lock substituents, respectively.

The fact that the reaction is intrinsically more efficient through the triplet than the singlet is not unusual since triplet states are generally longer-lived. The first-order rate constants for reaction from the triplet state (k_{rxn}^T) can be calculated using Eq. 8 if we assume that the triplet is the transient observed in laser-flash photolysis. Although the results, collected in Table 1, reflect broad trends in BDE, with the simple alkyl substituents **4a** – **4c** reacting slower than a benzylic substituent **4e**, the rates are clearly complicated by other factors. For instance, the fact that the methyl (**4a**) and isopropyl (**4c**) derivatives have essentially the same rate constant cannot be explained using BDE arguments alone.

$$\phi_{rxn}^T = k_{rxn}^T \cdot \tau \quad (8)$$

Significant isotope effects on the sensitized quantum yield (ϕ_{rxn}^T) are also observed in Figure 8 and Table 1. For the **4e/4e-d₂** system, a magnitude of 1.7, given by the ratio $\phi_{rxn}^{T,4e} / \phi_{rxn}^{T,4e-d_2}$, is similar to the magnitude of 2.5 observed upon direct photolysis, given by the ratio of the values for Φ . Application of Eq. 8 to these data reveal a large normal KIE (k_H/k_D) of 7. In contrast, the **4a/4a-d₃** system experiences a very large sensitized product isotope effect of 70, relative to a direct photolysis isotope effect of 4. In particular, we find that the sensitized photoreaction of **4a-d₃** is very inefficient, with a triplet quantum efficiency (ϕ_{rxn}^T) of 0.03, similar to the efficiency for direct photolysis (Φ). Calculation of the KIE for the **4a/4a-d₃** system from the transient lifetimes and Eq. 8 yields a value (k_H/k_D) of 70. That the KIE and product isotope effects are the same within error for **4a**, but not for **4e** reflects

the low and high efficiencies for these reactions, respectively. In the calculation of k_H/k_D using Eq. 8 for a low efficiency reaction, the ratio of the lifetimes (τ_H/τ_D) approaches unity, and the KIE is predominantly determined by the quantum yield ratio (ϕ_H/ϕ_D). Therefore, the accuracy in the KIE recorded for the **4a/4a-d₃** system primarily results from accurate measurement of the sensitized quantum yields (ϕ_{rxn}^T). Since these values have been very consistent (error bars in Figure 8), with standard deviations of 10% or less, and are carefully measured relative to ferrioxalate, a tried and true actinometer, it is difficult to conceive how the KIE for **4a/4a-d₃**, although anomalously large, is a result of systematic or random error.

4. MECHANISTIC INTERPRETATION

Based on the accumulated evidence, we believe that the most plausible mechanism is the one outlined in more detail in Figure 9, where the difference between **4a** and **4e** has been emphasized. The penultimate intermediate is the zwitterion **11**; once it is formed, product formation involves solvent capture and subsequent trimethyl lock ring closure. Regardless of how it is formed, the formation of **11** is irreversible, as evidenced by the stereochemical labeling studies.

For most of the substrates, product formation is dominated by the singlet pathway, as evidenced by a large contribution of Φ^S to the overall quantum yield, Φ (Table 1).

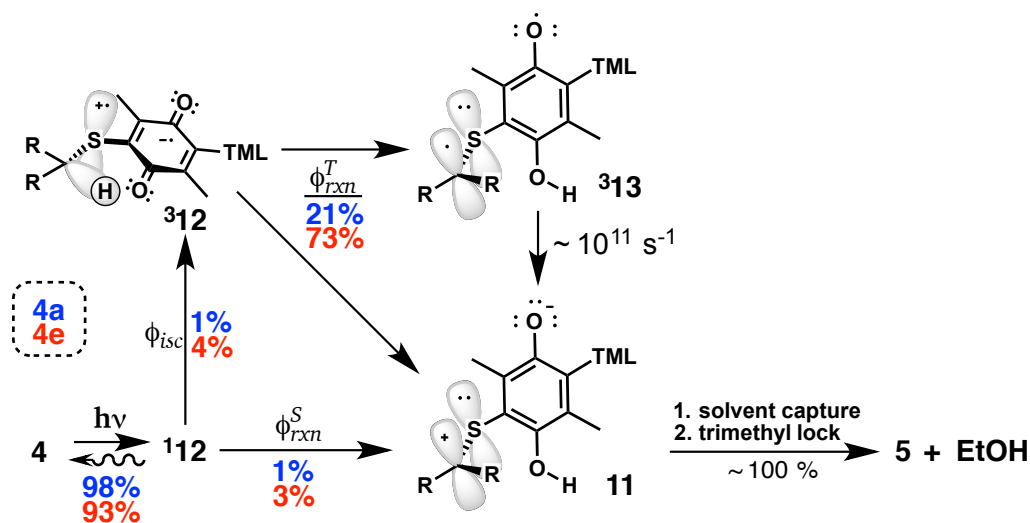


Figure 9. Mechanistic interpretation of the photoreaction of **4** to generate **5**.

However, after photoexcitation, the primary fate of the singlet excited state is actually return to the ground state, which occurs with efficiencies in excess of 90%. The fact that no fluorescence is observed by **4a** suggests that the singlet decays through an efficient internal conversion process, possibly brought on by the sulfur substituent. We consider sulfur to impart considerable polar character to the excited state, and have assigned the S_1 state in Figure 9 as being best represented by the species $^1\mathbf{12}$, the product of initial electron-transfer in the conversion of **4** \rightarrow **11** (Scheme 2). This conclusion is supported by the broad visible absorption band observed in these compounds, which is indicative of charge-transfer (Figure 3)³⁰. Although charge-transfer character in S_1 could be the cause of low quantum yields, it could also perhaps be the reason that the photoreaction is clean, generating the desired products in quantitative chemical yield. Typically, when given the opportunity, benzoquinones will readily undergo γ -hydrogen abstraction^{36,37,47}, and this particular system possesses eight other γ -hydrogens in addition to the sulfur substituent. We have observed that compound **9**, lacking sulfur, undergoes efficient abstraction of the trimethyl lock hydrogens, yet **4d** possessing a t-butyl substituent on sulfur is remarkably photostable. Together these data suggest that the role of the charge transfer is to simultaneously deactivate the intrinsic reactivity of the quinone oxygens and also activate the desired reactivity on the sulfur substituent. The resonance structure of **12** would account for both of these effects.

In addition to hydrogen-shift and deactivation, the singlet also undergoes intersystem crossing (ϕ_{isc}^Q) to the triplet. We conclude that this triplet is the transient observed in the laser flash-photolysis experiments. That the transient is a triplet is supported by quenching data for both oxygen and diethylaniline, and by its long lifetime⁴⁸. Additionally, a significant KIE in the decay for the **4e/4e-d₂** system indicates that the transient is a species that undergoes the hydrogen-shift reaction. A much smaller KIE on the transient decay for the **4a/4a-d₃** system is a consequence of the lower efficiency of reaction from this triplet ($\phi_{rxn}^{T,4a} = 0.2$).

To probe the electronics of the triplet state, we have evaluated several structures of relevance using DFT M06/6-311++G**, and have displayed electrostatic potential surfaces and spin-density plots in Figure 10. While we fully recognize the limitations of a modest level of theory, we are more interested in comparisons between closely related structures,

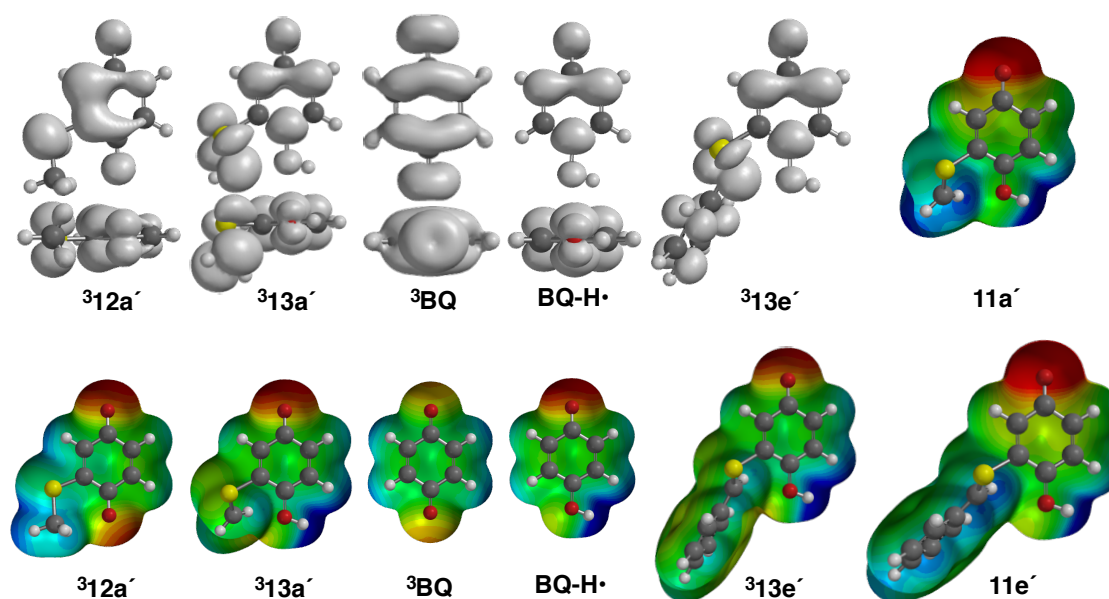


Figure 10. Spin-density (gray) and electrostatic potential surfaces (-200 (red) to 200 (blue) kJ/mol) of relevant structures lacking the trimethyl lock substituents (designated with prime)

rather than precise computational predictions. This level of theory, we believe, can be useful for such purposes. Since we are primarily concerned with the effect of sulfur, we have modeled the reaction using benzoquinones without the trimethyl lock substituents (indicated with a prime), and note that calculations performed on trimethyl lock-containing structures have led to the same qualitative results. Guided by our computational models, we view the triplet state as having a π,π^* topology and, like the singlet, possessing significant charge-transfer character. These conclusions are supported by the electrostatic potential surface and the spin-density plot of $^3\mathbf{12a}'$ shown in Figure 10.

That $^3\mathbf{12}$ contains substantial π,π^* character is evidenced by the lack of spin density on the oxygen n-orbitals in $^3\mathbf{12a}'$. Also shown in Figure 10, the parent compound, benzoquinone ($^3\mathbf{BQ}$), is predicted (and known) to possess an n,π^* triplet state⁴⁹, demonstrated by significant spin density on the oxygen n-orbitals orthogonal to the π -system. That $^3\mathbf{12a}'$ lacks spin density on these orbitals suggests that they are doubly occupied, consistent with a π,π^* state. Also evident for $^3\mathbf{12a}'$ is a high degree of conjugation between the sulfur lone-pair and the benzoquinone π -system, indicated by the planar geometry of the

optimized structure and the substantial spin-density on sulfur. Considering the electrostatic potential surface of ${}^3\mathbf{12a}'$, we see accumulation of negative charge on the quinone oxygens and positive charge on the sulfide. In comparison to the benzoquinone triplet, the degree of polarization in ${}^3\mathbf{12a}'$ is substantial. Together, these calculations strongly support the assignment of the triplet in Figure 9 as the charge-transfer structure, ${}^3\mathbf{12}$.

Generation of the zwitterion, $\mathbf{11}$, from ${}^3\mathbf{12}$ requires the additional transfer of a proton and electron from the sulfide to the quinone. As shown in Scheme 2, we expect this to occur through either a sequential (PT-ET) or concerted (HAT) process, where the sequential process involves formation of the intermediate, ${}^3\mathbf{13}$. However, since formation of ${}^3\mathbf{13}$ from ${}^3\mathbf{12}$ occurs much more slowly ($k_{rxn}^T < 1 \times 10^7 \text{ s}^{-1}$, Table 1) than the conversion of ${}^3\mathbf{13}$ to $\mathbf{11}$ ($\sim 10^{11} \text{ s}^{-1}$), established by the radical clock substrate, $\mathbf{4m}$, any possible buildup ${}^3\mathbf{13}$ through the sequential pathway can be discounted. The formation of biradicals such as ${}^3\mathbf{13}$, e.g. in the Norrish II reaction, is typically mandated by the γ -hydrogen shift being faster than decay of the triplet ketone back to the singlet ground state⁵⁰. However, in this particular system, the rate of reaction from the triplet state is not significantly faster than the rate of decay to the ground state, as evidenced by quantum efficiencies for product formation from the triplet (Φ_{rxn}^T) of less than unity. It is thus more conceivable that the biradical intermediate ${}^3\mathbf{13}$ may be bypassed more readily for this system than in a Norrish II reaction. Additionally, if ${}^3\mathbf{13}$ is formed in the conversion of ${}^3\mathbf{12} \rightarrow \mathbf{11}$, its necessarily fleeting existence suggests that it could be more accurately considered to be a reactive intermediate or transition state structure rather than a stable species. The relevant issue is to determine to what extent the transition state in ${}^3\mathbf{12} \rightarrow \mathbf{11}$ resembles ${}^3\mathbf{13}$.

Shown in Figure 10 are the electrostatic potential surface and spin-density plot for the geometry optimized structure of ${}^3\mathbf{13a}'$. In comparison to ${}^3\mathbf{12a}'$, the positive charge in the electrostatic potential surface has been neutralized on the sulfide radical cation, and the semiquinone has developed localized positive charge on the transferred proton. Comparison of the electrostatic potential surface and spin-density of ${}^3\mathbf{13a}'$ with those of the protonated form of the benzoquinone semiquinone (Figure 10, $\mathbf{BQ-H\bullet}$) reveal a close resemblance, suggesting that the twisted α -thio radical in ${}^3\mathbf{13a}'$ does not significantly perturb the electronics of the semiquinone. These findings suggest that the hydrogen-shift process in

${}^3\mathbf{12} \rightarrow {}^3\mathbf{13}$ involves protonation of the semiquinone anion n-orbital with concomitant electron transfer to the sulfur radical cation. Also shown in Figure 10 is the electrostatic potential surface for the ground state of the zwitterion product, $\mathbf{11a}'$. The primary feature of this structure is the redevelopment of positive charge on the substituent as a result of thiocarbenium ion formation. Stabilization of the thiocarbenium ion in $\mathbf{11}$ and the radical in ${}^3\mathbf{13}$ by the sulfur clearly requires p-orbital overlap, since the structures for $\mathbf{11a}'$ and ${}^3\mathbf{13a}'$ minimize with a planar sp^2 -hybridized β -carbon and a shortened C-S bond. However, if it can be assumed that a six-membered transition state is required for the hydrogen-shift to occur, then the degree of stabilization by the sulfur lone pair in the transition state is expected to be significantly less than in $\mathbf{11}$ and ${}^3\mathbf{13}$ due to minimal p-orbital overlap in the planar conformation (${}^3\mathbf{12}$ in Figure 9). Therefore, stabilization of the developing radical in ${}^3\mathbf{13}$ or carbenium ion in $\mathbf{11}$ is expected to be much more sensitive to other substituents on the β -carbon. Comparison of the rate constants of reaction from the triplet state (k_{rxn}^T) for compounds $\mathbf{4a}$ and $\mathbf{4e}$ reveal that the benzyl group is substantially more capable of stabilizing the transition state than the methyl substituent, a trend that reflects both radical and cation stabilities. Shown in Figure 10 are the electrostatic potential surface and spin-density plot for the benzylic products $\mathbf{11e}'$ and ${}^3\mathbf{13e}'$, respectively. In both cases, substantial stabilization by the benzyl group is apparent. For the α -thio radical (${}^3\mathbf{13e}'$), substantial spin-density can be seen on the ortho and para positions of the aromatic ring. For the thiocarbenium ion ($\mathbf{11e}'$), positive electrostatic potential is evenly spread across the benzene hydrogens, and less positive potential appears on the β -carbon than in $\mathbf{11a}'$. These findings support the assumption that the stabilizing effect of sulfur is less important at the transition state geometry for the triplet hydrogen-shift reaction of $\mathbf{4e}$ than it is for $\mathbf{4a}$.

The key difference between $\mathbf{11}$ and ${}^3\mathbf{13}$ when considering the electrostatics of the concerted (${}^3\mathbf{12} \rightarrow \mathbf{11}$) and stepwise (${}^3\mathbf{12} \rightarrow {}^3\mathbf{13} \rightarrow \mathbf{11}$) pathways, is the difference in the amount of positive charge on the substituent. The zwitterion $\mathbf{11a}'$ appears to have more positive electrostatic potential on the β -carbon than ${}^3\mathbf{12a}'$, while ${}^3\mathbf{13a}'$ has substantially less than ${}^3\mathbf{12a}'$, reflecting the fact that the thiocarbenium ion has one less electron than the α -thio radical. Likewise, the transition state structures for the stepwise and concerted processes are

expected to partially decrease and increase, respectively, the amount of positive charge on the carbon. For the benzylic substituents, a large decrease in the rate constant (k_{rxn}^T) was observed for the p-methoxy-benzyl derivative, **4f**, suggesting there to be a diminution of positive charge on the β -carbon at the transition state. These results would not be consistent with the concerted mechanism, where the developing positive charge would be stabilized by the p-methoxy group. We conclude that for the benzylic substrate, the most plausible mechanism is the stepwise process, with the second step (${}^3\mathbf{13} \rightarrow \mathbf{11}$) being extremely rapid and efficient, and the proton transfer step (${}^3\mathbf{12} \rightarrow {}^3\mathbf{13}$) being rate determining. We also note that substituent effects likely manifest themselves in other ways and in other processes, so that the effects on a particular rate constant don't always correlate with effects on the quantum yield⁵¹. For example, although the p-chlorobenzyl substrate (**4g**) has essentially the same rate constant (k_{rxn}^T) as the benzyl substrate (**4e**), it is much more efficient for reaction from the triplet (ϕ_{rxn}^T). This could, perhaps, be due to an inductive effect on the intrinsic rate of triplet decay, with the p-chlorobenzyl substituent resulting in a longer intrinsic lifetime. We previously rationalized that the singlet excited state must be decaying much faster than a normal benzoquinone due to charge-transfer from the sulfur. Perhaps a similar effect governs deactivation of the triplet. Such an effect is expected to be sensitive to inductively withdrawing groups on the sulfur substituent.

The large KIE for hydrogen-shift from the triplet state for **4a**, given by a k_H/k_D of 70, is strongly suggestive that a tunneling mechanism is at least partially active. Although it has been rationalized that a degree of non-planarity in the six-membered transition state would allow favorable stabilization by the lone-pair electrons on sulfur, such an effect would disfavor a tunneling mechanism by increasing the barrier width through which the hydrogen must transfer. Given these competing factors, it is possible that the reaction proceeds through multiple mechanisms, and further experimentation would be required to establish the extent to which each of these mechanisms are active. Nonetheless, tunneling has been observed in similar triplet hydrogen-shift reactions, such as in the photoenolization of ortho-methylanthrone, which results in the formation of products that are isoelectronic with zwitterion **11**⁵² at the relevant positions. Since both of these photoreactions generate a product that contains a newly formed double bond with the β -carbon that has undergone

hydrogen-shift, it is conceivable that the tunneling process is directly associated with double bond formation.

5. CONCLUSIONS

We describe mechanistic studies of a new method that allows rapid photochemical decaging of a wide range of structures using the well-established trimethyl lock lactonization process. Key to the development of this system was the discovery of a highly efficient phototrigger based on an intramolecular redox reaction of an excited benzoquinone bearing a sulfide substituent. Our results indicate that the process begins with photoinduced electron transfer followed by a critical and irreversible hydrogen shift that effectively results in two electron reduction to form the hydroquinone. The nucleophilic hydroquinone oxygen is then capable of undergoing trimethyl-lock cyclization with release of the caged compound.

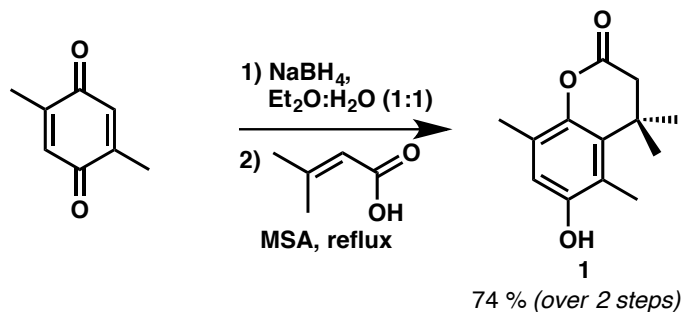
Given our mechanistic conclusions, many strategies for extending the excitation wavelength can be envisioned, as photoinduced electron transfer is a heavily studied and well-understood process. Also, the modular synthesis of these compounds allows the substituent on sulfur to be readily varied, allowing the introduction of groups that impact solubility, cell permeability, and biodistribution in general. Further studies along these lines are underway.

6. EXPERIMENTAL

6.1 *Materials and Methods*

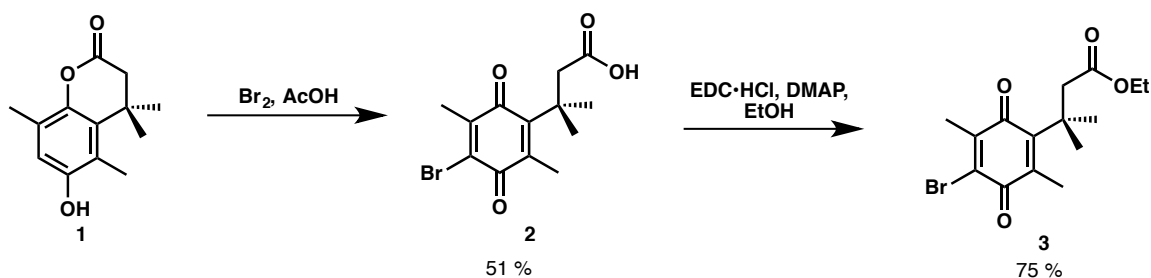
Unless otherwise stated, reactions were performed under an argon atmosphere. All commercially obtained reagents and solvents were used as received unless specifically indicated. All reactions were monitored by thin-layer chromatography using EMD/Merck silica gel 60 F254 pre-coated plates (0.25 mm). Protection of certain materials from light was accomplished by wrapping the reaction, workup, and chromatography glassware with foil or working in conditions of low-ambient light. Experimental details regarding quantum yield measurements are described in section 6.4

6.2 Preparative Procedures and Spectroscopic Data



6-hydroxy-4,4,5,8-tetramethyl-3,4-dihydro-2H-1-benzopyran-2-one (1). To a round bottom flask with magnetic stir bar is added 2,5-dimethylbenzoquinone (1 eq, 586 mg), methanol (20 mL), and diethyl ether (20 mL). An aqueous solution of sodium borohydride (5 eq in 20 mL) is added dropwise. The reaction is stirred 20 minutes under argon, then diluted with water (100 mL), and extracted with diethyl ether (100 mL x 3). The combined organics are dried over MgSO_4 , and concentrated *in vacuo* to yield the crude hydroquinone, which is used in the next step without further purification.

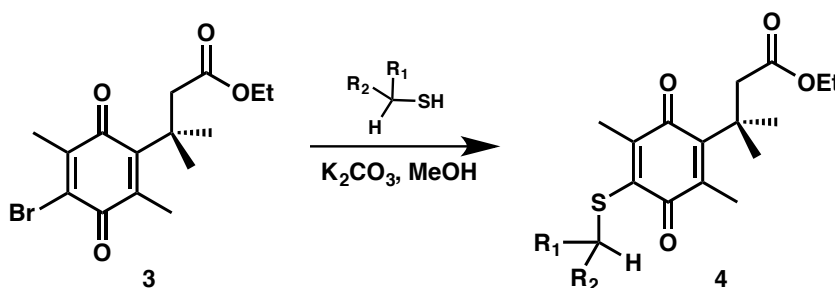
In a round bottom flask with magnetic stir bar and reflux condenser, the crude hydroquinone (1 eq, 441 mg) and 3,3-dimethylacrylic acid (1.1 eq) are suspended in methanesulfonic acid (13 mL) and heated to 70°C under an argon atmosphere overnight. After cooling to room temperature, the mixture is poured into ice water (100 mL) and extracted with ethyl acetate (100 mL x 3). The combined organics are dried over MgSO_4 and concentrated *in vacuo* to yield 700 mg of **1** as a white solid, which is used in the next step without further purification. $^1\text{H NMR}$ (300 MHz, Chloroform-*d*) δ 6.56 (s, 1H), 2.56 (s, 2H), 2.32 (s, 3H), 2.22 (s, 3H), 1.45 (s, 6H).



ethyl 3-(4-bromo-2,5-dimethyl-3,6-dioxocyclohexa-1,4-dien-1-yl)-3-methylbutanoate (3). To a round bottom flask equipped with a magnetic stir bar and addition funnel is added

1 (1 eq, 700 mg) and acetic acid (30 mL). A solution of bromine (2.2 eq) in acetic acid (4 mL) is added dropwise and the reaction is stirred at room temperature overnight. Upon completion, the mixture is diluted with water (150 mL) and extracted with dichloromethane (150 mL x 3). The combined organics are transferred to an Erlenmeyer flask with stir bar and brought to pH = 7 with the slow addition of dilute aqueous sodium hydroxide. The mixture is then extracted with sat. aq. sodium bicarbonate (150 mL x 5) (warning: gas evolution). The combined aqueous extracts are made acidic (pH < 4) with the addition of 1M HCl, and extracted with EtOAc (150 mL x 3). The combined organics are dried over MgSO₄ and concentrated *in vacuo* to provide 518 mg of **2** as a light yellow solid that is used in the next step without further purification.

To a 20 mL vial equipped with stir bar and protected from light is added **2** (1 eq, 518 mg), EDC•HCl (1 eq), and DMAP (0.1 eq). To the vial is then added simultaneously ethanol (20 eq), and dichloromethane (8 mL). After stirring 15 minutes, the mixture is diluted in water (25 mL) and extracted with dichloromethane (25 mL x 3). The combined organics are dried over MgSO₄ and concentrated *in vacuo*. The crude product is purified by flash column chromatography (SiO₂, 0 – 10% EtOAc in hexanes) to yield 430 mg of **3** as a yellow oil. ¹H NMR (300 MHz, Chloroform-*d*) δ 4.03 (q, *J* = 7.1 Hz, 2H), 2.93 (s, 2H), 2.19 (s, 3H), 2.16 (s, 3H), 1.42 (s, 6H), 1.18 (t, *J* = 7.2 Hz, 3H).



Preparation of sulfide-substituted benzoquinones (**4**).

General Procedure A: In a 20 mL vial equipped with a magnetic stir bar and protected from light is dissolved **3** (1 eq, 0.1 M) and methanol. To this solution is then sequentially added the thiol (2 eq) and K₂CO₃ (2 eq). The reaction is stirred until starting material is completely consumed as determined by TLC or LCMS (~ 15 mins), then diluted in water

and extracted with hexanes (x 3). The combined organics are dried over MgSO₄, and concentrated *in vacuo*. The crude is purified by flash column chromatography (SiO₂, 0 – 5% EtOAc in hexanes) to yield **4** as a yellow solid or oil in generally high yields.

General Procedure B: In a 20 mL vial equipped with a magnetic stir bar and protected from light is dissolved **3** (1 eq, 0.1M) in 1:1 dichloromethane : water. To the biphasic mixture is added tetrabutylammonium bromide (0.05 eq) and either the thiol (2 eq) and K₂CO₃ (2 eq) or the sodium salt of the thiolate (2 eq). The solution is stirred or shaken vigorously for 5 minutes, then diluted in water and extracted with dichloromethane (x 3). The combined organics are dried over MgSO₄ and concentrated *in vacuo*. The crude is purified by flash column chromatography (SiO₂, 0 – 5% EtOAc in hexanes) to yield **4** as a yellow solid or oil in generally high yields.

ethyl 3-[2,5-dimethyl-4-(methylsulfanyl)-3,6-dioxocyclohexa-1,4-dien-1-yl]-3-methylbutanoate (4a). Prepared according to *General Procedure B*. ¹H NMR (300 MHz, Chloroform-*d*) δ 4.03 (q, *J* = 7.1 Hz, 2H), 2.95 (s, 2H), 2.47 (s, 2H), 2.16 (s, 3H), 2.13 (s, 2H), 1.42 (s, 6H), 1.19 (t, *J* = 7.1 Hz, 2H). ESI-MS(+) calculated for [C₁₆H₂₂NaO₄S]⁺ ([M+23]⁺) 333.1, found 333.0.

ethyl 3-{2,5-dimethyl-4-[(²H₃)methylsulfanyl]-3,6-dioxocyclohexa-1,4-dien-1-yl}-3-methylbutanoate (4a-d₃). Prepared according to *General Procedure B*. ¹H NMR (600 MHz, Chloroform-*d*) δ 4.03 (q, *J* = 7.1 Hz, 2H), 2.94 (s, 2H), 2.16 (s, 3H), 2.12 (s, 3H), 1.42 (s, 6H), 1.19 (t, *J* = 7.1 Hz, 3H). ESI-MS(+) calculated for [C₁₆H₁₉D₃NaO₄S]⁺ ([M+23]⁺) 336.1, found 336.0.

ethyl 3-[4-(ethylsulfanyl)-2,5-dimethyl-3,6-dioxocyclohexa-1,4-dien-1-yl]-3-methylbutanoate (4b). Prepared according to *General Procedure A*. ¹H NMR (600 MHz, Chloroform-*d*) δ 4.02 (q, *J* = 7.1 Hz, 2H), 3.00 (d, *J* = 7.5 Hz, 2H), 2.94 (s, 2H), 2.16 (s, 3H), 2.14 (s, 3H), 1.42 (s, 6H), 1.23 (d, *J* = 7.4 Hz, 3H), 1.18 (t, *J* = 7.1 Hz, 3H). ESI-MS(+) calculated for [C₁₇H₂₄NaO₄S]⁺ ([M+23]⁺) 347.1, found 347.0.

ethyl 3-[2,5-dimethyl-3,6-dioxo-4-(propan-2-ylsulfanyl)cyclohexa-1,4-dien-1-yl]-3-methylbutanoate (4c). Prepared according to *General Procedure A*. ^1H NMR (600 MHz, Chloroform-*d*) δ 4.02 (q, $J = 6.9$ Hz, 2H), 3.76 (q, $J = 7.2$ Hz, 1H), 2.93 (s, 2H), 2.17 (s, 3H), 2.16 (s, 3H), 1.43 (s, 6H), 1.17 (t, $J = 7.2$ Hz, 3H). ESI-MS(+) calculated for $[\text{C}_{18}\text{H}_{26}\text{NaO}_4\text{S}]^+$ ($[\text{M}+23]^+$) 361.1, found 361.1.

ethyl 3-[4-(tert-butylsulfanyl)-2,5-dimethyl-3,6-dioxocyclohexa-1,4-dien-1-yl]-3-methylbutanoate (4d). Prepared according to *General Procedure A*. ^1H NMR (600 MHz, Chloroform-*d*) δ 4.06 – 3.97 (m, 1H), 2.92 (s, 2H), 2.28 (s, 3H), 2.19 (s, 3H), 1.43 (s, 6H), 1.32 (s, 9H), 1.18 (t, $J = 7.1$ Hz, 3H).

ethyl 3-[4-(benzylsulfanyl)-2,5-dimethyl-3,6-dioxocyclohexa-1,4-dien-1-yl]-3-methylbutanoate (4e). Prepared according to *General Procedure A*. Prepared according to *General Procedure A*. ^1H NMR (300 MHz, Chloroform-*d*) δ 7.36 – 7.14 (m, 5H), 4.18 (s, 2H), 3.98 (q, $J = 7.1$ Hz, 2H), 2.90 (s, 2H), 2.16 (s, 3H), 2.00 (s, 3H), 1.40 (s, 6H), 1.14 (t, $J = 7.1$ Hz, 3H). ESI-MS(+) calculated for $[\text{C}_{22}\text{H}_{26}\text{NaO}_4\text{S}]^+$ ($[\text{M}+23]^+$) 409.1, found 409.1.

ethyl 3-(2,5-dimethyl-3,6-dioxo-4-{{phenyl($^2\text{H}_2$)methyl}sulfanyl}cyclohexa-1,4-dien-1-yl)-3-methylbutanoate (4e- d_2). Prepared according to *General Procedure A*. ^1H NMR (300 MHz, Chloroform-*d*) δ 7.34 – 7.16 (m, 5H), 3.98 (q, $J = 7.1$ Hz, 2H), 2.90 (s, 2H), 2.16 (s, 3H), 2.00 (s, 3H), 1.40 (s, 6H), 1.14 (t, $J = 7.1$ Hz, 3H). ESI-MS(+) calculated for $[\text{C}_{22}\text{H}_{24}\text{D}_2\text{NaO}_4\text{S}]^+$ ($[\text{M}+23]^+$) 411.1, found 411.1.

ethyl 3-(4-{{(4-methoxyphenyl)methyl}sulfanyl}-2,5-dimethyl-3,6-dioxocyclohexa-1,4-dien-1-yl)-3-methylbutanoate (4f). Prepared according to *General Procedure A*. ^1H NMR (300 MHz, Chloroform-*d*) δ 7.17 (d, $J = 8.6$ Hz, 2H), 6.80 (d, $J = 8.6$ Hz, 2H), 4.15 (s, 2H), 3.99 (q, $J = 7.1$ Hz, 2H), 3.77 (s, 3H), 2.91 (s, 2H), 2.16 (s, 3H), 2.02 (s, 3H), 1.41

(s, 6H), 1.19 – 1.10 (m, 3H). ESI-MS(+) calculated for $[\text{C}_{23}\text{H}_{28}\text{NaO}_5\text{S}]^+$ ($[\text{M}+23]^+$) 439.1, found 439.1.

ethyl 3-(4-[(4-chlorophenyl)methyl]sulfanyl)-2,5-dimethyl-3,6-dioxocyclohexa-1,4-dien-1-yl)-3-methylbutanoate (4g). Prepared according to *General Procedure A*. ^1H NMR (300 MHz, Chloroform-*d*) δ 7.24 – 7.14 (m, 4H), 4.13 (s, 2H), 4.00 (q, $J = 7.2$ Hz, 2H), 2.90 (s, 2H), 2.15 (s, 3H), 2.01 (s, 3H), 1.40 (s, 6H), 1.16 (t, $J = 7.1$ Hz, 3H). ESI-MS(+) calculated for $[\text{C}_{22}\text{H}_{25}\text{ClNaO}_4\text{S}]^+$ ($[\text{M}+23]^+$) 443.1, found 443.1.

ethyl 3-(2,5-dimethyl-4-[(4-nitrophenyl)methyl]sulfanyl)-3,6-dioxocyclohexa-1,4-dien-1-yl)-3-methylbutanoate (4h). Prepared according to *General Procedure A*. ^1H NMR (300 MHz, Chloroform-*d*) δ 8.14 (d, $J = 8.4$ Hz, 2H), 7.38 (d, $J = 8.5$ Hz, 2H), 4.20 (s, 2H), 3.99 (q, $J = 6.9$ Hz, 2H), 2.88 (s, 2H), 2.15 (s, 3H), 1.98 (s, 3H), 1.38 (s, 6H), 1.17 (t, $J = 7.2$ Hz, 3H). ESI-MS(+) calculated for $[\text{C}_{22}\text{H}_{25}\text{NNaO}_6\text{S}]^+$ ($[\text{M}+23]^+$) 454.1, found 454.1.

ethyl 3-{4-[(2-methoxy-2-oxoethyl)sulfanyl]-2,5-dimethyl-3,6-dioxocyclohexa-1,4-dien-1-yl}-3-methylbutanoate (4i). Prepared according to *General Procedure A*. ^1H NMR (600 MHz, Chloroform-*d*) δ 4.02 (q, $J = 7.4$ Hz, 2H), 3.73 (s, 2H), 3.70 (s, 3H), 2.92 (s, 2H), 2.15 (s, 6H), 1.42 (q, $J = 7.6$ Hz, 6H), 1.18 (t, $J = 7.0$ Hz, 3H). ESI-MS(+) calculated for $[\text{C}_{18}\text{H}_{24}\text{NaO}_6\text{S}]^+$ ($[\text{M}+23]^+$) 391.1, found 391.0.

ethyl 3-{4-[(4-hydroxybutyl)sulfanyl]-2,5-dimethyl-3,6-dioxocyclohexa-1,4-dien-1-yl}-3-methylbutanoate (4j). Prepared according to *General Procedure A*. ^1H NMR (300 MHz, Chloroform-*d*) δ 4.02 (q, $J = 7.2$ Hz, 2H), 3.68 – 3.58 (m, 2H), 3.05 – 2.96 (m, 2H), 2.94 (s, 2H), 2.17 (s, 3H), 2.15 (s, 3H), 1.70 – 1.62 (m, 4H), 1.42 (s, 6H), 1.19 (t, $J = 7.1$ Hz, 3H). ESI-MS(+) calculated for $[\text{C}_{19}\text{H}_{28}\text{NaO}_5\text{S}]^+$ ($[\text{M}+23]^+$) 391.1, found 391.1.

ethyl 3-[4-(hex-5-en-1-ylsulfanyl)-2,5-dimethyl-3,6-dioxocyclohexa-1,4-dien-1-yl]-3-methylbutanoate (4k). Prepared according to *General Procedure A*. ^1H NMR (300

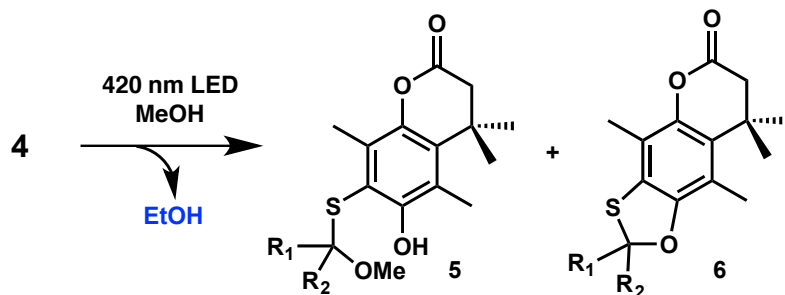
MHz, Chloroform-*d*) δ 5.85 – 5.69 (m, 3H), 5.04 – 4.89 (m, 2H), 4.02 (q, $J = 7.1$ Hz, 2H), 3.02 – 2.90 (m, 4H), 2.16 (s, 3H), 2.14 (s, 3H), 2.10 – 1.98 (m, 2H), 1.63 – 1.43 (m, 4H), 1.42 (s, 6H), 1.18 (t, $J = 7.1$ Hz, 3H). ESI-MS(+) calculated for $[\text{C}_{21}\text{H}_{30}\text{NaO}_4\text{S}]^+$ ($[\text{M}+23]^+$) 401.1, found 401.2.

ethyl 3-{4-[(cyclopropylmethyl)sulfanyl]-2,5-dimethyl-3,6-dioxocyclohexa-1,4-dien-1-yl}-3-methylbutanoate (4l). Prepared according to *General Procedure A*. ^1H NMR (300 MHz, Chloroform-*d*) δ 3.99 (q, $J = 7.1$ Hz, 1H), 2.91 (s, 2H), 2.88 (d, $J = 7.3$ Hz, 2H), 2.14 (s, 6H), 1.40 (s, 6H), 1.15 (t, $J = 7.2$ Hz, 3H), 1.04 – 0.82 (m, 1H), 0.64 – 0.38 (m, 2H), 0.24 – 0.11 (m, 2H). ESI-MS(+) calculated for $[\text{C}_{19}\text{H}_{26}\text{NaO}_4\text{S}]^+$ ($[\text{M}+23]^+$) 373.1, found 373.1.

ethyl 3-[2,5-dimethyl-3,6-dioxo-4-({(1R,2R)-2-phenylcyclopropyl)methyl}sulfanyl]cyclohexa-1,4-dien-1-yl]-3-methylbutanoate (4m). Prepared according to *General Procedure A*. ^1H NMR (400 MHz, Chloroform-*d*) δ 7.22 (dd, $J = 7.7, 7.2$ Hz, 2H), 7.14 (t, $J = 7.2$ Hz, 1H), 7.02 (d, $J = 7.7$ Hz, 2H), 4.01 (q, $J = 7.0$ Hz, 2H), 3.21 – 3.00 (m, 2H), 2.93 (q, $J = 16.1$ Hz, 2H), 2.16 (s, 3H), 2.13 (s, 3H), 1.89 – 1.69 (m, 1H), 1.42 (d, $J = 3.5$ Hz, 6H), 1.36 – 1.23 (m, 1H), 1.18 (t, $J = 7.0$ Hz, 3H), 1.09 – 0.96 (m, 1H), 0.95 – 0.84 (m, 1H). ESI-MS(+) calculated for $[\text{C}_{25}\text{H}_{30}\text{NaO}_4\text{S}]^+$ ($[\text{M}+23]^+$) 449.1, found 449.2.

ethyl 3-{2,5-dimethyl-3,6-dioxo-4-[(1-phenylethyl)sulfanyl]cyclohexa-1,4-dien-1-yl}-3-methylbutanoate (4n). Prepared according to *General Procedure A*. ^1H NMR (300 MHz, Chloroform-*d*) δ 7.24 – 7.13 (m, 5H), 4.79 (q, $J = 7.1$ Hz, 1H), 4.04 – 3.87 (m, 2H), 2.86 (s, 2H), 2.11 (s, 3H), 2.01 (s, 3H), 1.61 (d, $J = 7.0$ Hz, 3H), 1.37 (d, $J = 9.8$ Hz, 6H), 1.13 (t, $J = 7.1$ Hz, 3H). ESI-MS(+) calculated for $[\text{C}_{23}\text{H}_{28}\text{NaO}_4\text{S}]^+$ ($[\text{M}+23]^+$) 423.1, found 423.0.

6.3 Preparative-Scale Photolysis



In a 20 mL vial equipped with a magnetic stir bar is dissolved **4** (10-15 mg) in air-equilibrated methanol (20 mL). The solution is irradiated with focused light from a 420 nm LED until the starting material is completely consumed (~ 1 hour) determined by visible photobleaching. The sample then is concentrated *in vacuo* to yield **5**, **6**, or **7** as the exclusive photoproduct, unless otherwise stated. If a mixture is obtained, the crude is purified by flash column chromatography (SiO₂, 10% EtOAc in hexanes) to yield the isolated products. In some cases, **5** could not be isolated due to decomposition, and the reported NMR spectral data are derived from the crude NMR spectrum. All reported yields are based on integration of the crude NMR spectrum.

6-hydroxy-7-[(6-hydroxy-4,4,5,8-tetramethyl-2-oxo-3,4-dihydro-2H-1-benzopyran-7-yl)disulfanyl]-4,4,5,8-tetramethyl-3,4-dihydro-2H-1-benzopyran-2-one (7). ¹H NMR (300 MHz, Chloroform-*d*) δ 6.46 (s, 2H), 2.56 (s, 4H), 2.31 (s, 6H), 2.13 (s, 6H), 1.47 (s, 12H).

Photolysis of **4a** produces **5a** (>90%). **6-hydroxy-7-[(methoxymethyl)sulfanyl]-4,4,5,8-tetramethyl-3,4-dihydro-2H-1-benzopyran-2-one (5a)**. ¹H NMR (400 MHz, Chloroform-*d*) δ 7.17 (s, 1H), 4.69 (s, 2H), 3.48 (s, 3H), 2.55 (s, 2H), 2.50 – 2.42 (m, 3H), 2.41 – 2.35 (m, 3H), 1.46 (s, 6H).

Photolysis of **4c** produces **5c** (50%) and **7** (50%). **6-hydroxy-7-[(2-methoxypropan-2-yl)sulfanyl]-4,4,5,8-tetramethyl-3,4-dihydro-2H-1-benzopyran-2-one (5c)**. ¹H NMR

(300 MHz, Chloroform-*d*) δ 7.57 (s, 1H), 3.48 (s, 3H), 2.55 (s, 2H), 2.41 (s, 3H), 2.37 (s, 3H), 1.51 (s, 6H), 1.46 (s, 6H).

Photolysis of **4e** produces **5e** (>90%). **6-hydroxy-7-[[methoxy(phenyl)methyl]sulfanyl]-4,4,5,8-tetramethyl-3,4-dihydro-2H-1-benzopyran-2-one (5e)**. ^1H NMR (400 MHz, Chloroform-*d*) δ 7.66 – 7.36 (m, 4H), 7.07 – 6.88 (m, 2H), 5.47 (s, 1H), 3.44 (s, 3H), 2.54 (s, 2H), 2.34 (s, 3H), 2.27 (s, 3H), 1.46 (s, 6H).

Photolysis of **4f** produces **6f** (64%) and **7** (36%). **5-(4-methoxyphenyl)-2,8,13,13-tetramethyl-4,10-dioxo-6-thiatricyclo[7.4.0.0^{3,7}]trideca-1(9),2,7-trien-11-one (6f)**. ^1H NMR (300 MHz, Chloroform-*d*) δ 7.54 (d, $J = 8.7$ Hz, 2H), 7.06 – 6.78 (m, 3H), 3.83 (s, 3H), 2.55 (s, 2H), 2.32 (s, 3H), 2.18 (s, 3H), 1.43 (s, 6H).

Photolysis of **4k** produces **5k** (97%) and **7** (3%). **6-hydroxy-7-[(1-methoxyhex-5-en-1-yl)sulfanyl]-4,4,5,8-tetramethyl-3,4-dihydro-2H-1-benzopyran-2-one (5k)**. ^1H NMR (300 MHz, Chloroform-*d*) δ 7.44 (s, 1H), 5.74 (ddt, $J = 17.0, 10.2, 6.6$ Hz, 1H), 5.03 – 4.90 (m, 2H), 4.48 (dd, $J = 7.5, 5.3$ Hz, 1H), 3.49 (s, 3H), 2.56 (s, 2H), 2.44 (s, 3H), 2.38 (s, 3H), 2.09 – 1.97 (m, 2H), 1.80 – 1.49 (m, 4H), 1.47 (s, 6H).

Photolysis of **4l** produces **5l** (87%), **6l** (10%) and **7** (3%). **7-[[cyclopropyl(methoxy)methyl]sulfanyl]-6-hydroxy-4,4,5,8-tetramethyl-3,4-dihydro-2H-1-benzopyran-2-one (5l)**. ^1H NMR (300 MHz, Chloroform-*d*) δ 7.43 (s, 1H), 3.93 (d, $J = 8.0$ Hz, 1H), 3.50 (s, 3H), 2.55 (s, 2H), 2.47 (s, 3H), 2.38 (s, 3H), 1.46 (s, 6H), 1.19 – 1.01 (m, 1H), 0.71 – 0.43 (m, 3H), 0.43 – 0.30 (m, 1H). **5-cyclopropyl-2,8,13,13-tetramethyl-4,10-dioxo-6-thiatricyclo[7.4.0.0^{3,7}]trideca-1(9),2,7-trien-11-one (6l)**. ^1H NMR (300 MHz, Chloroform-*d*) δ 5.51 (d, $J = 7.8$ Hz, 1H), 2.54 (s, 2H), 2.31 (s, 3H), 2.16 (s, 3H), 1.42 (s, 6H), 0.82 – 0.41 (m, 4H).

Photolysis of **4m** produces the diastereomers **5m** and **5m'** in a 3:2 ratio, along with other

uncharacterized byproducts. Although isolation proved difficult due to decomposition, assignment has been made primarily based on clear ^1H -NMR resonances for cyclopropane -CH, the oxidized methylene -CH, methyl ether -OCH₃, aryl -CH₃, and the lactone methylene -CH₂ protons. **(5m)**. ^1H NMR (400 MHz, Chloroform-*d*) δ 4.41 (d, J = 5.8 Hz, 1H), 3.53 (s, 3H), 2.47 (s, 2H), 2.42 (s, 3H), 2.29 (s, 3H). **(5m')**. ^1H NMR (400 MHz, Chloroform-*d*) δ 4.31 (d, J = 7.0 Hz, 1H), 3.55 (s, 3H), 2.51 (s, 2H), 2.39 (s, 3H), 2.26 (s, 3H).

6.4 Quantum Yield Measurements

Materials and Methods

All chemicals and solvents were purchased in the highest grade available. Spectral grade methanol was distilled prior to use for quantum yield measurements. Thioxanthone was purified by preparative HPLC using a 5-95% acetonitrile-water gradient, and pure fractions were used in sensitization studies. Diethylaniline was distilled under vacuum immediately prior to use. Samples were prepared in eight-inch NMR tubes (Wilmad WG-1000) and photolyzed using 420 nm light from a Thorlabs M420L3 1W LED, 1A driver, and a custom-made merry-go-round apparatus rotating at 20 rpm. All procedures were carried out in darkness with a dim red safety light. Data were collected on an Agilent 1260 HPLC equipped with a diode-array detector using a 60% isocratic acetonitrile-water gradient. Absorbance spectra were recorded on a Cary 60 using 10 mm glass cuvettes.

Preparation of Potassium Ferrioxalate

The following procedure⁴⁴ is taken from *Photochemistry of Organic Compounds* by Klan & Wirz and is performed in a dark room with a red safety light. In an Erlenmeyer flask with magnetic stir bar is mixed 1.5 M potassium oxalate monohydrate (300 mL) and 1.5 M ferric chloride hexahydrate (100 mL). The mixture is stirred 10 minutes then filtered through a Buchner funnel. The collected solid is recrystallized thrice from warm water, then dried over a current of warm air overnight to provide crystalline potassium ferrioxalate trihydrate, which is stored at room temperature in the dark.

General procedure for Ferrioxalate actinometry

Solutions of potassium ferrioxalate and 1,10-phenanthroline are always made fresh when measuring quantum yields. In darkness (or in dim red light, $\lambda > 600$ nm), solid potassium ferrioxalate trihydrate (60 mg) is weighed into a tared 20 mL vial to which is then added 0.05 M H₂SO₄ (20 mL). The mixture is thoroughly shaken to ensure a homogenous solution is formed. Additionally, a solution of 1,10-phenanthroline (40 mg) in 1M sodium acetate buffer (20 mL; prepared by adding 82 g of NaOAc•3H₂O and 10 mL H₂SO₄ to 1 L of water) is prepared, and again thoroughly shaken until the solid is completely dissolved.

Using a 1 mL gas-tight syringe fitted with a four-inch needle, 500 μ L of actinometer solution is transferred to the bottom of an NMR tube and capped. The solution is irradiated at 420 nm in a merry-go-round apparatus. Upon completion, 100 μ L of the photolysate is transferred to a 2 mL volumetric flask (the syringe is initially flushed thrice with a small volume of photolysate). To the volumetric is then added 800 μ L buffered phenanthroline solution and the contents of the flask are diluted with water to the mark. The solution is allowed to develop for 15 minutes, then transferred via pipette to a clean dry cuvette and the UV/Vis spectrum recorded.

General procedures for photolysis quantum yields

Sample preparation for direct photolysis. To an amber HPLC vial is transferred 1 mL of a solution of **4** in methanol initially prepared with a 10 mm absorbance at 420 nm between 0.05 and 0.1. Using a 1 mL gas-tight syringe fitted with a four-inch needle, 500 μ L of the solution is transferred to the bottom of an eight-inch NMR tube, freeze-pump-thawed thrice, then flame-sealed under vacuum. The remaining 500 μ L is capped for HPLC analysis.

Sample preparation for sensitized photolysis. A stock solution of thioxanthone in methanol is initially prepared with a 10 mm absorbance at 420 nm between 0.05 – 0.1 and

a total volume of 10 mL. To 5 mL of this solution is added a calculated amount of **4** such that the 10 mm absorbance of **4** would be 0.1 at 420 nm (determined by HPLC calibration curve). Using a 1 mL gas-tight syringe, samples with different concentrations of **4** are prepared in amber HPLC vials (1 mL total) by mixing the two stock solutions at different ratios (up to a 10x dilution of **4**). Using a 1 mL gas-tight syringe fitted with a four-inch needle, 500 μ L of each solution is transferred to the bottom of an eight-inch NMR tube, freeze-pump-thawed thrice, then flame-sealed under vacuum. The remaining 500 μ L is capped for HPLC analysis. In some cases, the thioxanthone precipitates from the freeze-pump-thawed solution in which case gentle agitation results in dissolution.

Sample preparation for direct photolysis in the presence of quencher. A stock solution of **4** in methanol is initially prepared with a 10 mm absorbance at 420 nm between 0.05 – 0.1 and a total volume of 10 mL. To 5 mL of this solution is added N,N-diethylaniline (80 μ L) to create a second stock solution with a 0.1 M quencher concentration. Using a 1 mL gas-tight syringe, samples with different quencher concentrations (0 – 100 mM) are prepared in amber HPLC vials (1 mL total) by mixing the two stock solutions at different ratios. Using a 1 mL gas-tight syringe fitted with a four-inch needle, 500 μ L of each solution is transferred to the bottom of an eight-inch NMR tube, freeze-pump-thawed thrice, then flame-sealed under vacuum. The remaining 500 μ L is capped for HPLC analysis.

Photolysis. The prepared samples are irradiated in a well-ventilated space using a 420 nm LED and merry-go-round apparatus that spins at approximately 20 rpm. Both components (the LED and merry-go-round) are mounted on an optical rail to ensure consistency in light exposure. In some cases, the intensity of the LED is adjusted such that total photolysis time is at least 5 minutes, which ensures an adequate number of revolutions on the merry-go-round. Upon completion, the NMR tubes are scored near the surface of the liquid, cracked, poured into amber HPLC vials, and capped for analysis.

Data collection. In general, quantitative analysis for the photolysis of **4** was performed by HPLC using an isocratic elution of 60% acetonitrile in water and integration of the peak corresponding to **4** in the 254 nm absorbance trace. Quantitative analysis for photolysis of ferrioxalate was performed by UV/Vis spectroscopy using a glass cuvette (10 mm path length), blanked with water, and by measurement of the absorbance at 510 nm corresponding to the Fe²⁺-phenanthroline complex.

Calculation of the quantum yield. The quantum yield for disappearance of **4** (Φ_4) due to direct photolysis is given by Eq. 1a.

$$\Phi_4 = \frac{n_4}{p_4} \quad (1a)$$

where n_4 is the number of moles of **4** consumed, and p_4 is the number moles of photons absorbed by **4**. n_4 is further given by Eq. 1b, the difference between the number of moles pre- and post-photolysis, which are calculated from the integrations in the HPLC (I_4), the use of a calibration function (f), and the volume of the photolysis sample (V).

$$n_4 = (f(I_4^{pre}) - f(I_4^{post})) \cdot V \quad (1b)$$

The value for p_4 is calculated using Eq. 1c, where $(1 - 10^{-Abs_4})$ represents the fraction of the LED output absorbed by **4**, $(1 - 10^{-Abs_{Fe3+}})$ is that absorbed by potassium ferrioxalate, Φ_{Fe2+} is the quantum yield for Fe²⁺ production (1.115⁴⁴), and n_{Fe2+} is the number of moles of Fe²⁺ produced. The latter is given by the absorbance of the Fe²⁺-phenanthroline complex measured at 510 nm (see general procedure above), the known extinction coefficient (11100 M⁻¹cm⁻¹), and the photolysis volume. The fraction of photons absorbed by **4** is given by a calibration function (g) between $(1 - 10^{-Abs_4})$ and I_4 , which is more convenient than measuring the actual absorbance spectrum of the photolysis solution. For the fraction of photons absorbed by the ferrioxalate solution, the absorbance must be measured directly before and after photolysis.

$$p_4 = \frac{(1-10^{-Abs_4})}{(1-10^{-Abs_{Fe3+}})} \cdot \frac{\Phi_{Fe2+}}{n_{Fe2+}} = \frac{g(I_4)}{(1-10^{-Abs_{Fe3+}})} \cdot \frac{\Phi_{Fe2+}}{n_{Fe2+}} \quad (1c)$$

For calculation of the sensitized quantum yield, $(1 - 10^{-Abs_4})$ is replaced with the fraction of photons absorbed by the sensitizer, which is again given by a calibration function between the integration of the thioxanthone peak in the HPLC trace and its UV/Vis

absorption spectrum. In some cases, a small amount of direct photolysis occurs during sensitization experiments. To correct for this, the amount of **4** consumed (n_4) due to direct photolysis is subtracted from the total using the known quantum yield (Φ_4) before calculation of the sensitized quantum yield is performed. In most cases, this amounted to less than 10% of the total consumption of **4**.

7. REFERENCES

1. Walton, D., Regan, C. & Dougherty, D. A strategy for long-wavelength decaging of bioactive molecules. *Manuscript in Progress*.
2. Levine, M. N. & Raines, R. T. Trimethyl lock: A trigger for molecular release in chemistry, biology, and pharmacology. *Chem. Sci. R. Soc. Chem.* **2010** **3**, 2412–2420 (2012).
3. Greenwald, R. B. *et al.* Drug Delivery Systems Based on Trimethyl Lock Lactonization: Poly(ethylene glycol) Prodrugs of Amino-Containing Compounds. *J. Med. Chem.* **43**, 475–487 (2000).
4. Gomes, P., Vale, N. & Moreira, R. Cyclization-activated prodrugs. *Mol. Basel Switz.* **12**, 2484–2506 (2007).
5. Klán, P. *et al.* Photoremovable Protecting Groups in Chemistry and Biology: Reaction Mechanisms and Efficacy. *Chem. Rev.* **113**, 119–191 (2013).
6. Pelliccioli, A. P. & Wirz, J. Photoremovable protecting groups: reaction mechanisms and applications. *Photochem. Photobiol. Sci.* **1**, 441–458 (2002).
7. Gorner, H. Photoreactions of p-quinones with dimethyl sulfide and dimethyl sulfoxide in aqueous acetonitrile. *Photochem. Photobiol.* **82**, 71–77 (2006).
8. Kavarnos, G. J. & Turro, N. J. Photosensitization by reversible electron transfer: theories, experimental evidence, and examples. *Chem. Rev.* **86**, 401–449 (1986).
9. Görner, H. Photoreduction of p-Benzoquinones: Effects of Alcohols and Amines on the Intermediates and Reactivities in Solution. *Photochem. Photobiol.* **78**, 440–448 (2003).
10. Scheerer, R. & Graetzel, M. Laser photolysis studies of duroquinone triplet state electron transfer reactions. *J. Am. Chem. Soc.* **99**, 865–871 (1977).

11. Baxter, I. & Phillips, W. R. Reactions between 2,5-di-*t*-butyl-1,4-benzoquinone and certain primary aliphatic amines. *J. Chem. Soc. [Perkin 1]* 268–272 (1973). doi:10.1039/P19730000268
12. Bruce, J. M. Light-induced reactions of quinones. *Q. Rev. Chem. Soc.* **21**, 405–428 (1967).
13. Iwamoto, H., Takuwa, A., Hamada, K. & Fujiwara, R. Intra- and intermolecular photocyclization of vinylbenzo-1,4-quinones. *J. Chem. Soc. [Perkin 1]* 575–582 (1999). doi:10.1039/A809530B
14. Kallmayer, H.-J. & Fritzen, W. Photoreaktivität einiger 2-Alkylthio/Phenylthio-3,5,6-trichlor/brom-1,4-benzochinone. *Pharmazie* **49**, 412–415 (1994).
15. Shi, M., Yang, W.-G. & Wu, S. Wavelength-dependent photolyses of 2,5-dichloro-3,6-bis(dialkylamino)-[1,4]benzoquinone. *J. Photochem. Photobiol. Chem.* **185**, 140–143 (2007).
16. Chen, Y. & Steinmetz, M. G. Photoactivation of Amino-Substituted 1,4-Benzoquinones for Release of Carboxylate and Phenolate Leaving Groups Using Visible Light. *J. Org. Chem.* **71**, 6053–6060 (2006).
17. Chen, Y. & Steinmetz, M. G. Photochemical Cyclization with Release of Carboxylic Acids and Phenol from Pyrrolidino-Substituted 1,4-Benzoquinones Using Visible Light. *Org. Lett.* **7**, 3729–3732 (2005).
18. Jones & Qian, X. Photochemistry of Quinone-Bridged Amino Acids. Intramolecular Trapping of an Excited Charge-Transfer State I. *J. Phys. Chem. A* **102**, 2555–2560 (1998).
19. Falci, K. J., Franck, R. W. & Smith, G. P. Approaches to the mitomycins. Photochemistry of aminoquinones. *J. Org. Chem.* **42**, 3317–3319 (1977).
20. Giles, R. G. F. The photochemistry of an aminated 1,4-benzoquinone. *Tetrahedron Lett.* **13**, 2253–2254 (1972).
21. Cameron, D. W. & Giles, R. G. F. Photochemical formation of benzoxazoline derivatives from aminated quinones. *J. Chem. Soc. C Org.* 1461–1464 (1968). doi:10.1039/J39680001461
22. Cameron, D. W. & Giles, R. G. F. A photochemical rearrangement involving aminated quinones. *Chem. Commun. Lond.* 573–574 (1965). doi:10.1039/C19650000573

23. Barbafina, A., Latterini, L., Carlotti, B. & Elisei, F. Characterization of Excited States of Quinones and Identification of Their Deactivation Pathways. *J. Phys. Chem. A* **114**, 5980–5984 (2010).
24. Hubig, S. M., Bockman, T. M. & Kochi, J. K. Identification of Photoexcited Singlet Quinones and Their Ultrafast Electron-Transfer vs Intersystem-Crossing Rates. *J. Am. Chem. Soc.* **119**, 2926–2935 (1997).
25. Trommsdorff, H. P. Electronic States and Spectra of p-Benzoquinone. *J. Chem. Phys.* **56**, 5358–5372 (1972).
26. Asundi, R. K. & Singh, R. S. Absorption Spectrum of Benzoquinone. *Nature* **176**, 1223–1224 (1955).
27. Bridge, N. K. & Porter, G. Primary Photoprocesses in Quinones and Dyes. I. Spectroscopic Detection of Intermediates. *Proc. R. Soc. Lond. Math. Phys. Eng. Sci.* **244**, 259–275 (1958).
28. Bridge, N. K. & Porter, G. Primary Photoprocesses in Quinones and Dyes. II. Kinetic Studies. *Proc. R. Soc. Lond. Math. Phys. Eng. Sci.* **244**, 276–288 (1958).
29. Orgel, L. E. The electronic structures and spectra of p-benzoquinone and its derivatives. *Trans. Faraday Soc.* **52**, 1172–1175 (1956).
30. Braude, E. A. 127. Studies in light absorption. Part I. p-Benzoquinones. *J. Chem. Soc. Resumed* 490–497 (1945). doi:10.1039/JR9450000490
31. Orlando, C. M. & Bose, A. K. Photorearrangement of Di-t-butyl-p-benzoquinones. *J. Am. Chem. Soc.* **87**, 3782–3783 (1965).
32. Orlando, C. M., Mark, H., Bose, A. K. & Manhas, M. S. Photoreactions. IV. Photolysis of tert-butyl-substituted p-benzoquinones. *J. Am. Chem. Soc.* **89**, 6527–6532 (1967).
33. Orlando, C. M., Mark, H., Bose, A. K. & Manhas, M. S. Photoreactions. V. Mechanism of the photorearrangement of alkyl-p-benzoquinones. *J. Org. Chem.* **33**, 2512–2516 (1968).
34. Baxter, I. & Mensah, I. A. Photolysis of t-butyl-substituted p-benzoquinone mono- and di-imine derivatives. *J. Chem. Soc. C Org.* 2604–2608 (1970). doi:10.1039/J39700002604
35. King, T. J., Forrester, A. R., Ogilvy, M. M. & Thomson, R. H. Photolysis of 2,6-di-t-butyl-1,4-benzoquinone: a new rearrangement. *J. Chem. Soc. Chem. Commun.* 844–844 (1973). doi:10.1039/C39730000844

36. Kraus, G. A. & Wu, Y. 1,5- and 1,9-Hydrogen atom abstractions. Photochemical strategies for radical cyclizations. *J. Am. Chem. Soc.* **114**, 8705–8707 (1992).
37. Görner, H. Photoreactions of 2,5-dibromo-3-methyl-6-isopropyl-1,4-benzoquinone. *J. Photochem. Photobiol. Chem.* **175**, 138–145 (2005).
38. Hu, S. & Neckers, D. C. Lifetime of the 1,4-Biradical Derived from Alkyl Phenylglyoxylate Triplets: An Estimation Using the Cyclopropylmethyl Radical Clock. *J. Org. Chem.* **62**, 755–757 (1997).
39. Griller, D. & Ingold, K. U. Free-radical clocks. *Acc. Chem. Res.* **13**, 317–323 (1980).
40. Wagner, P. J. & Liu, K. C. Photorearrangement of α -allylbutyrophenone to 2-phenyl-2-norbornanol. Determination of 1,4-diradical lifetimes. *J. Am. Chem. Soc.* **96**, 5952–5953 (1974).
41. Small, R. D. & Scaiano, J. C. Photochemistry of phenyl alkyl ketones. The lifetime of the intermediate biradicals. *J. Phys. Chem.* **81**, 2126–2131 (1977).
42. Engel, P. S. & Keys, D. E. Estimation of a cyclic 1,4-biradical lifetime using the cyclopropylcarbinyl rearrangement. *J. Am. Chem. Soc.* **104**, 6860–6861 (1982).
43. Castellino, A. J. & Bruice, T. C. Intermediates in the epoxidation of alkenes by cytochrome P-450 models. 2. Use of the trans-2,trans-3-diphenylcyclopropyl substituent in a search for radical intermediates. *J. Am. Chem. Soc.* **110**, 7512–7519 (1988).
44. Klán, P. & Wirz, J. in *Photochemistry of Organic Compounds* 73–135 (John Wiley & Sons, Ltd, 2009).
45. Allonas, X., Ley, C., Bibaut, C., Jacques, P. & Fouassier, J. P. Investigation of the triplet quantum yield of thioxanthone by time-resolved thermal lens spectroscopy: solvent and population lens effects. *Chem. Phys. Lett.* **322**, 483–490 (2000).
46. Burget, D. & Jacques, P. Dramatic solvent effects on thioxanthone fluorescence lifetime. *J. Lumin.* **54**, 177–181 (1992).
47. Görner, H. Photoreactions of 2-methyl-5-isopropyl-1,4-benzoquinone. *J. Photochem. Photobiol. Chem.* **165**, 215–222 (2004).
48. Barbafina, A. *et al.* Photophysical properties of quinones and their interaction with the photosynthetic reaction centre. *Photochem. Photobiol. Sci.* **7**, 973–978 (2008).

49. Kemp, D. R. & Porter, G. Photochemistry of Methylated p-Benzoquinones. *Proc. R. Soc. Lond. Math. Phys. Eng. Sci.* **326**, 117–130 (1971).
50. Wagner, P. J. Type II photoelimination and photocyclization of ketones. *Acc. Chem. Res.* **4**, 168–177 (1971).
51. Wagner, P. J. & Kemppainen, A. E. Is there any correlation between quantum yields and triplet-state reactivity in Type II photoelimination. *J. Am. Chem. Soc.* **90**, 5896–5897 (1968).
52. Garcia-Garibay, M. A., Gamarnik, A., Bise, R., Pang, L. & Jenks, W. S. Primary Isotope Effects on Excited State Hydrogen Atom Transfer Reactions. Activated and Tunneling Mechanisms in an ortho-Methylanthrone. *J. Am. Chem. Soc.* **117**, 10264–10275 (1995).

DECAGING STRATEGIES BASED ON THE PHOTOREDOX CHEMISTRY OF METHYLENE BLUE

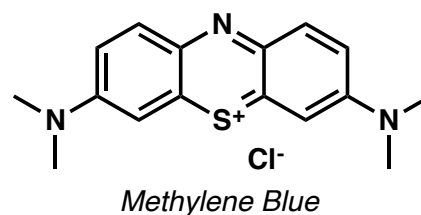
Abstract

The development of new treatments for traumatic brain injury is very challenging due to the occurrence of systemic side-effects and the inability to localize therapeutic agents at the site of the injury in the brain. The use of a photodecaging strategy in the design of new drug candidates allows these issues to be addressed independently, and could have further applications for the treatment of other illnesses that may be receptive to light-based therapies. Methods to decage aldehydes, ketones, and alcohols based on the photoredox chemistry of a common near-infrared dye known as methylene blue are presented. In the first example, photoreduction of the dye is directly coupled to oxidation of an amine, which results in hydrolysis to a ketone/aldehyde. In the second example, photoreduction of the dye to the leuco form results in rapid cyclization with release of an alcohol. The challenges associated with development of these systems are discussed in detail.

1. INTRODUCTION

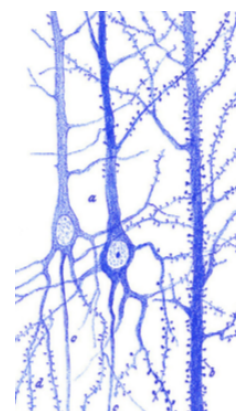
A Brief History of Methylene Blue

The organic compound known as methylene blue is a water-soluble and photostable dye that absorbs strongly in the red. Although it was first synthesized in



1876 for the dye industry, it has developed a rich history for use in the field of biology^{11,12}. In 1890, a German physician named Paul Ehrlich was experimenting with the staining of tissues and found that nerve fibers were selectively stained by methylene blue when fed to live animals. This feature of the dye is still used today, where methylene blue is routinely

administered during intraoperative procedures that require the visualization of nerve fibers. A few years after Ehrlich's initial findings, Santiago Ramon y Cajal used the dye in the discovery of dendritic spines for which he shared the 1906 Nobel Prize with Golgi for the "recognition of their work on the structure of the nervous system."



*dendritic spines
by Ramon y Cajal*

The ability to selectively stain certain tissues also led Ehrlich to the idea that one could selectively kill microorganisms, and in 1891 he discovered that methylene blue selectively stains and kills the malaria parasite. When he cured two patients of the disease, methylene blue became the first synthetic organic compound to be used for medicinal purposes. During WW2, methylene blue became a required treatment against malaria for US soldiers. More recently, the use of methylene blue against malaria has had a revitalization in Sub-Saharan Africa, where the malaria parasite is becoming increasingly resistant to the more common treatment of chloroquinone¹³.

Methylene blue is currently listed as a World Health Organization essential medicine for a basic healthcare system and is approved for a variety of clinical applications including intraoperative visualization, treatment for urinary tract infections, methemoglobinemia, ifosfamide-induced encephalopathy, and distributive shock¹⁴⁻²¹. Additionally, there are twenty active clinical trials of methylene blue for the treatment of Alzheimer disease, depression and anxiety, psychosis, pain, and itching^{14,15}.

Many of the chemical and photochemical properties of methylene blue are well understood. Its chemical structure is an oxidized form of a tricyclic phenothiazine scaffold substituted symmetrically with two dimethylamino groups. Shown in Figure 1, it absorbs strongly in the red with a λ_{max} at 665 nm and an extinction coefficient of $81600 \text{ M}^{-1} \text{ cm}^{-1}$. The excited singlet-state is weakly fluorescent with a quantum yield of 0.05 and a lifetime that varies between 330 and 390 ps, which is too short-lived to undergo diffusional reactions²². However, the singlet undergoes efficient intersystem crossing with a pH dependent quantum yield of approximately 0.6, and generates a long-lived triplet state with a lifetime of 90 μs that can undergo diffusional quenching with triplet oxygen to generate singlet oxygen¹⁷. It also participates in a reversible reduction process with a redox potential at +1.0 V, which is

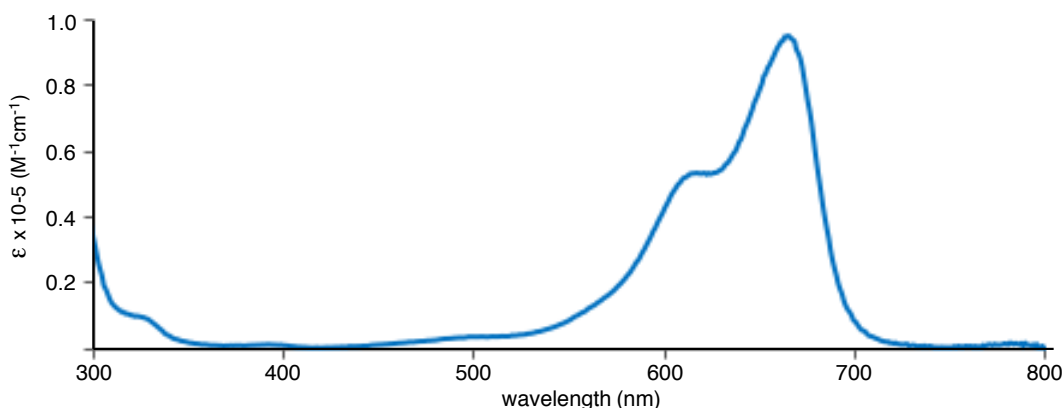


Figure 1. UV/Vis absorption spectrum of methylene blue in water

very close to the O_2/H_2O_2 redox couple at +0.82 V in neutral water. The reduced form of methylene blue, known as the *leuco* dye, is colorless and will spontaneously reoxidize in the presence of O_2 and generate H_2O_2 . Both forms of the dye (oxidized and reduced) have been found to be biologically active, and it is often difficult to distinguish which form is active in a particular biological pathway.

Although the most common photochemical use of methylene blue is as a singlet oxygen generator, there are a few studies that have demonstrated that the dye also participates in photoredox processes^{23–27,27–31} (Figure 2). Bimolecular quenching of the triplet state by

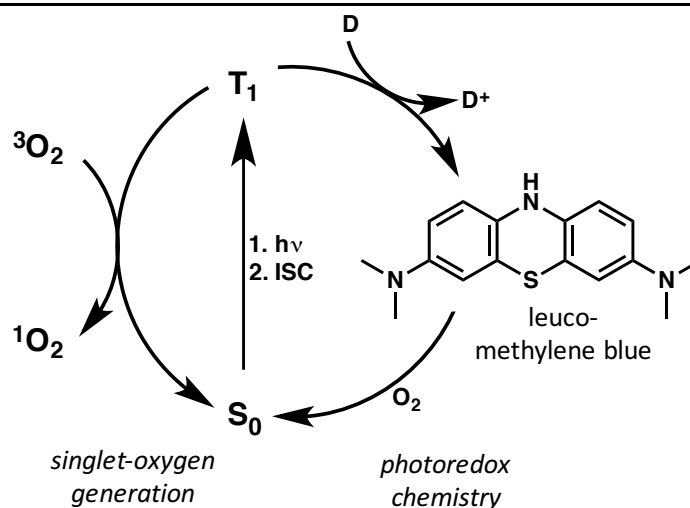


Figure 2. Common photochemical processes of methylene blue. Triplet quenching by 3O_2 results in singlet oxygen formation. Triplet quenching by electron donors results in formation of the leuco dye.

electron donors (**D**) results in the initial generation of a donor radical cation and methylene blue neutral radical. Further reduction then leads to the fully-reduced leuco dye and a two-electron oxidized donor (**D**⁺). Most recent developments of this chemistry use a tertiary aliphatic amine as a sacrificial electron donor in a photocatalytic cycle. Two electron oxidation of the amine results in generation of an enamine or iminium species and the leuco dye, which can then be utilized to reduce another species in solution. This photoredox catalysis has been useful in a synthetic context for the conversion of aryl boronic acids to phenols³², and in the trifluoromethylation of indoles and olefins³³.

The work presented here describes the use of methylene blue in the context of a decaging strategy, where two chemical mechanisms that utilize the photoredox chemistry of methylene blue are explored. In one case, oxidation of a tertiary amine is expected to decage a bioactive aldehyde or ketone after hydrolysis of the initial iminium species (Figure 3A). In this process, electron-transfer is expected to be inhibited by protonation of the aliphatic amine at physiological pH, and efforts to circumvent this issue through the use of less basic diamines are explored in this context.

In the second decaging strategy, reduction of the methylene blue chromophore to the

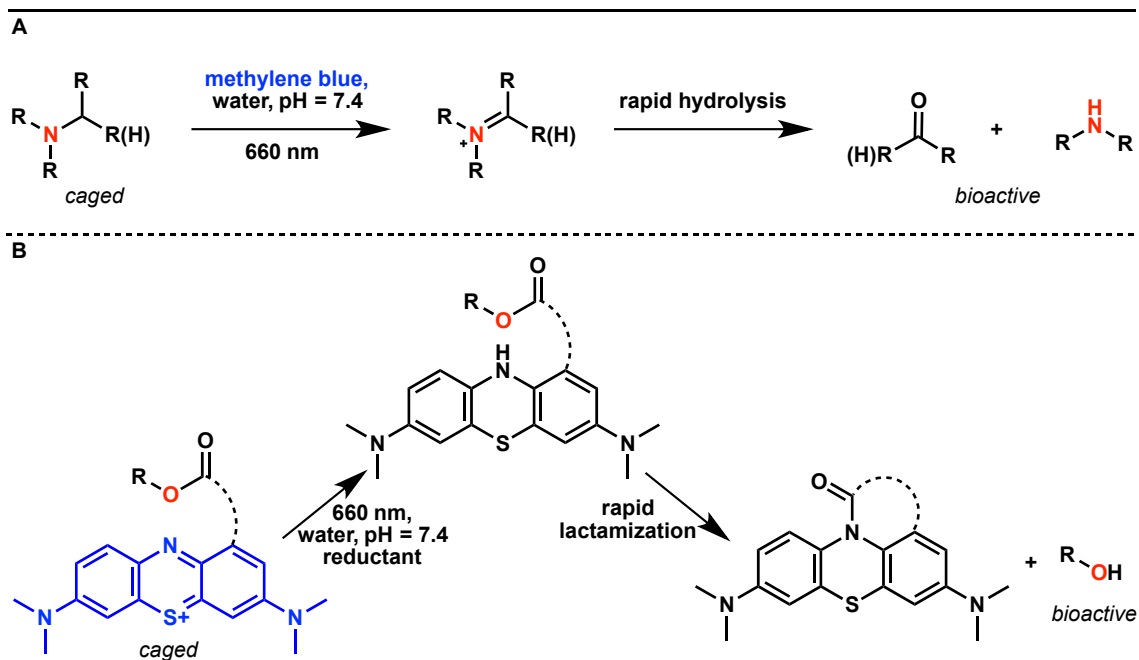


Figure 3. Decaging strategies used in this study. **A)** photooxidation of tertiary aliphatic amines to release secondary amines and aldehydes/ketones. **B)** photoreductive cyclization to release alcohols.

leuco dye is expected to generate a more nucleophilic nitrogen that can be exploited in a rapid lactam-forming reaction, resulting in release of a caged alcohol (Figure 3B). The synthesis of appropriately substituted methylene blue constructs that are capable of undergoing this process, and their photochemical reactivity, are explored and discussed.

2. PHOTOOXIDATION OF TERTIARY AMINES

2.1 Photobleaching Studies

To initially probe for the possibility of a bimolecular photoredox reaction between various amines and methylene blue, 10 μM solutions of the dye were photolyzed in the presence of 20 mM amine in water buffered at physiological pH (Figure 4A). In general, photolysis was carried out in air-equilibrated solutions using a 660 nm LED, and photobleaching was monitored by UV/Vis spectroscopy. Shown in Figure 4B is a time course for photobleaching by triethylamine and various diamines. As expected, photolysis

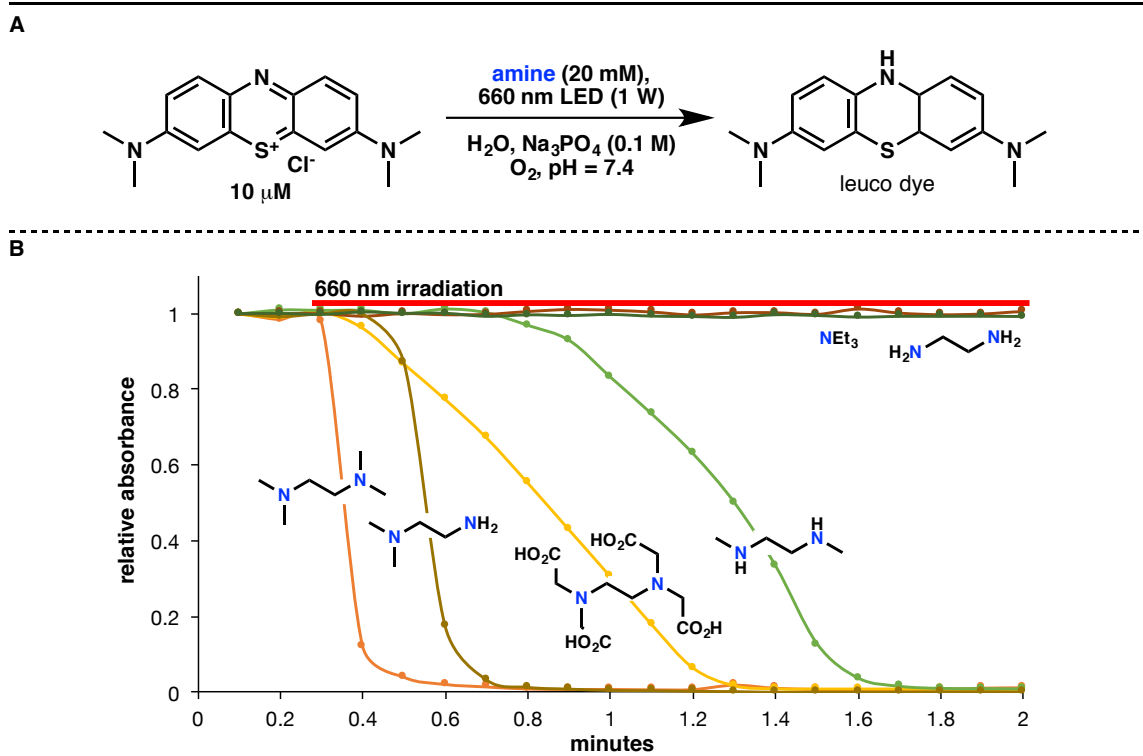


Figure 4. Photobleaching of methylene blue in the presence of various amines. **A)** Reaction conditions. **B)** Time courses for photobleaching monitored by UV/Vis at 650 nm.

in the presence of triethylamine does not result in any observable quenching, while in the presence of the diamines, photobleaching is complete within two minutes. Additionally, diamines that contain a tertiary nitrogen bleach more quickly than those that have exposed N-H bonds.

The effect of the protonation state of the diamines on the photobleaching process was also probed directly using tetramethylethylenediamine (TMEDA) at varying pH. The time courses shown in Figure 5A clearly indicate that the process is inhibited at pH values where the majority of TMEDA is expected to be doubly protonated. Additionally, the rate of photobleaching is dependent upon the concentration of the diamine, which again is

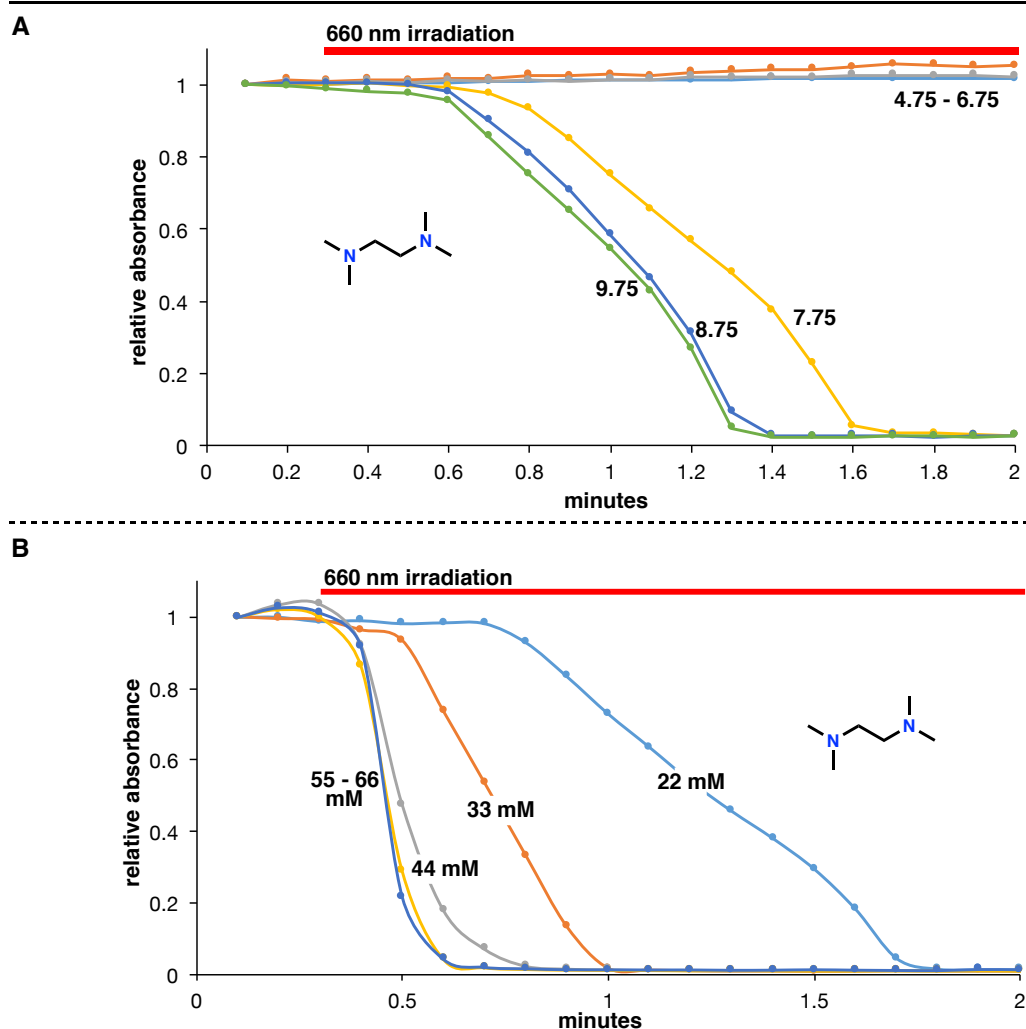


Figure 5. Photobleaching of methylene blue by TMEDA in buffered water due to photolysis at 660 nm. **A)** Effect of pH **B)** Effect of TMEDA concentration at pH = 7.4.

demonstrated with TMEDA in Figure 5B. At lower concentrations, the photobleaching is slower and there is a lengthy incubation time between the start of photolysis and the start of photobleaching.

2.2 Results and Discussion

The product mixture that results from the photolysis of methylene blue in the presence of various diamines is complicated by selectivity issues and oxygen sensitivity. When TMEDA is photolyzed in degassed buffered aqueous solutions, a variety of products is formed, including trimethylethylenediamine, the expected result of oxidation and hydrolysis. However, in the presence of air, photolysis produces a much more complex mixture. Additionally, when trimethylethylenediamine, 1,2- or 1,1-dimethylethylenediamine are photolyzed in degassed solution, a variety of uncharacterized products are obtained that do not seem to be a direct result of the desired photoredox chemistry. Based on these preliminary results, a model is shown in Figure 6 to describe the observed effects. At low concentrations of diamine (< 20 mM), triplet quenching by oxygen is efficient, and decomposition products resulting from the reaction of singlet oxygen with the diamine are formed. At higher concentrations of diamine (> 20 mM) and at an

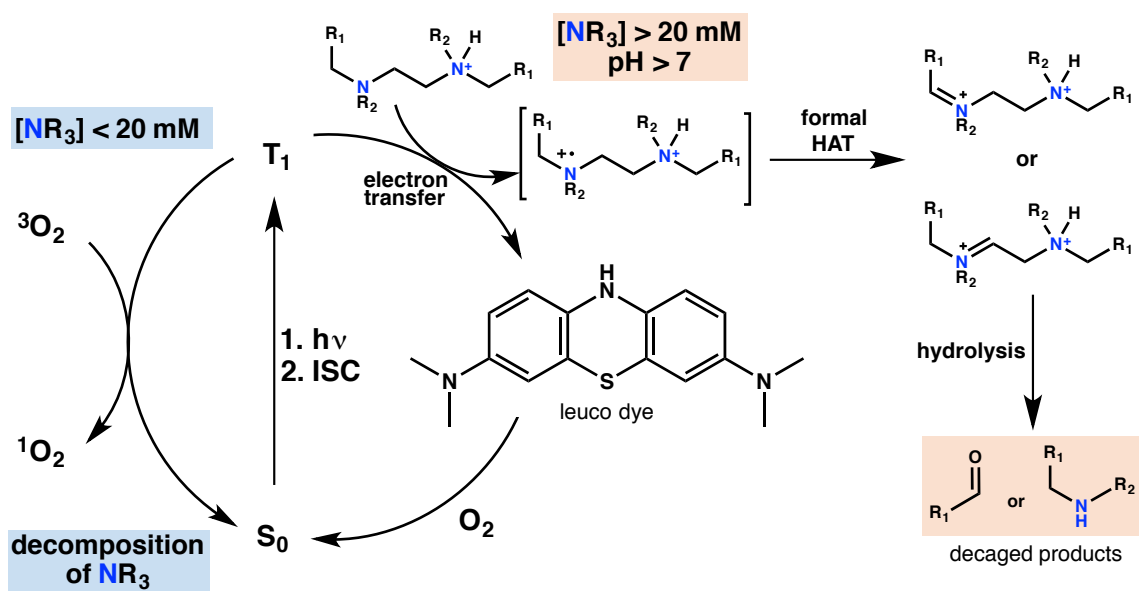


Figure 6. Proposed model to describe experimental observations for the photoreaction of methylene blue with diamines in pH = 7.4 buffered water.

appropriate pH, the triplet is quenched primarily by the diamine, oxygen quenching is suppressed, and the expected hydrolysis products are formed. However, if the diamine contains a nitrogen that is not tertiary, decomposition products result due to an unknown photochemical decay process.

2.3 A Tethered Diamine System

Since this photochemical method is intended to be used in a biological environment, the sensitivity of the aforementioned diamine oxidation processes on the presence of oxygen and the ability for methylene blue to sensitize singlet oxygen formation will have to be suppressed. The bis(dimethylaminoethyl) methylene blue construct **2** was designed to address these concerns (Figure 7). As shown in Figure 7A, the synthesis of **2** is straightforward. Oxidation of phenothiazine with iodine results in precipitation of the phenothiazinium cation **1** as a black solid. Treatment of this species with trimethylethylenediamine in the presence of air results in clean nucleophilic addition to the desired positions, forming **2**, which can be purified in the absence of light using silica gel chromatography or preparative HPLC. Photolysis of **2** in buffered water in the presence of air results in clean conversion to a product that displays a mass spectrum that corresponds to the doubly demethylated species, **3** (Figure 7B). When photolyzed for shorter time periods, a monodemethylated mass is also observed, suggesting that formation of **3** is a sequential process. The assignment of **3** is also supported by the fact that the UV/Vis spectrum of this product is identical to that of **2**. Continued photolysis of **3** results in photobleaching and decomposition of the dye on a much slower time scale than formation of **3**.

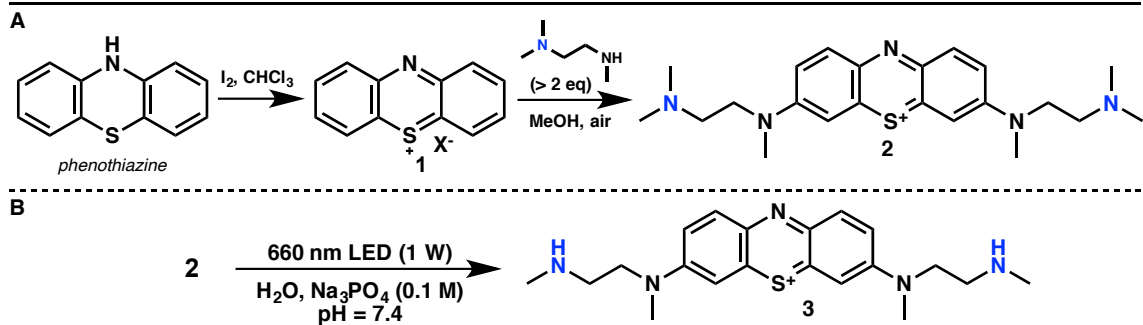


Figure 7. **A)** Synthesis and **B)** photolysis of the bis(dimethylaminoethyl) methylene blue construct, **2**.

To probe for suppressed singlet oxygen formation by **2**, the use of the singlet oxygen trap 1,3-diphenylisobenzofuran (DPBF) was employed. As shown in Figure 8A, when methylene blue is photolyzed in air-equilibrated methanol, the intense absorbance of DPBF at 400 nm rapidly decays as a result of singlet oxygen trapping, which is known to result in the formation of an endoperoxide. When **2** is photolyzed in the presence of DPBF under identical conditions, very little decomposition is observed (Figure 8B), suggesting that **2** does not generate singlet oxygen as efficiently as methylene blue.

These results are consistent with the process outlined in Figure 9. With the high effective concentration of amine afforded through tethering, the methylene blue triplet is quenched much more efficiently through electron transfer than through singlet oxygen

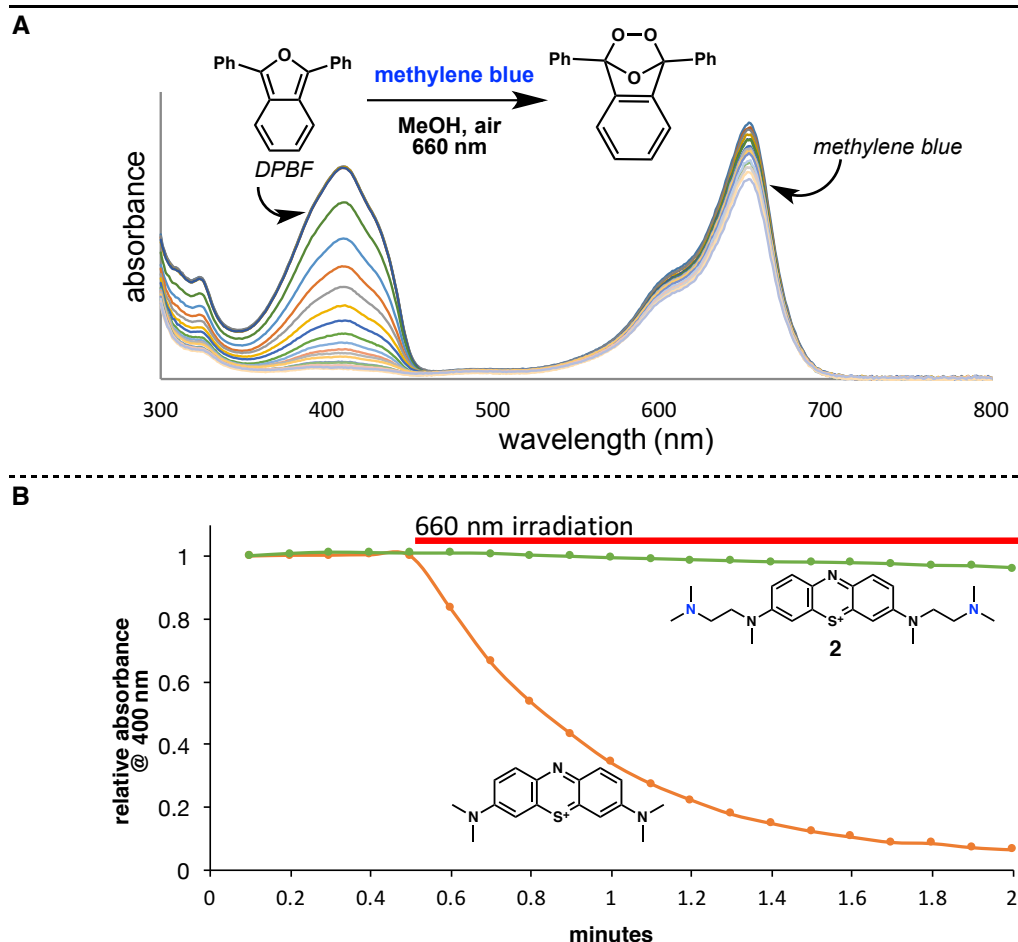


Figure 8. Singlet oxygen trapping by DPBF. **A)** UV/Vis spectrum showing the decay of DPBF during the photolysis of methylene blue. **B)** Time courses for the decay of DPBF due to photolysis of **2** or methylene blue.

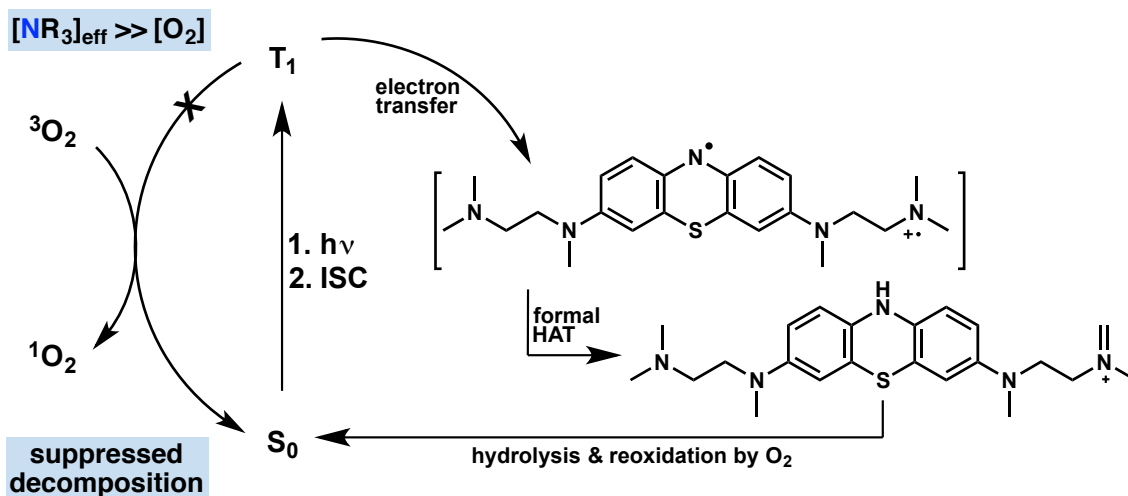
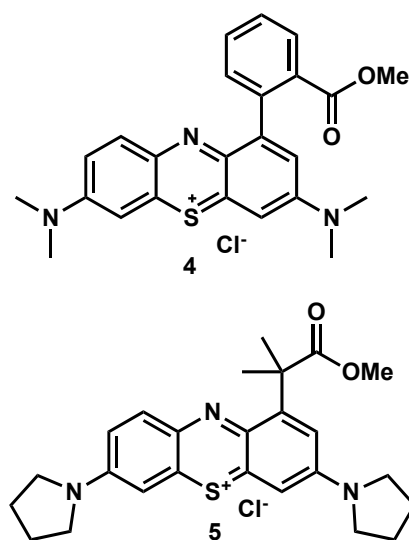


Figure 9. Proposed pathway for the photochemical conversion of **2** to **3**.

generation. That the reaction proceeds cleanly even at low concentrations (< 20 mM) and in air-equilibrated solution suggests that decomposition products resulting from singlet oxygen formation are suppressed. After the initial methyl group is hydrolyzed, the resulting leuco dye can be reoxidized by oxygen and reenter the cycle to oxidize and hydrolyze the second methyl group.

3. DECAGING VIA LACTAM FORMATION

The utility of a phototriggered trimethyl lock reaction has been described previously in this report. In this process, a nucleophilic phenol is generated through an intramolecular photoredox reaction which is properly substituted to undergo a rapid lactonization resulting in the decaging of an alcohol or amine. The photoreduction of methylene blue is also expected to generate a more nucleophilic nitrogen in the leuco dye (Figure 3B), which could potentially undergo rapid cyclization. Two systems have been designed to achieve this effect. The first system (**4**) contains a benzoate cage and was initially targeted due to greater synthetic



accessibility, although it was unclear whether this side chain would rapidly cyclize once reduced. The second system (**5**) does not contain the full trimethyl lock side chain, but previous reports indicate that it would still rapidly cyclize once reduced³⁴.

The synthesis of **4** is shown in Figure 10A. After reduction of methylene blue with sodium dithionite, the leuco dye can be trapped with 2-bromobenzoyl chloride to generate benzamide **6**. An intramolecular Heck cross-coupling with palladium then affords lactam **7**, which was found to smoothly oxidize to the product **4** using NBS in methanol. When **4** is photolyzed in degassed buffered solution at 660 nm in the presence of ascorbate, photobleaching is rapidly observed, but cyclization at room temperature does not readily occur (Figure 10B). However, if the photobleached solution is heated to 100°C for 10 minutes, the expected product (**7**) precipitates cleanly with the decaging of methanol. These results suggest that cyclization of the reduced form of the dye is not efficient at room

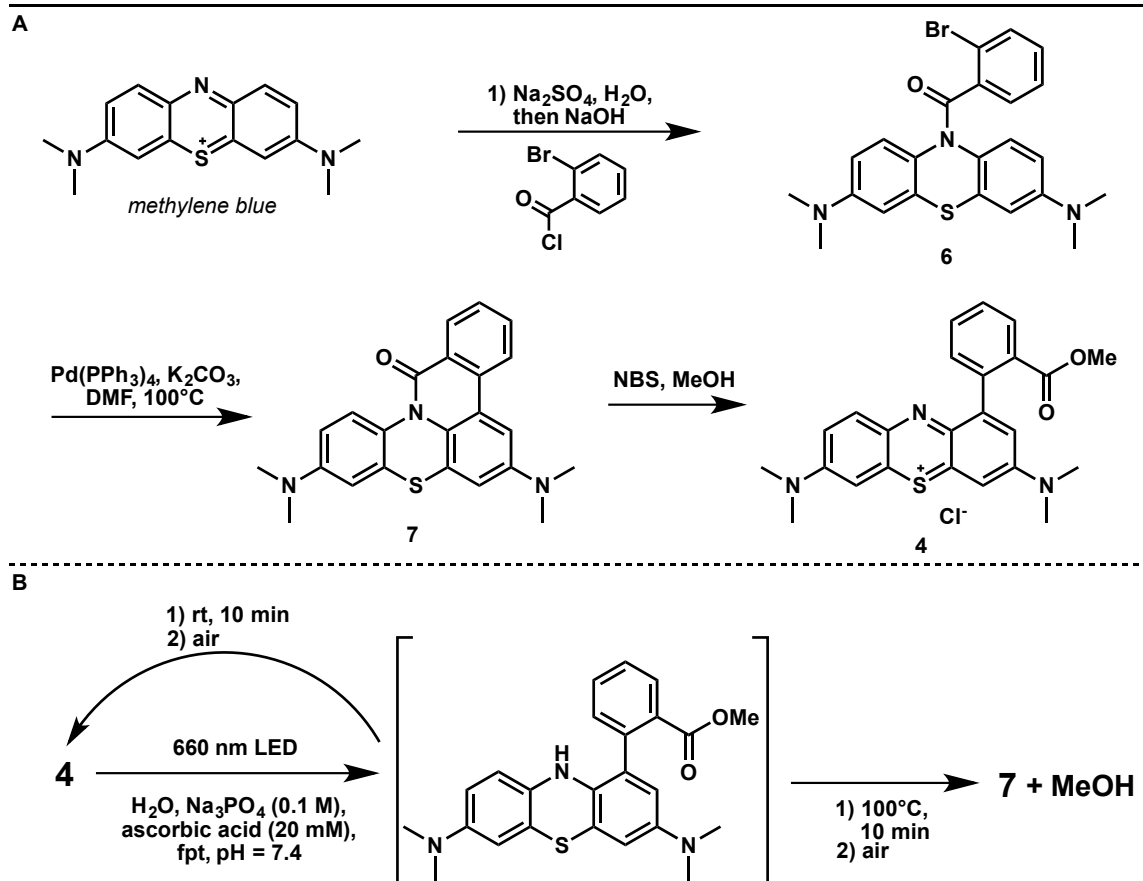


Figure 10. **A)** Synthesis and **B)** photolysis of the methylene blue benzoate photocage **4**.

temperature and that a faster decaying process would be required for application in a biological setting.

A system analogous to **5** containing a substituted nitrobenzene had previously been reported to undergo rapid lactam formation after chemical reduction of the nitro group to an aniline³⁴. Therefore, **5** was also expected to rapidly cyclize once photoreduced to the leuco dye. The synthesis of **5** is shown in Figure 11A. Beginning with commercially available phenothiazine, oxidation with bromine in acetic acid affords quantitative yields of dibromophenothiazine **8**, which can be converted into the acrylamide **9** with methacryloylchloride in refluxing benzene. Subjecting **9** to Friedel-Crafts conditions results in the lactam **10**, which will undergo a delicate C-N cross-coupling reaction with pyrrolidine

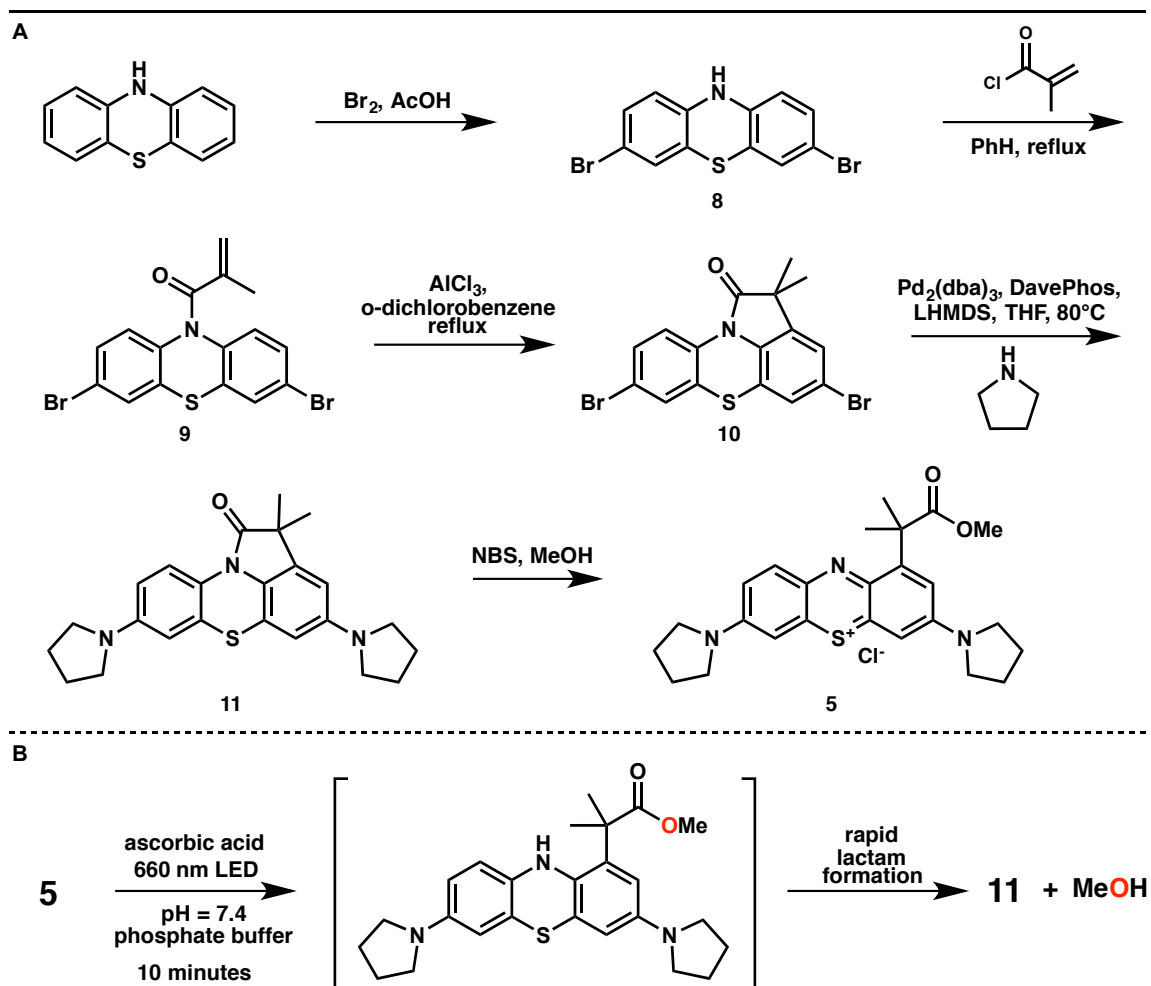


Figure 11. A) Synthesis and **B)** photolysis of the methylene blue dimethylacetate photocage **5**.

to furnish the final intermediate **11**. Oxidation of this intermediate to the methyl ester **5** cleanly occurs with NBS in methanol. The photolysis of this compound in the presence of ascorbate rapidly results in the formation of **11** and the decaging of methanol at room temperature, even when conducted in air-equilibrated solvent (Figure 11B). This suggests that the cyclization process effectively outcompetes reoxidation of the leuco dye. A certain benefit of this system is that cyclization occurs with photobleaching of the chromophore, which prevents secondary photolysis.

4. CONCLUSIONS

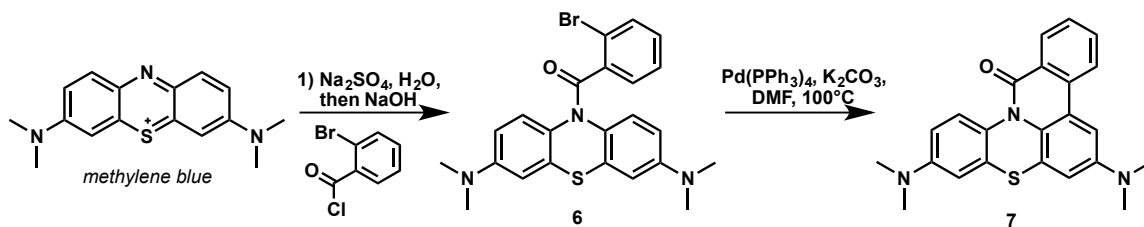
Two photodecaging strategies that harness the intrinsic photoredox chemistry of methylene blue have been explored for potential application in the treatment of TBI. These systems are capable of releasing aldehydes/ketones, alcohols and amines rapidly and efficiently using 660 nm light. The constructs are easily synthesized, thermally stable, and water soluble. Future development of this technology is focused on the decaging of bioactive compounds for use *in vivo*.

5. EXPERIMENTAL

5.1 Materials and Methods

Unless otherwise stated, reactions were performed under an argon atmosphere using freshly dried solvents. N,N-dimethylformamide and methanol were dried by passing through activated alumina. Benzene and ortho-dichlorobenzene were distilled from CaH₂ under an argon atmosphere. All other commercially obtained reagents were used as received unless specifically indicated. All reactions were monitored by thin-layer chromatography using EMD/Merck silica gel 60 F254 pre-coated plates (0.25 mm). Protection of certain materials from light was accomplished by wrapping the reaction, workup, and chromatography glassware with foil or working in conditions of low-ambient light. Unless otherwise stated, irradiations at 660 nm were carried out using using a Thorlabs M660L3 1 W LED focused with a LMR1S lens and powered by the LEDD1B driver set at 1 A.

5.2 Preparative Procedures and Spectroscopic Data



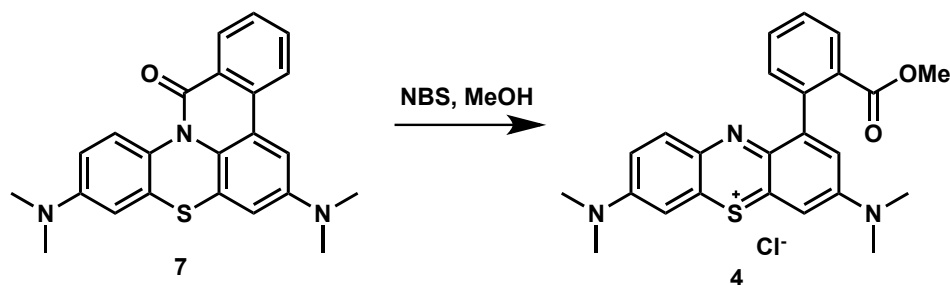
10-(2-bromobenzoyl)-N3,N3,N7,N7-tetramethyl-10H-phenothiazine-3,7-diamine (6).

To a 500 mL round bottom flask equipped with a magnetic stir bar and thermometer, under an argon atmosphere, is added methylene blue (1 eq, 1 g) and deionized water (150 mL). Sodium dithionite (3.15 eq) is added, and the mixture is stirred 45 minutes, followed by the slow addition of sodium hydroxide (6.3 eq) such that the temperature does not rise above 30°C. After stirring an additional 30 minutes, ortho-bromobenzoyl chloride (6.3 eq) is added dropwise, and the mixture is stirred 12 hours. After allowing to settle, the suspension is triturated with water (100 mL x 5) and the liquid discarded. The solid is dissolved in ethanol (20 mL), precipitated with water (100 mL), and filtered. After repeating this procedure three times, the solid is dissolved in DCM, dried over MgSO₄, flushed through a plug of silica gel, and concentrated *in vacuo* to yield **6** as a white solid, which is used without further purification. ¹H NMR (300 MHz, Chloroform-*d*) δ 8.27 – 5.95 (br, 9H), 3.07 – 2.68 (br, 12H). ESI-MS(+) calculated for [C₂₃H₂₃BrN₃OS]⁺ ([M+H]⁺) 468.0 : 470.0 (1 : 1), found 468.0 : 470.0 (1 : 1).

5,11-bis(dimethylamino)-8-thia-1-azapentacyclo[11.7.1.0^{2,7}.0^{9,21}.0^{14,19}]henicosa-

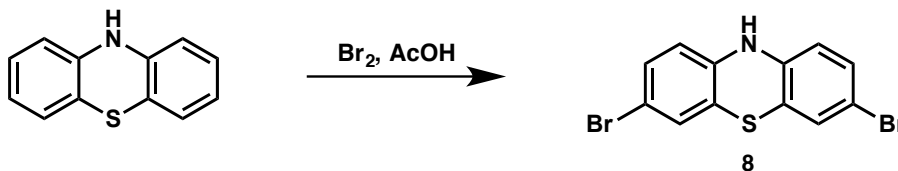
2,4,6,9(21),10,12,14(19),15,17-nonaen-20-one (7). To an oven-dried Schlenk flask equipped with a magnetic stir bar and under an argon atmosphere was added **6** (440 mg, 1 eq), and dry DMF (5 mL). The vessel is purged and backfilled with argon four times, then K₂CO₃ (2 eq) and Pd(PPh₃)₄ (0.5 eq) are added and the closed vessel heated at 100°C for 12 hours. Upon completion, the reaction is allowed to cool to room temperature, then diluted in water (100 mL) and extracted with diethyl ether (100 mL x 3). The combined organics are dried over MgSO₄ and concentrated *in vacuo*. The crude material is purified by flash column chromatography (SiO₂, 1 % MeOH in DCM) to yield **7** as a yellow oil. ¹H

NMR (300 MHz, Chloroform-*d*) δ 8.58 (d, $J = 7.7$ Hz, 1H), 8.15 (d, $J = 8.2$ Hz, 1H), 7.82 – 7.68 (m, 2H), 7.65 – 7.53 (m, 1H), 7.22 – 7.16 (m, 1H), 6.78 – 6.71 (m, 1H), 6.66 – 6.56 (m, 1H), 6.56 – 6.49 (m, 1H), 3.02 (s, 6H), 2.95 (s, 6H). ESI-MS(+) calculated for $[\text{C}_{23}\text{H}_{22}\text{N}_3\text{OS}]^+$ ($[\text{M}+\text{H}]^+$) 388.1, found 388.1.



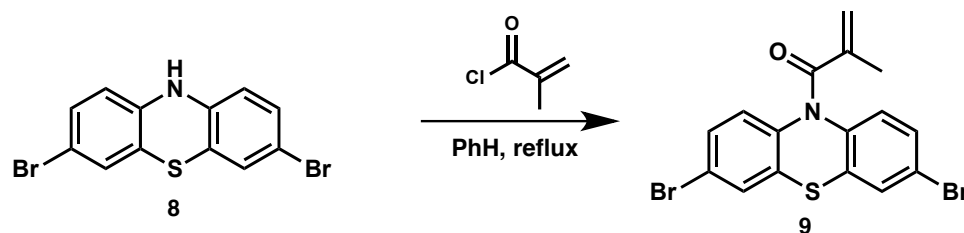
3,7-bis(dimethylamino)-1-[2-(methoxycarbonyl)phenyl]-5 λ^4 -phenothiazin-5-ylum

chloride (4). In a round bottom flask equipped with a magnetic stir bar and protected from light is dissolved lactam **7** (25 mg, 1 eq) in dry methanol (20 mL). A solution of NBS in methanol (1 eq, 1 mL) is added dropwise, and the reaction is stirred under an inert atmosphere for 15 minutes, at which point TLC (5% MeOH/DCM) indicates complete consumption of the starting material. The solution is diluted in 1.5 M HCl (50 mL), and extracted with dichloromethane (50 mL x 3). The combined organics are dried over MgSO_4 and concentrated *in vacuo*. The crude material is purified by flash column chromatography (SiO_2 , 0 – 10% MeOH in DCM) to yield **4** as a dark blue solid. ^1H NMR (400 MHz, Methanol-*d*₄) δ 8.00 (dd, $J = 7.8, 1.4$ Hz, 1H), 7.76 – 7.68 (m, 1H), 7.67 – 7.58 (m, 2H), 7.54 (d, $J = 7.2$ Hz, 1H), 7.43 (s, 2H), 7.39 (dd, $J = 9.5, 2.8$ Hz, 1H), 7.34 (d, $J = 2.7$ Hz, 1H), 3.46 (d, 3H), 3.45 (s, 6H), 3.37 (s, 6H). ESI-MS(+) calculated for $[\text{C}_{24}\text{H}_{24}\text{N}_3\text{O}_2\text{S}]^+$ ($[\text{M}]^+$) 418.1, found 418.0.

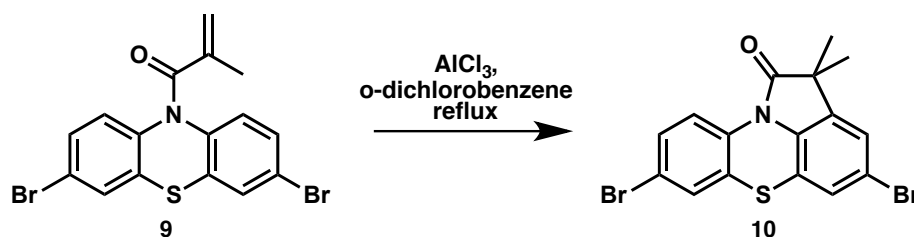


3,7-dibromo-10H-phenothiazine (8). In a 500 mL round bottom flask with magnetic stir bar is suspended phenothiazine (5 g, 1 eq) in acetic acid (250 mL). Bromine (2.5 eq) in

acetic acid (20 mL) is added dropwise via addition funnel and the mixture stirred overnight at room temperature. After cooling with an ice-water bath, Na_2SO_3 (2 eq) is added, followed by water (5 mL). After stirring 5 minutes, 1M NaOH (4 eq) is added, which causes a green solid to precipitate. The solid is filtered, and washed with cold isopropanol to yield **8** as a light-blue solid, which is used without further purification. ^1H NMR (300 MHz, $\text{DMSO-}d_6$) δ 8.83 (s, 1H), 7.13 (m, 4H), 6.56 (d, $J = 8.3$ Hz, 2H). ESI-MS(+) calculated for $[\text{C}_{12}\text{H}_8\text{Br}_2\text{NS}]^+$ ($[\text{M}]^+$) 353.8 : 355.8 : 357.8 (1:2:1), found 353.9 : 355.9 : 357.9 (1:2:1).

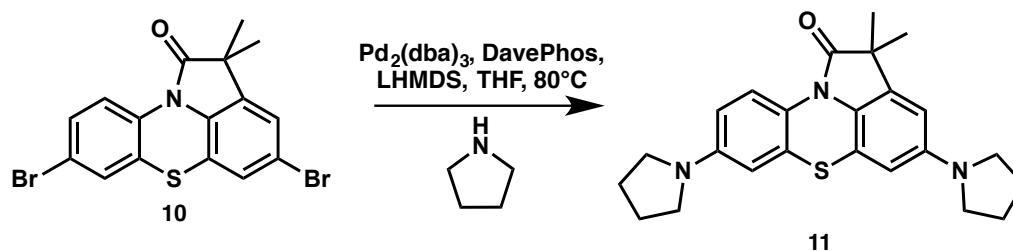


1-(3,7-dibromo-10H-phenothiazin-10-yl)-2-methylprop-2-en-1-one (9). In a 100 mL round bottom flask equipped with a magnetic stir bar and reflux condenser is suspended **8** (1 eq, 5 g) in dry benzene (150 mL). After cooling with an ice-water bath, methacryloyl chloride (1 eq) is added dropwise, and the solution is allowed to warm to room temperature, then heated to reflux overnight. After allowing to cool, the solvent is removed *in vacuo* to yield **9** as a white solid. ^1H NMR (300 MHz, $\text{DMSO-}d_6$) δ 7.83 (s, 2H), 7.65 – 7.46 (m, 4H), 5.21 (s, 1H), 4.95 (s, 1H), 1.81 (s, 3H). ESI-MS(+) calculated for $[\text{C}_{16}\text{H}_{12}\text{Br}_2\text{NOS}]^+$ ($[\text{M}+\text{H}]^+$) 423.9 : 425.9 : 427.9 (1:2:1), found 423.9 : 425.9 : 427.9 (1:2:1).



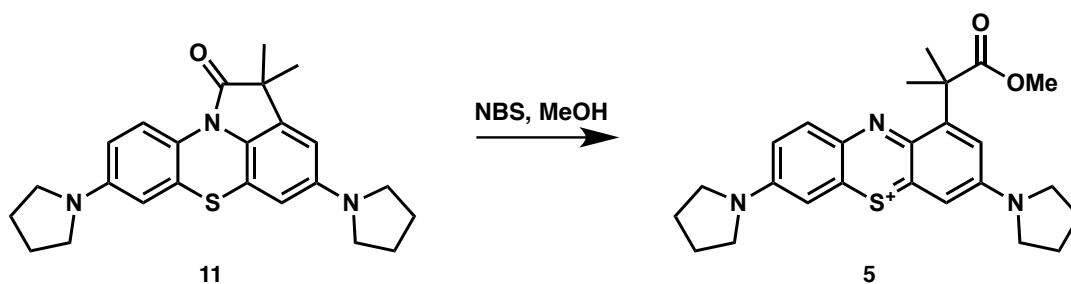
5,11-dibromo-14,14-dimethyl-8-thia-1-azatetracyclo[7.6.1.0^{2,7}.0^{13,16}]hexadeca-2,4,6,9(16),10,12-hexaen-15-one (10). To an oven-dried 250 mL round bottom flask equipped with a reflux condenser and magnetic stir bar is added **9** (1.2 g, 1 eq) and freshly

distilled *o*-dichlorobenzene (5 mL). AlCl_3 (3 eq) is added portionwise and the reaction is heated to reflux under argon for two hours, then cooled and diluted with 1 M HCl (200 mL). After vigorously stirring overnight, the mixture is extracted with DCM (100 mL x 3), and the combined organics dried over MgSO_4 and concentrated *in vacuo*. The resulting black sludge is taken up in a minimal amount of hexane, and loaded onto a column of silica gel. After flushing with hexanes to completely remove the residual *ortho*-dichlorobenzene, the product is eluted with 5% EtOAc in hexanes to yield **10** as a crystalline white solid. ^1H NMR (300 MHz, Chloroform-*d*) δ 8.61 (d, $J = 9.1$ Hz, 1H), 7.19 (m, 1H), 7.09 (s, 1H), 7.01 (s, 1H), 6.93 (s, 1H), 1.40 (s, 6H). ESI-MS(+) not recorded – **10** does not elute from the LCMS.



14,14-dimethyl-5,11-bis(pyrrolidin-1-yl)-8-thia-1-

azatetracyclo[7.6.1.0^{2,7}.0^{13,16}]hexadeca-2,4,6,9(16),10,12-hexaen-15-one (11). To an oven-dried Schlenk flask under an argon atmosphere is added **10** (1 eq, 200 mg), $\text{Pd}_2(\text{dba})_3$ (0.02 eq), and DavePhos (0.024 eq). The flask is purged and backfilled with argon five times, then freshly distilled pyrrolidine (2.2 eq) and LHMDS (4.4 eq, 1M in THF) is added. The Schlenk is closed and heated to 65°C for 1 hour, then cooled, and diluted in sat. aq. NH_4Cl (20 mL). The solution is extracted with DCM (20 mL x 3), and the combined organics are dried over MgSO_4 and concentrated *in vacuo*. The crude material is purified by flash column chromatography (SiO_2 , 2-5 % MeOH in DCM) to yield **11** as a yellow oil. ^1H NMR (300 MHz, Chloroform-*d*) δ 8.70 (d, $J = 9.2$ Hz, 1H), 6.30 (dd, $J = 9.2, 2.7$ Hz, 1H), 6.16 (dd, $J = 6.2, 2.5$ Hz, 2H), 6.00 (d, $J = 2.2$ Hz, 1H), 3.24 (m, 8H), 1.99 (m, 8H), 1.39 (s, 6H). ESI-MS(+) calculated for $[\text{C}_{24}\text{H}_{28}\text{N}_3\text{OS}]^+$ ($[\text{M}+\text{H}]^+$) 406.2, found 406.1.



1-(1-methoxy-2-methyl-1-oxopropan-2-yl)-3,7-bis(pyrrolidin-1-yl)-5 λ^4 -phenothiazin-5-ylum (5). In a 2 mL vial equipped with a magnetic stir bar and protected from light is dissolved lactam **11** (2 mg, 1 eq) in dry methanol (1 mL). A solution of NBS in methanol (1 eq, 0.05 M) is added dropwise, and the reaction is stirred under an inert atmosphere for 15 minutes, at which point TLC (5% MeOH/DCM) indicates complete consumption of the starting material. The solution is diluted in 1.5 M HCl (5 mL), and extracted with dichloromethane (5 mL x 3). The combined organics are dried over MgSO₄ and concentrated *in vacuo*. The crude material is purified by flash column chromatography (SiO₂, 0 – 10% MeOH in DCM) to yield **5** as a dark blue residue. ¹H NMR (300 MHz, Chloroform-*d*) δ 7.76 (d, $J = 9.3$ Hz, 1H), 7.56 (m, 2H), 7.04 (m, 2H), 3.75 (br, 8H), 3.54 (s, 3H), 2.18 (br, 8H), 1.65 (s, 6H). ESI-MS(+) calculated for [C₂₅H₃₀N₃O₂S]⁺ ([M]⁺) 436.2, found 436.1.

5.2 Photolysis Procedures

Photolysis of 4. In a 10 mL Schlenk flask equipped with a magnetic stir bar, a solution of **4** with an absorbance of 1 - 2 at 665 nm is prepared in pH = 7.4 phosphate (0.1 M) buffered water containing 0.02 M ascorbate. The solution is freeze-pump-thawed thrice, and then sealed under vacuum. Irradiation of the sample using the focused beam from a 660 nm LED (Thorlabs M660L3; 1 W) for 15 mins produces a colorless solution, which is stirred at either (A) room temperature or (B) 100°C for 10 minutes, then sparged with air. The resulting products are analyzed by LCMS using a 40-95% acetonitrile-water gradient over 10 minutes with positive electrospray. For (A) **7** is not observed in the product mixture (ret. time = 8.7 mins; [M+H]⁺ = 388.1) and the solution recolorizes. For (B) **7** is observed in the product mixture and the solution remains colorless.

Photolysis of 5. In a 2 mL vial equipped with a magnetic stir bar, a solution of **5** with an absorbance of 1 - 2 at 665 nm is prepared in pH = 7.4 phosphate (0.1 M) buffered water containing 0.02 M EDTA or 0.02 M ascorbic acid. Irradiation of the sample using the focused beam from a 660 nm LED (Thorlabs M660L3; 1 W) for 30 mins produces a colorless suspension. The resulting products are analyzed by LCMS using a 40-95% acetonitrile-water gradient over 10 minutes with positive electrospray. The lactam **10** is observed in the product mixture (ret. time = 9.5 mins; $[M+H]^+ = 406.1$) and the solution remains colorless. The ^1H NMR spectrum of the precipitate (obtained after filtration) is identical with lactam **10**.

6. REFERENCES

1. Loane, D. J. & Faden, A. I. Neuroprotection for traumatic brain injury: translational challenges and emerging therapeutic strategies. *Trends Pharmacol. Sci.* **31**, 596–604 (2010).
2. Xiong, Y., Mahmood, A. & Chopp, M. Emerging treatments for traumatic brain injury. *Expert Opin. Emerg. Drugs* **14**, 67–84 (2009).
3. DeKosky, S. T., Blennow, K., Ikonomic, M. D. & Gandy, S. Acute and chronic traumatic encephalopathies: pathogenesis and biomarkers. *Nat. Rev. Neurol.* **9**, 192–200 (2013).
4. Dinh, M. M. *et al.* Redefining the golden hour for severe head injury in an urban setting: the effect of prehospital arrival times on patient outcomes. *Injury* **44**, 606–610 (2013).
5. Hook, G., Jacobsen, J. S., Grabstein, K., Kindy, M. & Hook, V. Cathepsin B is a New Drug Target for Traumatic Brain Injury Therapeutics: Evidence for E64d as a Promising Lead Drug Candidate. *Front. Neurol.* **6**, 178 (2015).
6. Duhaime, A. C. Exciting your neurons to death: can we prevent cell loss after brain injury? *Pediatr. Neurosurg.* **21**, 117–122; discussion 123 (1994).
7. Gibson, C. J., Meyer, R. C. & Hamm, R. J. Traumatic brain injury and the effects of diazepam, diltiazem, and MK-801 on GABA-A receptor subunit expression in rat hippocampus. *J. Biomed. Sci.* **17**, 1–11 (2010).
8. Naeser, M. A., Saltmarche, A., Kregel, M. H., Hamblin, M. R. & Knight, J. A. Improved Cognitive Function After Transcranial, Light-Emitting Diode Treatments in Chronic, Traumatic Brain Injury: Two Case Reports. *Photomed. Laser Surg.* **29**, 351–358 (2011).

9. Morries, L. D., Cassano, P. & Henderson, T. A. Treatments for traumatic brain injury with emphasis on transcranial near-infrared laser phototherapy. *Neuropsychiatr. Dis. Treat.* **11**, 2159–2175 (2015).
10. Henderson, T. A. & Morries, L. D. Near-infrared photonic energy penetration: can infrared phototherapy effectively reach the human brain? *Neuropsychiatr. Dis. Treat.* **11**, 2191–2208 (2015).
11. Schirmer, R. H., Adler, H., Pickhardt, M. & Mandelkow, E. Lest we forget you - methylene blue *Neurobiol. Aging* **32**, 2325.e7 (2011).
12. Wainwright, M. & Crossley, K. B. Methylene Blue - a therapeutic dye for all seasons? *J. Chemother.* **14**, 431–443 (2002).
13. Wainwright, M. & Amaral, L. The phenothiazinium chromophore and the evolution of antimalarial drugs. *Trop. Med. Int. Health TM IH* **10**, 501–511 (2005).
14. Oz, M., Lorke, D. E. & Petroianu, G. A. Methylene blue and Alzheimer's disease. *Biochem. Pharmacol.* **78**, 927–932 (2009).
15. Oz, M., Lorke, D. E., Hasan, M. & Petroianu, G. A. Cellular and Molecular Actions of Methylene Blue in the Nervous System. *Med. Res. Rev.* **31**, 93–117 (2011).
16. Tardivo, J. P. *et al.* Methylene blue in photodynamic therapy: From basic mechanisms to clinical applications. *Photodiagnosis Photodyn. Ther.* **2**, 175–191 (2005).
17. Tuite, E. M. & Kelly, J. M. New trends in photobiology: Photochemical interactions of methylene blue and analogues with DNA and other biological substrates. *J. Photochem. Photobiol. B* **21**, 103–124 (1993).
18. Jang, D. H., Nelson, L. S. & Hoffman, R. S. Methylene Blue for Distributive Shock: A Potential New Use of an Old Antidote. *J. Med. Toxicol.* **9**, 242–249 (2013).
19. Louters, L. L. *et al.* Methylene blue stimulates 2-deoxyglucose uptake in L929 fibroblast cells. *Life Sci.* **78**, 586–591 (2006).
20. Callaway, N. L., Riha, P. D., Wrubel, K. M., McCollum, D. & Gonzalez-Lima, F. Methylene blue restores spatial memory retention impaired by an inhibitor of cytochrome oxidase in rats. *Neurosci. Lett.* **332**, 83–86 (2002).

21. Callaway, N. L., Riha, P. D., Bruchey, A. K., Munshi, Z. & Gonzalez-Lima, F. Methylene blue improves brain oxidative metabolism and memory retention in rats. *Pharmacol. Biochem. Behav.* **77**, 175–181 (2004).
22. Danziger, R. M., Bar-Eli, K. H. & Weiss, K. The laser photolysis of methylene blue. *J. Phys. Chem.* **71**, 2633–2640 (1967).
23. Nicewicz, D. A. & Nguyen, T. M. Recent Applications of Organic Dyes as Photoredox Catalysts in Organic Synthesis. *ACS Catal.* **4**, 355–360 (2014).
24. Kalaitzakis, D., Kouridaki, A., Noutsias, D., Montagnon, T. & Vassilikogiannakis, G. Methylene Blue as a Photosensitizer and Redox Agent: Synthesis of 5-Hydroxy-1H-pyrrol-2(5H)-ones from Furans. *Angew. Chem. Int. Ed.* **54**, 6283–6287 (2015).
25. A Rafia, U. F. Photoredox Reaction of Methylene Blue and Lactose in Alcoholic Buffered Solution.
26. Casarotto, M. G. & Smith, G. J. Methylene-blue-sensitized photo-oxidation of terpenes. *J. Photochem.* **40**, 87–91 (1987).
27. Kayser, R. & Young, R. Photoreduction of Methylene-Blue by Amines .1. Flash-Photolysis Study of Reaction Between Triplet Methylene-Blue and Amines. *Photochem. Photobiol.* **24**, 395–401 (1976).
28. Kayser, R. H. & Young, R. H. THE PHOTOREDUCTION OF METHYLENE BLUE BY AMINES—II. AN INVESTIGATION OF THE DECAY OF SEMIREduced METHYLENE BLUE. *Photochem. Photobiol.* **24**, 403–411 (1976).
29. Kato, S., Usui, Y. & Koizumi, M. The Application of Intermittent Illumination to the Bleaching of Dye. II. The Methylene Blue-Amine System. *Bull. Chem. Soc. Jpn.* **36**, 1522–1527 (1963).
30. Obata, H., Kogasaka, K. & Koizumi, M. Photochemical Reactions Between Methylene Blue and Trimethylamine, Dimethylamine and Monomethylamine .3. the Behavior of Methylene Blue in the Presence of Oxygen. *Bull. Chem. Soc. Jpn.* **32**, 125–132 (1959).
31. Goerner, H. Oxygen uptake induced by electron transfer from donors to the triplet state of methylene blue and xanthene dyes in air-saturated aqueous solution. *Photochem. Photobiol. Sci.* **7**, 371–376 (2008).

32. Pitre, S. P., McTiernan, C. D., Ismaili, H. & Scaiano, J. C. Mechanistic Insights and Kinetic Analysis for the Oxidative Hydroxylation of Arylboronic Acids by Visible Light Photoredox Catalysis: A Metal-Free Alternative. *J. Am. Chem. Soc.* **135**, 13286–13289 (2013).
33. Pitre, S. P., McTiernan, C. D., Ismaili, H. & Scaiano, J. C. Metal-Free Photocatalytic Radical Trifluoromethylation Utilizing Methylene Blue and Visible Light Irradiation. *ACS Catal.* **4**, 2530–2535 (2014).
34. Liu, B. & Hu, L. 5'-(2-Nitrophenylalkanoyl)-2'-deoxy-5-fluorouridines as potential prodrugs of FUDR for reductive activation. *Bioorg. Med. Chem.* **11**, 3889–3899 (2003).